

**Estimation of population density using drones:
The case of red deer (*Cervus elaphus*) and chronic wasting
disease management in Norway**

Julie Bommerlund



**UNIVERSITETET
I OSLO**

Master Thesis (60 credits)

Ecology and Evolution

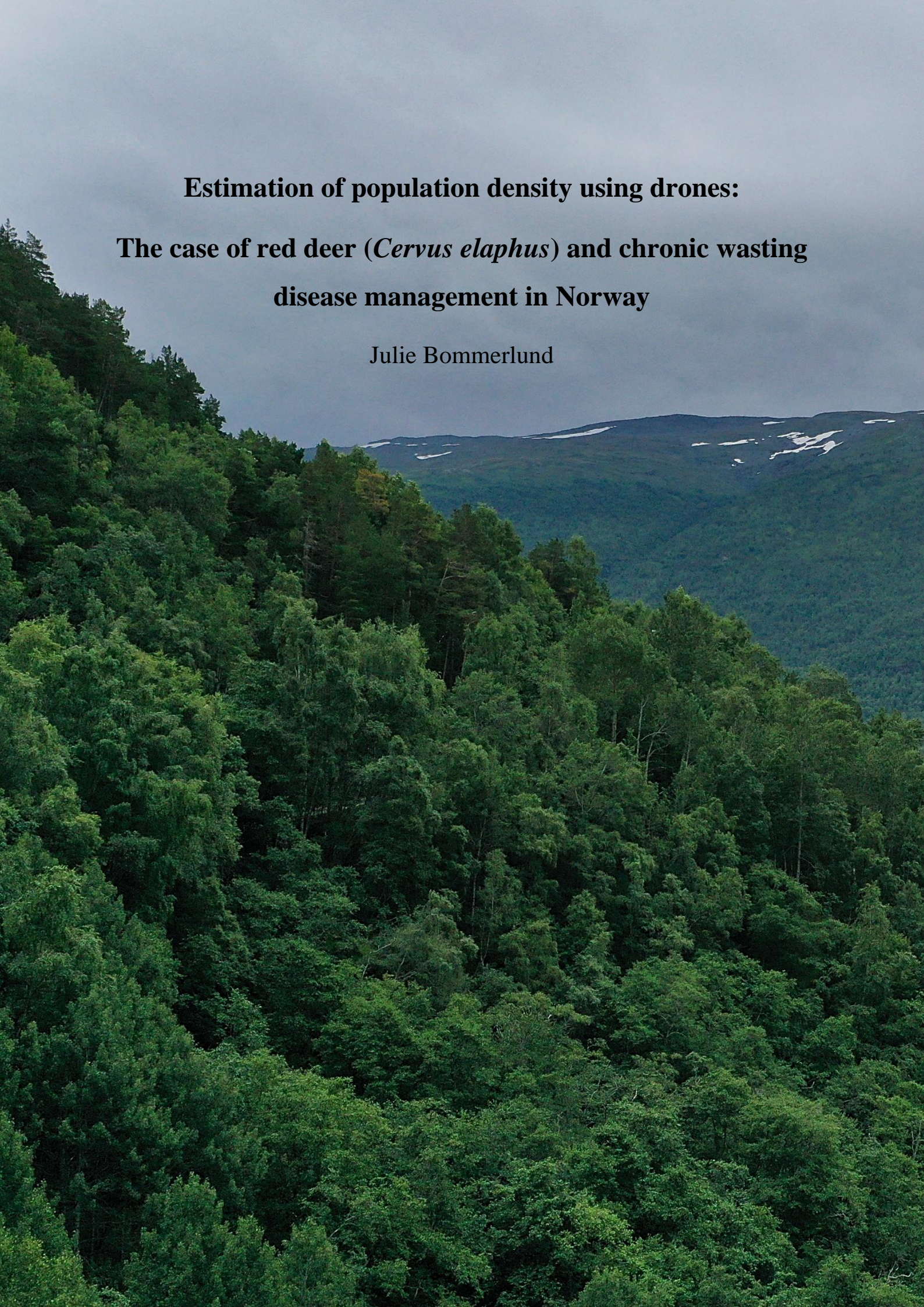
Centre for Ecological and Evolutionary Synthesis

Department of Bioscience

Faculty of Mathematics and Natural Sciences

UNIVERSITY OF OSLO

August 2022

An aerial photograph of a vast, dense forest in Norway. The forest is composed of various types of trees, including tall evergreens and shorter deciduous trees, creating a rich green canopy. In the background, rolling hills and mountains are visible, some with patches of snow. The sky is overcast and grey.

Estimation of population density using drones:
**The case of red deer (*Cervus elaphus*) and chronic wasting
disease management in Norway**

Julie Bommerlund

© Julie Bommerlund, 2022

Estimation of population density using drones: The case of red deer (*Cervus elaphus*) and chronic wasting disease management in Norway

Julie Bommerlund

<https://www.duo.uio.no/>

Print: Reprosentralen, Universitetet i Oslo

Front page photo credit: Julie Bommerlund

Second page photo credit: Nils Olav Talgøy



Abstract

Precise and accurate information about population numbers is crucial within wildlife ecology, for example to effectively manage disease threats. After chronic wasting disease was detected in a reindeer (*Rangifer tarandus*) population in Norway, concerns that moose and red deer in the area would contract the fatal disease arose. Aiming to lower the probability of such a spillover, the Norwegian Environment Agency recommended that the at-risk moose and red deer populations should be reduced to less than one animal per km². However, accurate and precise estimates on absolute densities of deer are difficult, often impossible, to obtain using traditional data collection methods. This is especially true for elusive species living in inaccessible areas. Current estimates of red deer (*Cervus elaphus*) abundance and density in Norway are unreliable with no known degrees of uncertainties. Thus, these estimates do not suffice when it comes to determining the harvest quotas needed to reach the population density goal set by the authorities. The purpose of this thesis was therefore to develop a method for more reliable population estimates of red deer using drones. In a case study approach, the drones were used to collect data from four different sampling areas in Lærdal, Norway. Detections of red deer in the drone images were then recorded using a double-observer protocol and hierarchical state-space models were fitted to the data using a Bayesian approach to obtain posterior distributions of absolute deer density. Although the produced critical intervals were rather wide, the results revealed that absolute red deer density estimates with quantifiable uncertainties can be produced using this method. Furthermore, the method showed great potential for reliable spatiotemporal comparisons of deer density estimates.

Acknowledgments

First and foremost, I would like to thank my main supervisor, Torbjørn Ergon, for guiding me throughout this project. Thank you for spending hours and hours providing me with the tools and statistics comprehension I needed to make the thesis happen. You and your patience has been invaluable. Furthermore, I would like to express my gratitude to my two supervisors Atle Mysterud and Simon Filhol. Atle, thank you for sharing of your extensive deer knowledge and for your incredibly motivating feedback along the way. Simon, thank you for teaching me about drones, and in particular, thank you for projecting the images used in this study and thus making it possible to retrieve crucial information. For his assistance as well as deep insight into chronic wasting disease (CWD) and red deer in Lærdal, I would like to thank the CWD-coordinator of Lærdal municipality, Lars Nesse. In addition, I would like to thank the landowners of Lærdal who gave me permission to access and fly the drones above their land. I am also greatly appreciative of the local heroes of Lærdal, especially Njål Kaardal Golf, who helped me retrieve the crashed drones when my fear of heights would not permit me to recover them from the steep mountain slopes myself. Furthermore, I wish to extend my thanks to Øystein Brekkum at NIBIO for providing me with GPS data of red deer during my field work. And thank you to Vestland County Municipality for allotting me funding from the Norwegian Environment Agency's grant for game purposes.

Of course, I would also like to thank all of my family and friends. Thank you especially to my best friend and roommate, Ru, for waiting quietly and patiently right by my side every day while I have been working on this thesis. You are the best dog in the world. In that regard, thank you so much to Karoline Aarvik, Filip Krefting, Anette Fanny Dvergastein, and Marte Holt Sannesmoen for making it possible for me to complete the field work by ensuring Ru was in good and safe hands while I was in Lærdal, even on just hours' notice. You are the best. Also, "to tusen takk" (two thousand thanks) to my boyfriend Nicholas Baldwin for taking care of both Ru and me while I have been spending my days writing, and for listening to me reading pages of drafts and going on about everything related to counting red deer (of which I know you have no personal interest). You are also the best. Further, I would like to thank the best office mates in room 3124 for their constant encouragement, help, lunch talks, and (maybe most importantly) cakes every Monday. I am so grateful I ended up sharing an office with you. Thank you so much to the best mamma, pappa, sisters, and brother in the world for always supporting me in absolutely everything I do or try to do. Finally, I would like to add an extra special thanks to my sister, Anette Bommerlund alias "Observer 1".

Table of content

Abstract	v
Acknowledgments	vi
1 Introduction	1
1.1 Population estimation in wildlife ecology	1
1.2 Chronic wasting disease (CWD) and the need for population estimates.....	3
1.3 Aim of thesis	4
2 Methods	5
2.1 Study area.....	5
2.2 Spatial sampling design.....	6
2.3 Equipment: UAVs and terrain model.....	9
2.4 Survey flights	10
2.5 Analysis.....	12
2.5.1 Selecting focal images.....	12
2.5.2 Detecting and recording red deer.....	13
2.5.3 Making count data with site covariates	16
2.5.4 Considering availability bias	19
2.5.5 Statistical modeling	21
3 Results	25
3.1 Availability of red deer.....	25
3.2 Model results	25
3.3 Behavioral response	32
4 Discussion	35
4.1 Absolute red deer density estimates and CWD management.....	35
4.2 Effect of variables on red deer density estimates	38
4.3 Effects of UAV on red deer behavior.....	40
4.4 Limitations and advantages of UAV for density estimates	41
5 Concluding remarks and future recommendations	46
References	47
Appendices	56
Appendix A: List of survey flights and route perimeters	56
Appendix B: Settings of UAVS and apps	60
Appendix C: List of GPS-collared red deer and potential survey matches	62
Appendix D: R-code.....	64
D1. R-code for section 2.5.1 Selecting focal images.....	64
D2. R-code for section 2.5.3 Checking for GPS-collared deer	64
D3. R-code for section 2.5.4 Making count data with site covariates	65

D4. R-code for section 2.5.5 Statistical modeling	69
Appendix E: Model definition.....	76
Observation model	76
Process model.....	77
Making use of known density in deer enclosure to inform priors on detectability	78
Appendix F: Model results	81
Prior.....	81
Model 1: Predictor variable ‘field distance’	81
Model 2: Predictor variable ‘forest distance’	83
Model 3: Predictor variable ‘mean elevation’	85

1 Introduction

1.1 Population estimation in wildlife ecology

Accurate, consistent, and effective monitoring of animals' population numbers is crucial for adaptive management and conservation of natural ecosystems (Collier et al., 2013; Lisein et al., 2013; Vermeulen et al., 2013; Corcoran et al., 2019; Spaan et al., 2019). Spatial and temporal data on a species' population abundance or density can be used to evaluate whether conservation efforts are having the desired effects on endangered species (Corcoran et al., 2019; Graves et al., 2022). Information about population density is also key when it comes to managing species with disease threats (Graves et al., 2022). In particular, such information is a premise when making decisions regarding reduction of density as a means to help prevent high disease prevalence (Graves et al., 2022). Further, data on invasive species' presence, population size and density can be used to track these species' distributions (Corcoran et al., 2019; Graves et al., 2022) and thus contribute to the regulation of harmful non-native species. Finally, one of the most common uses of population estimates for management of large mammals is to inform decisions related to harvesting management.

Yet, gathering information about population abundance and density can be challenging, and the methods traditionally used for this purpose have different drawbacks. Ground-based line transects, double-observer or repeat observation, and capture-recapture sampling can provide rigorous estimates when it comes to detection and abundance, but often fall short when it comes to capturing spatial variation in density (Graves et al., 2022). To account for the latter, surveys can be performed from manned aircrafts, but this involves high monetary costs as well as serious safety concerns (Kellenberger, Marcos and Tuia, 2018; Graves et al., 2022). In addition, population estimates derived from manned aerial counts suffer from both imprecision and inaccuracy (Eikelboom et al., 2019).

Traditional data collection methods for wild deer are indeed costly, labor intensive and/or unreliable. Hence, absolute abundance and density of deer is rarely known (Witczuk et al., 2018; Forsyth et al., 2022). This is especially true for widely dispersed species living in inaccessible areas or in complex structural environments (Kellenberger, Marcos and Tuia, 2018; Corcoran et al., 2019; Corcoran et al., 2021; Preston et al., 2021), such as Norwegian red deer (*Cervus elaphus*, Figure 1.1). Despite the importance of population estimates, Norwegian authorities are lacking adequate data on the abundance and density of the country's red deer populations. Current estimates have primarily been obtained using statistics

from hunting and the reported number of animals observed during hunting. Alas, these estimates only provide trends associated with unknown degrees of uncertainties and cannot be reliably used to quantify population abundances (Solberg et al. 2019, p. 44). Some red deer municipalities have tried to address this issue by means of on-road spotlight surveys of deer coming out of the woods and into the agricultural fields (known as “spring counts”; Mysterud et al., 2007; Solberg et al., 2019, p. 33). Besides only providing a minimum estimate of population size (Solberg et al., 2019, p. 33), sampling from road-based surveys seems to be an unreliable method and has been criticized for leading to inaccurate, imprecise, and biased estimates as deer distribution is influenced by roads (Mysterud et al., 2007; Witczuk et al., 2018; Preston et al., 2021). Thus, new data collection methods are needed to address the aforementioned issues concerning population estimates.



Figure 1.1: Image of red deer stag with GPS-collar taken in July 2012 in Norway. Photo: Nils Olav Talgøy.

A promising direction in population detection, abundance, and density estimation is the employment of unmanned aerial vehicles (UAVs, also known as drones, unmanned aerial systems [UAS], and remotely piloted aircrafts [RPA]). Although still in the trial phase, the last few years have seen a rapid uptake and remarkable progress in the use of UAVs for ecological data collection (Hodgson et al., 2018; Schroeder et al., 2020). The feasibility of this tool for detection, abundance and distribution estimates have successfully been explored for several animal species (Christie et al., 2016; Corcoran et al., 2021), including red deer

(Witczuk et al. 2018), white-tailed deer (*Odocoileus virginianus*; Chrétien, Théau and Ménard, 2016; Beaver et al., 2020; Preston et al., 2021), and elk (*Cervus canadensis*; Graves et al., 2022). Compared to ground-based approaches, results show that UAV technologies are more accurate, precise, and efficient (Linchant et al., 2015; Hodgson et al., 2016; 2018; Beaver et al., 2020; Preston et al., 2021). They produced population estimates with narrower confidence intervals and less bias than traditional data collection methods (Linchant et al., 2015; Hodgson et al., 2016; 2018; Beaver et al., 2020; Preston et al., 2021). In addition, counts obtained from surveys by UAVs have repeatedly given similar or significantly larger estimates than estimates based on ground surveys (Hodgson et al., 2016; Spaan et al., 2019). Overall, UAV surveys increase the ability to detect population trends (Beaver et al., 2020).

1.2 Chronic wasting disease (CWD) and the need for population estimates

The first case of chronic wasting disease (CWD) in Europe was detected in a reindeer (*Rangifer tarandus*) in Nordfjella Zone 1 in southern Norway in 2016 (Benestad et al., 2016). As a consequence of this finding, all the reindeer in the infected population were culled in the fall and winter of 2017 and 2018 (Mysterud and Rolandsen, 2018; Mysterud, Strand and Rolandsen, 2019). CWD is a contagious neurological disease that results in emaciation, abnormal behavior, loss of bodily functions and eventually death (Mysterud and Edmunds, 2019). It is known to infect animals in the deer family such as reindeer, moose (*Alces alces*), and red deer. The course of disease lasts for a minimum of 16 months (Mysterud and Edmunds, 2019; Escobar et al., 2020). The disease is transmitted both directly by animal-to-animal contact and indirectly through the environment (Miller and Williams, 2003; Miller et al., 2004). Furthermore, the resistant nature of the CWD infectious agents, termed prions, represents a significant obstacle when it comes to eradicating CWD from contaminated areas – in this case the Nordfjella region (Ytrehus et al., 2018).

Thus, there is now a great concern that the moose and red deer populations found in the area will contract CWD from prions that remain in the environment. Reducing the density of susceptible animals in the areas where CWD has been found, will reduce the likelihood of spillover to red deer and moose from environmental reservoirs (Chronic Wasting Disease Alliance, 2020; Solberg et al. 2019, p. 3). As a means to lower the probability of such a spillover of the disease, the Norwegian Environment Agency, recommend that the populations of moose and red deer in the 15 municipalities comprising the Nordfjella CWD zone are reduced to less than one deer per km² (Miljødirektoratet, 2020; Solberg and Rolandsen, 2020). However, as previously stated, the abundance and density estimates of red deer in Norway are

inadequate, which creates difficulties in terms of making informed decisions related to reducing the population (and consequently the disease threat). Hence, the need for a more direct method to estimate population size and density in the areas in and close to the CWD contaminated Nordfjella Zone 1 is immediate.

1.3 Aim of thesis

The aim of this study is to develop a method that can be used to provide more reliable population estimates of wild deer by the use of UAVs. The UAVs will be used to gather data on red deer populations in Lærdal, Norway, which are at risk of a CWD outbreak. The study will make use of daylight red-green-blue (RGB) camera in addition to thermal camera and flights will mostly be performed above steep terrain. Moreover, the study will largely make use of counts by two observers in order to estimate detection probability (Nichols et al., 2000). To make further inferences about detection probability, the data will be supplemented by counts made from aerial images of a known number of fenced deer (Figure 1.2).



Figure 1.2: Tame red deer at Lund Deer Farm in Lærdal, Norway. Photo: Julie Bommerlund.

2 Methods

2.1 Study area

The fieldwork was conducted in the municipality of Lærdal in Vestland county, Norway. Lærdal has a relatively dry climate, with an annual precipitation of 400-500 mm (Thorsnæs et al., 2022). The mean temperature for 2021 was 7.1 °C (0.4 °C above normal mean annual temperature), while the temperature during the sampling period averaged 4.5 °C. A 51 km long valley stretches from the north-western to north-eastern part of the municipality (Mysterud et al., 2021; Figure 2.1). The bottom of the valley mostly consists of agricultural fields and grass meadows, which are often used by red deer for feeding and travelling, as well as settlements and roads (Figure 2.1). The slope of the mountains surrounding the valley floor are covered with forest (Figure 2.1). Birch (*Betula* sp.) and alder (*Alnus incana*) constitute most of this woodland, while some coniferous trees, in particular Scots pine (*Pinus sylvestris*) and Norway spruce (*Picea abies*), are scattered around (Mysterud et al., 2021).

Of the 15 municipalities that are part of the Nordfjella CWD zone, Lærdal is the municipality with the densest red deer population (Solberg et al., 2019). Owing to this high deer density, the municipality currently consist of 47 management areas, or “vald”, for deer hunting (Årdal municipality, Lærdal municipality and Aurland municipality, 2011, p. 9). These hunting grounds stretch from the valley floor, up the mountains, and, legally, above the tree line. During winter, the red deer aggregate along the valley close to agricultural areas (Godvik et al., 2009; Lande et al., 2014). In summer, the red deer move ranges to the mainly deciduous forests (Mysterud et al., 2021). The forested areas and mountains on the south side of the valley overlap with the area previously occupied by the chronic wasting disease (CWD) infected reindeer, Nordfjella Zone 1, and thus, Lærdal contains deer that may have been inside or close to the area used by CWD infected reindeer (Solberg et al., 2019; Figure 2.1).

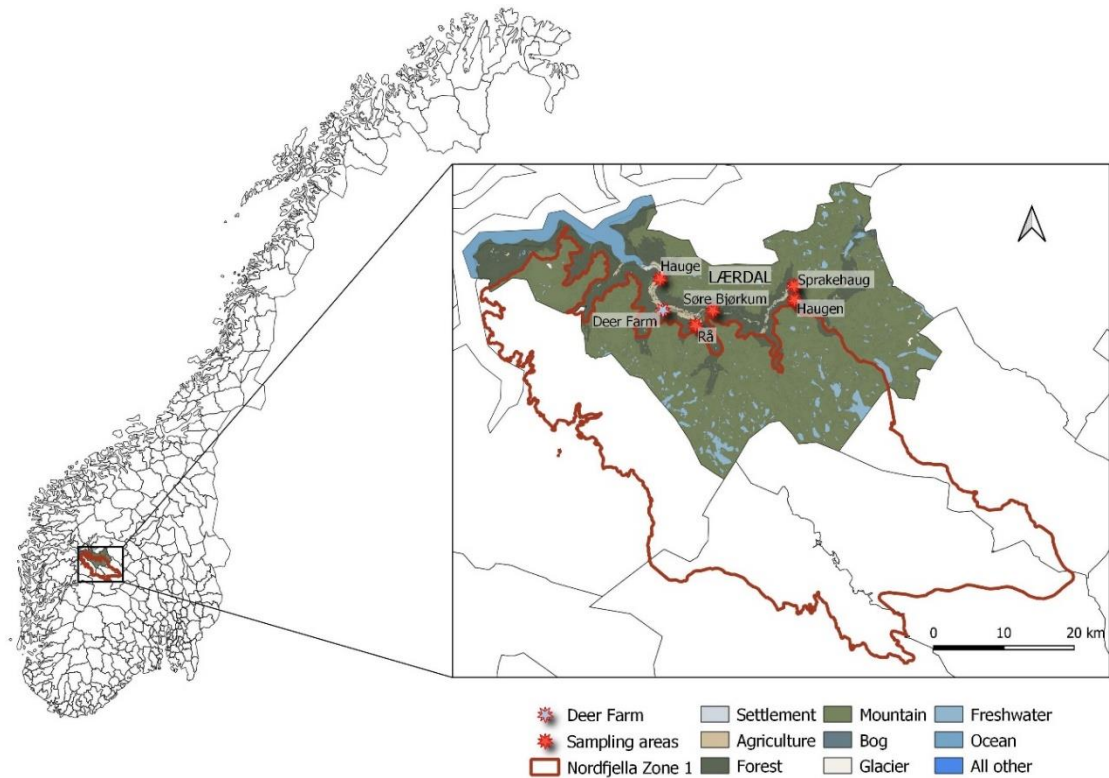


Figure 2.1: An overview of the study area in Lærdal municipality in the Nordfjella region, Norway. The figure also shows detailed positions of the deer farm and sampling areas.

2.2 Spatial sampling design

As part of the project “Red deer in Nordfjella”, more than 30 red deer in the Nordfjella-region have been instrumented with global positioning system (GPS) collars. Selection of sampling areas was based on whether the areas were overlapping with the ranges of such GPS-collared deer. Overlaps were desirable to potentially capture images with GPS-collared deer present to improve inferences about detection errors. It was also preferable to have at least one area overlapping with Nordfjella Zone 1. Thus, sampling areas were not randomly selected, but each area could be considered a different case study. Five areas were chosen: Hauge, Haugen, Rå, Sprakehaug, and Søre Bjørkum (Figure 2.1; Figure 2.2). With some exceptions, every area was sampled on one occasion during day and one occasion during night both in March and April of 2021 (Table 2.1; Table 2.2). Haugen was sampled twice during day and night in March. The intention was to follow the same procedure in April, but weather conditions and time constraints made this unfeasible. For the same reasons, Sprakehaug was not sampled at night in March. Hauge was exclusively sampled on one occasion during nighttime in March due to challenges associated with the site’s terrain as well as weather conditions.

In addition to the selected sampling areas, three flights were also performed above Lund Deer Farm. At the deer farm, the number of red deer was known, aiding estimation of detection probability. At time of flights, the enclosure contained a total of 117 red deer: 2 stags with antlers, 45 hinds, 35 yearlings (16-17 young stags and the rest yearling hinds), and 35 calves of the year. The size of the enclosure was about 5 hectares according to the landowner (Ole Bjørn Grøthe, 2022, pers. comm. 3 March).



Figure 2.2: Image of Haugen in Lærdal, Norway, a sampling area used in surveys. The image was taken in March 2021 using the drone DJI Mavic 2 Enterprise Dual.

On each of the five sampling areas, a total of six routes, three during daytime and three during nighttime, were initially chosen for survey flights. However, the number varied from area to area because of challenging terrain, unsuitable weather, and the unmanned aerial vehicle's (UAV's) battery usage (Table 2.1; Table 2.2; see Appendix A for full list of surveys). Including the three flights from the deer farm, a total of 61 surveys were completed, 31 during the day and 30 during the night (Table 2.1; Table 2.2). During night, the red deer cluster at the fields at the bottom of the valley. Thus, the nighttime survey flights were performed above infields using an infrared (IR) camera. The daytime survey flights were, in

contrast, performed along the slope of the mountains using a daylight red-green-blue (RGB) camera.

Table 2.1: An overview of the areas sampled during daytime divided into the months the areas were sampled. Each sampling area consisted of up to 5 ‘Route’s. ‘Mean elevation’ is the mean elevation of all sites within the route (see section 2.5.1 for more information about sites), ‘No. surveys’ is the number of survey flights completed for each route, ‘No. sites’ is the number of sites for each survey, and ‘Mean area’ (in hectare) is the mean area of all sites combined in a route.

Sampling area	Route	Mean elevation (MASL)	March			April		
			No. surveys	No. sites	Mean area (ha)	No. surveys	No. sites	Mean area (ha)
Deer Farm	1	80	2	21, 10	3.02	0	NA	NA
Haugen	1	546	2	7, 9	7.00	1	10	7.01
	2	497	2	6, 8	5.90	1	8	6.00
	3	552	2	6, 7	6.62	1	6	6.55
Rå	1	146	1	10	3.78	1	10	2.17
	2	143	1	8	3.06	1	8	2.47
	3	114	1	6	2.56	1	17	2.11
Sprakehaug	1	568	1	7	5.45	0	NA	NA
	2	671	1	5	6.10	0	NA	NA
	3	475	1	5	6.42	1	4	6.07
	4	568	1	7	5.85	1	7	5.83
	5	614	1	7	6.40	1	6	6.15
Søre Bjørkum	1	228	1	28	7.77	1	24	4.95
Bjørkum	2	265	1	32	7.43	1	16*	7.20
	3	254	1	7	7.93	0	NA	NA
	4	164	1	20	6.90	0	NA	NA

*Flight interrupted and stopped by crash.

Table 2.2: An overview of the areas sampled during nighttime divided into the months the areas were sampled. Each sampling area consisted of up to 4 ‘Route’s. ‘Mean elevation’ is the mean elevation of the route, ‘No. survey’ is the number of survey flights completed for each route, ‘Mean area’ (in hectare) is the mean area of a route as given by the flight planning app (except for Deer Farm, where the area is the size of the enclosure). Two of three nighttime flights completed in Sprakehaug in April have unknown route areas as the flights were cut short due to weather and battery issues, i.e., the areas given by the flight planning app were inflated.

Sampling area	Route	Max elevation (MASL)	March		April	
			No. surveys	Mean area (ha)	No. surveys	Mean area (ha)
Deer Farm	1	80	1	5.0	0	NA
Hauge	1	20	0	NA	1	2.09
	2	20	0	NA	1	3.50
	3	20	0	NA	1	1.53
Haugen	1	441	2	2.42	1	2.42
	2	444	2	2.38	1	2.38
	3	459	2	2.42	1	2.42
Rå	1	119	1	4.39	1	4.39
	2	108	1	3.34	1	3.34
	3	107.5	1	3.79	1	3.79
Sprakehaug	1	442	0	NA	1	-
	2	442	0	NA	1	-
	3	442	0	NA	1	3.34
Søre Bjørkum	1	134	1	1.48	1	1.48
	2	139	1	0.77	1	0.77
	3	154	1	1.63	1	1.63
	4	140	1	0.57	1	0.57

2.3 Equipment: UAVs and terrain model

With the ability to maneuver the UAV in closely spaced grid patterns, multirotor drones offer greater control over flight planning than fixed-wing drones (Corcoran et al., 2021). Compared to fixed-wing drones, multirotor drones also allow for higher ground resolution as these drones can be flown at a lower altitude and speed (Corcoran et al., 2021). Thus, two multirotor consumer drones were chosen for sampling: DJI Mavic 2 Pro and DJI Mavic 2 Enterprise Dual (Figure 2.3). DJI Mavic 2 Pro has an excellent camera for daylight photography, while DJI Mavic 2 Enterprise Dual has both a daylight camera and a thermal camera that simultaneously take pictures. The initial plan was therefore to use the Pro-drone for the daylight surveys and the Enterprise Dual-drone for the nighttime surveys. However, the Pro-drone collided with a tree early in the fieldwork and was no longer operable. Thus, all survey flights from after the 8th of March 2021 were completed using the Enterprise Dual-drone.



Figure 2.3: The DJI Mavic 2 Enterprise Dual Drone. Image taken in Haugen, Lærdal, Norway. Photo: Julie Bommerlund.

When employed, the UAV's remote controller was mounted to an iPad Mini. The app DJI 4.0 was used to control the settings of the DJI Mavic 2 Pro, and DJI Pilot was used to control the settings of the DJI Mavic 2 Enterprise Dual. Both UAVs used Map Pilot, a flight

control app and companion app of the mapping process platform Maps Made Easy, to set up and complete the flight routes. Before each flight, Map Pilot was set to give an image overlap of 80% in the direction of the flight (forelap) and 60% between survey lines (sidelap). (See Appendix C for full description of the UAVs' and apps' settings during flight.)

For terrain awareness, Map Pilot by default uses Shuttle Radar Topography Mission (SRTM) data from NASA. This data's resolution is only 30 m/pixel (EROS, 2018), which is quite coarse in the steep and rugged terrain of Lærdal. However, it is possible to use other digital elevation models (DEMs) in Map Pilot. Hence, after a second (this time no-damage) crash, the official terrain model from the Norwegian Mapping Authority (2021), which has a detail level of 10 m/pixel, was imported. This was done by downloading the DEM-files covering Lærdal from the map catalogue Geonorge and using QGIS to merge the files into one raster file as well as to crop the areas of interest, i.e., the sampling areas. The selected areas were then separately saved in the correct projection (from UTM to latitude/longitude and coordinate reference system 4326). Following the guidelines of the mapping software provider Drones Made Easy (2022), the new terrain data was uploaded to a private account in Maps Made Easy. Finally, the data was pulled from the Maps Made Easy account and used by Map Pilot for terrain awareness during flights. All survey flights completed after the 14th of March 2021 used the terrain model from the Norwegian Mapping Authority instead of the default model from NASA.

2.4 Survey flights

Numerous considerations had to be taken into account when deciding upon the routes of the daytime survey flights: Flights behind knolls were not possible as the UAV and the remote controller communicate via radio frequency signals. Flights close to high voltage power lines could not be performed as power lines might disrupt the signals. The UAV could not fly too close to cliffs and crevasses due to high risk of crash. And finally, the UAV had to remain within visual line of sight. The routes of the nighttime survey flights were, on the other hand, determined based on a set of rules. Firstly, the routes were chosen based on whether the fields were visible from the road in case it would be desirable to compare the obtained survey data with data from the annual spring counts (where deer are counted from the roadside). Secondly, only fields that, at the shortest distance, were less than 100 m from the forest boundary were used for surveys. Thirdly, fields surrounded by deer fences were for obvious reasons avoided. As with sampling areas, both daytime and nighttime survey flight routes were chosen based on the movement of GPS-collared deer.

The UAV batteries were a limitation for both types of survey flights. With the five batteries available during sampling, it was possible to fly 1.5-2.0 hours depending on the weather (wind and cold weather cause the batteries to drain faster). This meant that the three survey flights completed per sampling occasion could only last for about 30 minutes each. Additionally, the flights had to be executed in a 2-hour window: Normally, location data from GPS-collared deer are received every hour. However, for a 2-hour period during sampling of areas with such deer, the coordinates of the corresponding deer were set to be recorded every 2 minutes instead. The frequent recording of positions required more of the GPS tracker batteries, and thus the limit of 2 hours was imposed. The survey flights also had to be conducted in time periods without precipitation or strong winds (less than 8 m/s).

Furthermore, to avoid the thermal camera from picking up infrared radiation emitted by heated rocks, trees, etc., the nighttime flights had to be performed early in the morning, as opposed to late at night, so that such objects' temperatures could become sufficiently lower than the surface temperature of deer before sampling (Seymour et al., 2017; Kays et al., 2019; Spaan et al., 2019; Takehiko et al., 2022). Spectral confusion from thermal heating of landscape elements still made it difficult to reliably distinguish deer in a few cases where potential individuals were standing close to a forest boundary. In these situations, the potential individual was not counted unless movement eventually had been detected. The latter was not an issue for the daytime surveys; though, optimally the daytime flights had to be completed in the middle of the day when the sun was at its brightest. In these lighting conditions, the UAVs could be flown 60 m above ground level (AGL), instead of 40 m, and still capture images of good quality. The extra height of 20 m was essential to avoid collisions in the uneven terrain of the mountain slopes where the daytime surveys were sampled. Thus, when lighting allowed for it, the daytime flights were set at 60 m AGL (see Table A1 in Appendix A). All nighttime flights were set at 40 m AGL.

With all mentioned challenges, limitations, rules, and settings accounted for, the routes were created. Supported by observations made of the sampling areas and elevation data from the Norwegian Mapping Authority, the computer program Google Earth was used to determine and draw the perimeters of the survey flights' routes (see Appendix A). The resulting projects were subsequently exported from Google Earth as KML-files, sent by email to the iPad mounted to the UAV's remote controller, and uploaded to the app Map Pilot. Using Map Pilot, the routes of the survey flights were then drawn inside their respective perimeters. After a few flights had been completed, it became clear that the potential for

collision during daytime would be reduced by flying horizontal across the slope of the mountains, as opposed to up and down along the slope, and by starting the flights at their routes' highest point. Thus, all routes drawn following this point were created accordingly.

In order to comply with the legal requirement/national legislation of maintaining visual line of sight with the UAV at all times, a second observer, whose sole purpose was to watch the aircraft, was present during all flights. During the nighttime survey flights, the UAV operator was then free to count and record the number of red deer observed on the screen as well as note the deer's behavior. For the daytime survey flights, no deer were observed during the flights, but visible deer were later recorded from the images (see below).

2.5 Analysis

2.5.1 Selecting focal images

As mentioned in section 2.3, the UAVs were set to give significant overlap between the images of a flight, both forward/backward and sideways. The idea was to align and mosaic the photos from each survey flight, using the photogrammetry tool AgiSoft Metashape Professional (v1.7.5, 2021), in order to position each deer observed in the images. Attempts to do so were, however, unsuccessful: images from nighttime survey flights would not align and the orthomosaics produced from the daytime survey flights appeared distorted and incomplete (probably largely due to the presence of trees as well as inaccurate global navigation satellite system [GNSS] positioning of the drone and poor overlap between some images). Instead, independent, non-overlapping "focal images" from the daytime survey flights were selected for further analysis. As the actual overlap between the aerial photos were not precisely 60% and 80% but varied substantially with the slope of the terrain, manual selection of these focal images was decided to be the most feasible way forward for the most consistent and accurate selection. It was not possible to confidently select non-overlapping focal images from the nighttime surveys nor confidently determine the area covered by the surveys. Because of this, the images from the nighttime surveys were not used further in the analysis.

For every daytime survey flight, the positions of the images in relation to each other were plotted as rows (direction of flight) and columns (change of direction; Figure 2.4). All plots in this study were made using either R v4.1.1 or v4.2.0 (R Core Team, 2021). The first image of each flight was considered a focal image and the area covered by a focal image was considered a 'site'. Subsequent non-overlapping focal images in a row were determined based on distinct features in the images (trees, boulders, streams, etc.). Once every photo of a row

had been inspected, the procedure was repeated for every third row – two rows were skipped to avoid sidewise overlap. Altogether, 332 sites were selected.



Figure 2.4: Example of image positions in a survey flight. Each number represents an image retrieved from survey 20210411_Raa_RGB_40m_#2. The red circles indicate focal images selected using the procedure described above. Top side of the figure is north. The upper row of numbers is the lowest point of the flight, and the bottom row of numbers is the highest.

2.5.2 Detecting and recording red deer

The counts were expected to contain false-negative detection errors in the form of both perception errors and availability bias (the latter will be discussed in section 2.5.4). Perception error refers to a situation where an individual is present in the sampled area and visible in the image but still missed in the counts (Brack, Kindel and Oliveira, 2018). Such failure to detect individuals might be caused by observer fatigue (Brack, Kindel and Oliveira, 2018). With this in mind, red deer were counted using the independent double-observer protocol. When following such a protocol, two observers “make independent detections of individuals during point counts of a fixed time and then, after the counting, reconcile their lists” (Kéry and Royle, 2016, p. 318). In this case, each observer went through the UAV images and recorded unique red deer by noting their location on the images. By following this approach, each

observed individual could be classified as either “seen only by observer 1”, “seen only by observer 2”, or “seen by both observers”. This makes it possible to estimate observer specific detection probabilities and hence also the probability that a deer would be detected by at least one of the observers (due to independent detections). Each observer followed the guidelines as given below.

All images (not just the focal images) in the selected rows, i.e., the rows containing the focal images, from the daytime flights were successively opened in ImageJ (Schneider, Rasband and Eliceiri, 2012) and searched for red deer. Once a deer was detected, ImageJ’s multi-point tool was used to mark what was inferred to be the head of the animal in the corresponding focal image. To avoid false positives, potential individuals were *not* marked if the observer had any doubts as to whether the observed entity was a red deer or something else. However, in several cases, preceding and following images overlapping with a focal image could be used to establish if it was indeed a deer that had been observed on the focal image. In some instances, an individual was only detectable in the image/images before and/or after the focal image. That is, the deer was detected in an area overlapping with a focal image but hidden (e.g., by tree trunks or forest canopy) in the focal image itself. To avoid registering the same individual twice (by the two observers), such individuals were always marked in the *first* photo in which they were visible when looking at the images in the order they were captured (even if the observer initially overlooked the deer in this image).

Animals were typically recognized by the red deer’s cream/white heart-shaped rump as well as the dark grey stripe running along the back and darkening towards the head (Figure 2.5). Some individuals, especially those detected on a snow surface, were easily distinguishable and the presence or absence of antlers was unambiguous (Figure 2.5). Red deer in the snow could also be more easily found by following the deer tracks in the snow. Moreover, for daytime flights where the DJI Mavic 2 Enterprise Dual drone had been used, thermal imagery had also been captured and these images could be used to help detect deer in snow landscape. These IR images did not show all the deer that were detected in the corresponding RGB images and could consequently only be used as a supporting tool. In landscapes without snow, the thermal images were of no support as objects that retained heat (e.g., rocks and trees) were, according to the camera, giving of the same level of infrared radiation as deer. Thus, thermal-imaging cameras may be better suited for manual flights.



Figure 2.5: Examples of UAV derived imagery with red deer detected in image. Image A shows several deer in a fenced area in Lærdal from 40 m AGL. The red circles in image A indicate the deer focused on in image B. Image C shows three deer in Haugen, Lærdal from 60 m AGL. The red circle in image C indicates the deer focused on in image D. Both images were captured in March 2021 using DJI Mavic 2 Pro and DJI Mavic 2 Enterprise Dual, respectively.

Based on the presence/absence of antlers and the size compared to other deer in the same image or flight, the deer were divided into four categories: 0 – Hind; 1 – Stag; 2 – Calf; and 3 – Uncertain. Notably, as Norwegian red deer stags start shedding their antlers in April (Hjortevilt, n.d.), adult individuals observed on images from the April-flights could not confidently be categorized as hind or stag unless antlers were visible. Thus, such individuals were by default categorized as “3 – Uncertain”. ImageJ’s multi-point counter was set according to the individual’s determined category (0, 1, 2, or 3) before the individual was marked.

When no more individuals could be confidently detected in a focal image, the marked image was saved as a TIF-file and the results report saved as a CSV-file. In addition, for each deer in an image the following was recorded:

- folder name
- focal image number
- image number (when a deer was detected in a focal image, image number and focal image number were identical)
- category of the deer (0, 1, 2, or 3)
- the X- and Y-coordinates of the deer in the image
- whether the deer was standing on snow surface (0 or 1)
- whether the deer was detectable (0 or 1) or unavailable (NA) in the focal image

With regards to the latter, a deer only needed to be visible in one of the preceding/following images to be recorded as detected – even if it was not the image immediately preceding/following the focal image. Furthermore, one observer also noted the deer’s behavioral responses to the UAV.

2.5.3 Making count data with site covariates

The files containing count data from both observers were uploaded to R (R Core Team, 2021), where the following process was completed: Deer marked in separate, unique images by the observers, were registered as seen only by observer 1 or 2, depending on which observer had marked the deer. For images where both observers had marked deer, a matrix with Euclidian distances (in image pixels) between deer marked by observer 1 and deer marked by observer 2 were calculated. Deer marked by the two observers as more than 200 pixels apart were always considered to be different individuals, while deer marked as less than 200 pixels apart were considered the same individual. When one individual was less than 200 pixels apart from two or more animals, it was matched with the closest individual (see Appendix D for details). Finally, the obtained data was aggregated to solely contain information about focal images, that is, deer observed only in non-focal images were added as counts to the focal images by which they were covered. Thus, the dataset contained counts of deer seen by both observers, only observer 1, and only observer 2 for each focal image.

As it was not possible to use photogrammetric technique to recover spatial information from the UAV images, a projection method to estimate the spatial coverage of any given image was developed. Knowing the drone flight elevation (from barometric sensor), position and orientation angle (pitch, yaw, and roll), as well as the camera optical properties, an image could be projected onto a DEM model at a resolution of 0.1 m/pixel (i.e., 1 pixel represented 0.01 m²; Figure 2.6). Given the low positioning accuracy of the drone (code base GPS) and

the difficulty to identify objects that could be used for georeferencing, images at the start or end of flight lines, likely crossing a road or river, were used to manually adjust projection parameters. Once projected (Figure 2.6), the *raster* package (v2.0-12; Hijmans and van Etten, 2012) in R was used to compute the area by counting the pixels in each of the projected images and multiplying that number by the area covered by a single pixel (0.01 m²). Regarding the images from the deer farm, the areas outside the enclosure had been painted black, using Paint 3D (Microsoft, 2017), before importing them to R in order to exclude these regions from the total area. Next, DEMs from the Norwegian Mapping Authority (2021) were imported into R to extract elevation at each image pixel in the focal images. For each focal image, the following information was computed: mean elevation, minimum elevation, maximum elevation, mean aspect, and mean slope.

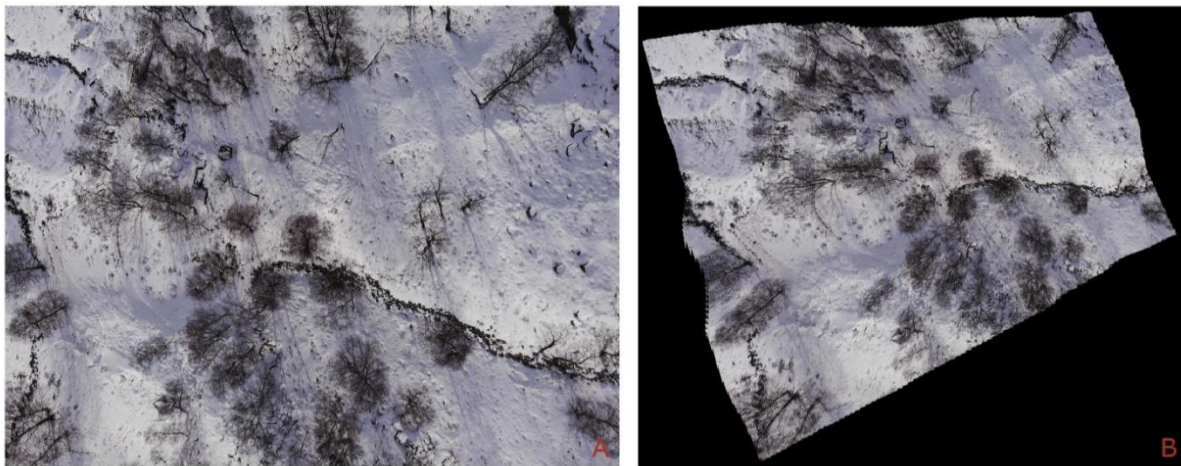


Figure 2.6: Image A is an original focal image, while image B is the same image after projection of a DEM. There is a lower altitude (i.e., further from the drone) on the left side of the images, hence, image B is wider on this side. The original image was captured in Haugen, Lærdal, Norway in March 2021 using DJI Mavic 2 Enterprise Dual.

In order to determine the sites' distances to the forest and agricultural field boundaries, line strings and polygons with these boundaries were manually drawn in Google Earth for each sampling area (Figure 2.7). All Google Earth-images used as templates to create these boundaries were captured in July of 2019 or later (Google Earth V 7.3.3, 2020a). Using QGIS, the line strings and polygons were converted to shapefiles and raster-files, respectively, before they were imported to R. From these files, the following was computed for each focal image: the distance to the agricultural field and the distance to the end of the forest at the site's mean position, the site's mean distance to the field and to the end of the forest, minimum distance to the field and to the end of forest, and maximum distance to the field and

to the end of forest. Before importing any of the projected images, DEM-files, and shapefiles to R it was important that all files were saved with the same coordinate reference system settings: EPSG:25833-ETRS89 / UTM zone 33N.



Figure 2.7: Example map showing line strings with the agricultural field and forest boundaries at Haugen, Lærdal, Norway (Google Earth V 7.3.3, 2020a). The red line represents the field boundary, and the white line represents the forest boundary. Top side of map is north.

Next, previously recorded flight data was imported to R. For each survey flight, this data contained information about sampling area, route number, month of flight (March or April), date of flight, weather during flight (sunny, mostly sunny, slightly overcast, mostly overcast, or overcast), temperature during flight, and whether the survey area was covered with snow during sampling. The latter was considered true if a majority of the aerial photos from the survey flight displayed a snow-covered surface. The resulting list of all focal images with computed area, elevation data, agricultural field and forest boundary data, and flight data was then added to the dataset containing information about counts (full script for the procedure can be found in Appendix D2).

2.5.4 Considering availability bias

As mentioned in section 2.5.2, the counts were expected to be prone to availability bias. In this study, availability bias refers to the situation where “an individual is present in the sampled area but unavailable for counts” (Brack, Kindel and Oliveira, 2018). Such a situation might occur when a red deer is hidden in the images by vegetation. In other words, the red deer that were 100% covered by vegetation in all images would not be counted by either observer. This potential availability bias, when not accounted for in the model, would cause the model to only estimate the density of animals that were observable in the aerial photos. The thought was that this false-negative error could be corrected, i.e., that “availability” could be included in the model and the density of *all* animals could be estimated, by using the location data retrieved from GPS-tracking of the collared red deer. That is, the location of GPS-collared deer could be compared to the location of detected deer in order to estimate availability probability.

For this to be possible, it was essential that the GPS-collared deer had been present in the survey areas during sampling. After each sampling occasion, a TXT-file with coordinates was received from NIBIO (the Norwegian Institute of Bioeconomy Research) for every GPS-collared deer whose home range overlapped with the sampled study area. All files contained information about the individual deer’s positions several hours before, during, and after sampling. During sampling, the positions had been logged every 2-minute. Next, AgiSoft Metashape Professional (2021) was used to create orthomosaics of the daytime survey flights. Each orthomosaic and their corresponding file/files with GPS-positions were then uploaded to QGIS to check if the GPS-collared deer had in fact been present during sampling (Figure 2.8). Figure 2.8 clearly shows that GPS-collared deer were present when the survey took place. However, the presence of GPS-collared deer during sampling could only be confidently confirmed in 2 of the surveys completed above areas with wild red deer (see Appendix C). During most sampling occasions, the GPS-collared deer were at considerable distances from the survey flight routes. Thus, I concluded that there was not enough data to make reasonable estimates about availability bias from GPS-tracking.

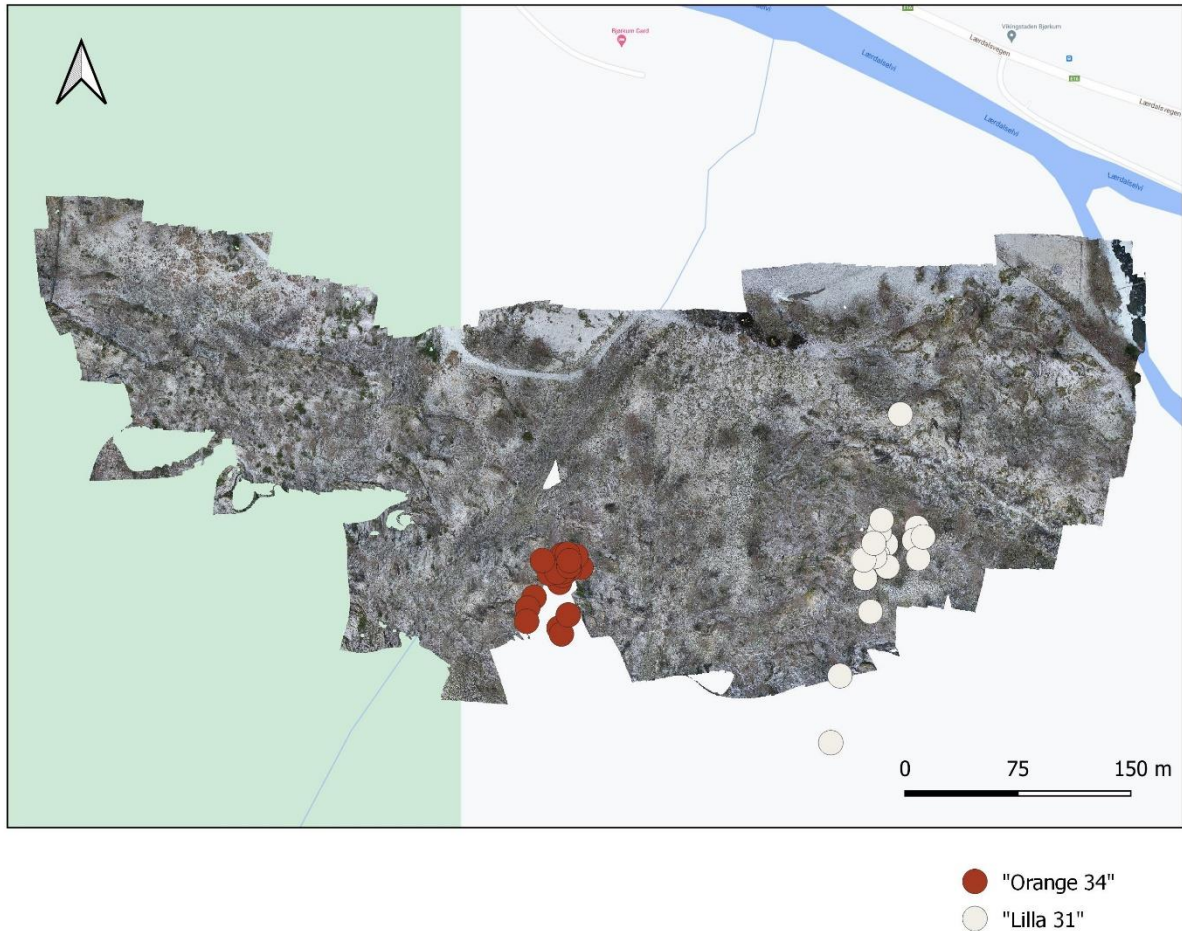


Figure 2.8: Example image showing how presence/absence of GPS-collared deer during sampling was determined. The map includes an orthomosaic from survey 20210307_Soere_Bjoerkum_RGB_60m_#1 as well as GPS-positions of the GPS-collared deer “Orange 34” and “Lilla 31” at 2-minute intervals during time of survey. The map was created using QGIS Geographic Information System (QGIS Development Team, 2020).

Availability bias could potentially have been estimated by use of multiple overlapping aerial images as in the study by Williams et al. (2017). In this approach, estimates about availability is obtained using counts of individuals in the intersection of the overlapping images and fitted (with other data) in an inhomogeneous Poisson process model in an N-mixture model framework (Williams et al., 2017). This method was not used as simplified calculations using the count data suggested that the availability bias was negligible. For both observers, I assessed availability bias by computing the proportion of deer present in the area covered by the focal images (deer seen in the focal images, preceding images, and/or following images) that also were visible in the focal images (seen in the focal images). Of 121 individuals that were seen by observer 1 in areas of the preceding or following images that were overlapping with the focal image, 112 individuals (92.6 %) were also visible in the focal image. Hence, it appears that there would be a rather small chance that an individual present

on the ground would be hidden (i.e., unavailable) in all images covering the ground from different angles along the flight path. When making the assumption that most deer would be exposed to three pictures taken from different angles, and that the probability of being visible in each of them is 0.926, then the probability of being visible in at least one of the three images would be $1 - (1 - 0.926)^3 = 0.9996$ or approximately 99.96 %. For observer 2, this probability was approximately 99.84 %. However, the assumption may be conservative as many deer were visible in more than three images. In other words, these calculations indicated that availability bias was not significant, and therefore I did not take availability bias into account in the model.

2.5.5 Statistical modeling

To estimate the density of the wild red deer, a hierarchical state space model (SSM) was fitted to the resulting dataset using Bayesian Markov chain Monte Carlo (MCMC) sampling in R v4.2.0 (R Core Team, 2021) with the R packages *nimble* (v0.12.1; de Valpine et al., 2017; 2022). An SSM consists of two parts: an observation model and a process model. The observation model describes how the data (in this case the observed counts of red deer) have arisen based on a given underlying reality. The process model is a stochastic model of this underlying reality, in this case the spatial variation in red deer density. The object of Bayesian inference is to estimate the multivariate probability distribution of certain parameters, given the data and prior knowledge related to the parameters, i.e., the prior probability distribution. That is, the object is to estimate the posterior probability distribution, $P(\theta|D)$ [θ is all “top level” parameters and D is the data]. This is in contrast to frequentist statistics, which is based on choosing values for the parameters that will maximize $P(D|\theta)$. A 95 % Bayesian confidence interval (CI), known as the credible interval (CRI), does, unlike the frequentist CI, actually contain the target parameter with probability 0.95 (Kéry and Schaub, 2011, p. 37). Furthermore, by using MCMC sampling, simulated samples can be drawn from the posterior distribution, and hence, by summarizing these samples, the resulting mean, standard deviation (SD), and other statistics can be interpreted as the posterior mean, posterior SD, and so forth (Kéry and Schaub, 2011, p. 38). If appropriate convergence of the MCMC chains is obtained, the results represent a random sample from the posterior distribution (Kéry and Schaub, 2011, p. 38). I assessed convergence by using a recommended approach where the trace plots of different simulated iterative sequences are inspected and compared (Gelman et al., 2004, p. 295; see Appendix F for summary of convergence statistics).

The final hierarchical model used in the analysis could mathematically be defined as (full model derivation in Appendix E):

$$\mathbf{y}_i \sim \text{Multinomial}(\boldsymbol{\pi}, Y_i)$$

$$Y_i \sim \text{Binomial}(p^*, N_i)$$

$$N_i \sim \text{Poisson}(\lambda_i a_i)$$

$$\log(\lambda_i) = \mu_i + \varepsilon_i$$

$$\mu_i = \mathbf{x}_i \boldsymbol{\beta}$$

$$\varepsilon_i \sim N(0, \sigma_\varepsilon)$$

Here, \mathbf{y}_i is a vector of length three with the numbers of deer being detected by observer 1, observer 2, or by both observers (disjunct categories) at site i , and $\boldsymbol{\pi}$ is the corresponding multinomial probability vector (i.e., the probabilities of observing a deer in each of the three categories given that the deer is detected by at least one of the observers). Further, Y_i is the total number of individuals detected at the site (i.e., the sum of the elements of \mathbf{y}_i), p^* is the probability that a deer will be detected by at least one of the observers, and N_i is the number of individuals present at the site. Together, the two first lines above make up the double-observer observation model and the remaining lines specify the process model. The number of individuals present at each site, N_i , was assumed to be a Poisson random variable with expectation $\lambda_i a_i$, where a_i is the area of the site. To account for spatial variation in deer densities among sites, deer density λ_i was specified as a log-normal random variable with parameters μ_i and σ_ε , where μ_i was constrained by a linear model, $\mathbf{x}_i \boldsymbol{\beta}$ (\mathbf{x}_i is a vector of predictor variables and $\boldsymbol{\beta}$ holds the coefficient parameters). These latter components make up the overdispersed Poisson process model. With this model, the median density of sites with identical predictor variables \mathbf{x}_i becomes e^{μ_i} and the mean density of such sites become $e^{\mu_i + \sigma_\varepsilon^2/2}$ (the latter is the mean of the log-normal distribution). Since the linear model is on the logarithmic scale of λ_i , I model multiplicative effects on deer densities (i.e., a given absolute difference in \mathbf{x}_i will give a relative difference in deer density).

Several potential predictor variables were evaluated for inclusion in the model: the observed animals' assigned category (hind, calf, stag, or uncertain), each site's mean distance to the agricultural field (henceforth 'field distance'), each site's mean distance to the end of the forest (henceforth 'forest distance'), each site's mean elevation (henceforth 'mean

elevation'), slope, aspect of slope, weather, temperature, snow, route, month, sampling area, route divided into month, and sampling area divided into month. The observed animals' assigned category was eliminated as a predictor variable due to almost all of the individuals being identified as "uncertain". To determine if the remaining variables were expected to have a significant effect on the predicted number of red deer, I used the wild deer data (i.e., data from the enclosure was excluded) to fit a Poisson general linear mixed model (GLMM) for each variable. The Poisson GLMMs were created using the R package *glmmTMB* (v1.7.22; Brooks et al., 2017), and all models had an offset equal to the logarithm of the area in hectare (see example of GLMM in Appendix D4). The GLMMs showed little variation in the number of estimated red deer between routes of one sampling area, unconditional on month. The opposite was true for sampling areas. Hence, in the overdispersed Poisson process model, I imposed the constraint $\mu_i = \mu_{0,s(i)} + x_i\beta$, where $s(i)$ was the sampling area and month of site i . That is, I estimated deer density distributions for each sampling area and month and assumed the expected densities would increase or decrease monotonous with the predictor variable, x_i .

To establish a prior distribution for the parameters, a model similar to the main model was created using only the data from the deer farm (model code can be found in Appendix D4 and model specifications can be found in Appendix E). Here, the mean density, d , was not estimated but set to its known value (there were 117 deer in the 5-hectare enclosure during both flights performed above the enclosure). The red deer density estimates provided by this model were not precise, but this was probably due to the aggregated distribution caused by the feeding station and the limited space within the enclosure. Although parameters describing the deer density distribution (μ_i and σ_ε) were not relevant for the wild deer, I still found it sensible to use the enclosure data to obtain information about detection probabilities. However, I decided to only use the posterior detection probabilities at 60 m AGL, and not 40 m, because very few of the survey flights were performed at 40 m AGL and none of these surveys contained observed red deer. That is, the posterior distributions of the detection probabilities in the enclosure at 60 m AGL were used as basis for the prior distribution of the detection probabilities in the main model. The posterior mean of this parameter was approximately 0.784, while the posterior median was about 0.788 (95 % CRI: 0.670-0.878; see Appendix F for full summary of results). The log-odds of the posterior detection probabilities, η , were obtained, and the mean of these values were calculated to be approximately 1.320 while the standard deviation (SD) was about 0.321. This mean and SD

were then used to specify the priors for the detection probability of observer 1, p_1 , and observer 2, p_2 , in the main model (full derivation in Appendix E):

$$\eta_1 \sim N(\text{mean}(\boldsymbol{\eta}), 1.2 \cdot \text{sd}(\boldsymbol{\eta}))$$

$$\eta_2 \sim N(\text{mean}(\boldsymbol{\eta}), 1.2 \cdot \text{sd}(\boldsymbol{\eta}))$$

$$p_1 = \frac{e^{\eta_1}}{1 + e^{\eta_1}}$$

$$p_2 = \frac{e^{\eta_2}}{1 + e^{\eta_2}}$$

Here, multiplication of the SD with 1.2 was done to account for potential errors in the posteriors obtained from the enclosure data as well as to account for potential differences in detection probability between the enclosed areas and the areas with wild red deer (e.g., caused by observer fatigue from inspecting images with fewer deer or vice versa).

3 Results

3.1 Availability of red deer

The total number of red deer recorded by observer 1 was 128. Of these, 119 were seen in the focal images, with 7 only detected in this category (Table 3.1). 74 were seen in the preceding images and 71 were seen in the following images. 2 deer were detected in both these categories but not in the focal images, 4 only in the preceding images, and 3 only in the following images (for a total of 9 deer detected only in the adjacent images; Table 3.1). The total number of deer recorded by observer 2 was 135. Here, 121 had been seen in the focal images, with 16 detected only in these images (Table 3.1). 72 were seen in the preceding images and 78 were seen in the following images, with 7 deer detected only in each of these categories (for a total of 14 deer detected only in the adjacent images; Table 3.1).

Table 3.1: Contingency tables showing the number of deer seen/not seen in focal images vs. the number of deer seen/not seen in adjacent images by A) observer 1 and B) observer 2.

A	Seen in focal image	Not seen in focal image	B	Seen in focal image	Not seen in focal image
Seen in adjacent image	112	9	Seen in adjacent image	105	14
Not seen in adjacent image	7	-	Not seen in adjacent image	16	-

3.2 Model results

There was a considerable variation in the area covered by the daytime survey sites (focal images) used in the models, both between the sampling areas and within sampling area Søre Bjørkum (Figure 3.1). The sites sampled from Rå generally covered a smaller area than the sites of Haugen, Søre Bjørkum and Sprakehaug (Figure 3.1). This was expected as all survey flights performed at Rå were completed 40 m above ground level (AGL; i.e., not 60 m AGL).

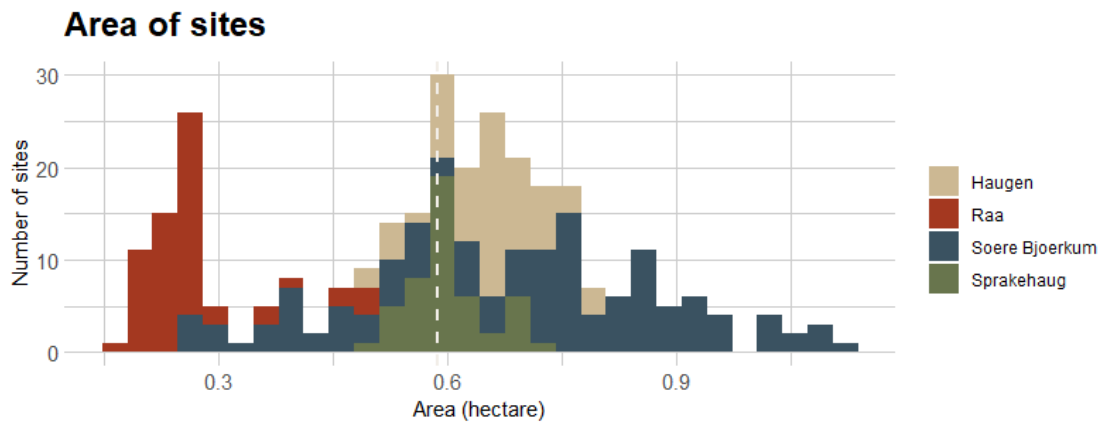


Figure 3.1: The number of sites covering different intervals of area in hectare (1000 hectare = 1 km²). The stippled line represents the mean area covered by the sites. The variation observed within Søre Bjørkum may have been caused by large differences in the slopes within the area, differences in the original terrain map and the terrain map created with DEM-files from the Norwegian Mapping Authority, and/or the last survey where the UAV collided may have been flown at 40 AGL instead of 60 AGL due to an error.

All sampling areas had a large number of sites where no deer was detected (Figure 3.2). In addition, Haugen in March had one site with one deer, two sites with two deer, and three sites with three deer. Haugen in April had three sites with one deer, two sites with two deer, and one site with five deer. Søre Bjørkum had two sites with one deer, seven sites with two deer, and one site with seven deer in March, and only three sites with one deer in April. In March, Sprakehaug had one site with two deer, and in April no deer was counted here. Rå stood out again, with no counted deer at any sites for both months (Figure 3.2)

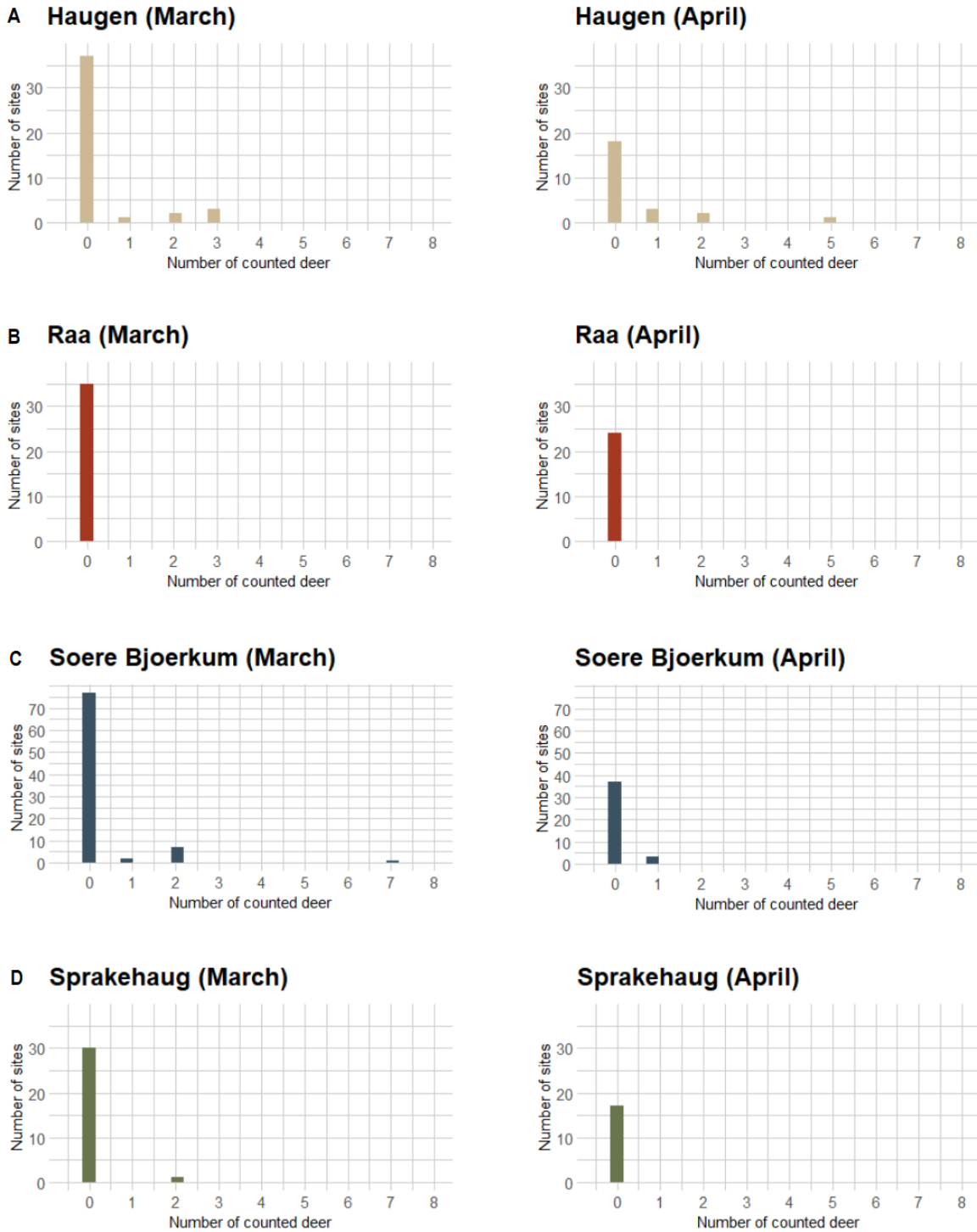


Figure 3.2: The number of red deer counted at each site at the four sampling areas during March and April. The total number of counted deer make up Y_i in the model. Note that the y-axis tick values of Søre Bjørkum are different from the sampling areas.

Only three of the potential predictor variables fitted in the general linear mixed models (GLMMs) provided 95% confidence intervals (CIs) excluding 0 and p-values below 0.05: field distance, mean elevation, and snow. With regards to the latter, both observers' experiences were that red deer were much easier to detect in the snow. Thus, the detection

probabilities of the two observers, p_1 and p_2 , were in the double-observer observation model initially modeled as a function of whether or not a survey area was categorized as having a snow-covered surface. However, I decided to simplify the final model as the 95% critical intervals (CRIs) for the effect (log odds ratio) of snow on the detection probabilities contained 0. Field distance and mean elevation were somewhat correlated, with a correlation coefficient of approximately 0.58. When looking at the correlation between field distance and ‘mean elevation minus mean elevation at the sampling area’ the correlation between the two variables became much stronger at approximately 0.82. As I had included sampling area in the model, it was more correct to take the latter correlation coefficient into consideration. Thus, to avoid problems associated with collinearity in the model, I decided that field distance and mean elevation should be used as predictor variables in two separate models. A third model with forest distance as a predictor variable was also fitted due to biological interest in the effects of this variable on deer density. This variable was also strongly correlated with field distance, with a correlation coefficient of approximately 0.86. The remaining variables were dropped. In other words, three models were fitted using three different predictor variables: field distance, forest distance, and mean elevation.

The model using sites’ mean distances to agricultural fields (field distance) as a predictor variable produced a posterior 95 % CRI for the slope of the variable that excluded 0 (Table 3.2). I.e., it was at least 95 % certain that, during daytime, the density of red deer increased with increasing distance from agricultural fields. In contrast, the posterior 95 % CRIs of the slopes with respect to the standardized predictor variables included 0 for both the model using forest distance (95 % CRI: -0.043 to 0.783) and the model using mean elevation (95 % CRI: -0.426 to 1.028) as predictor variables (see Appendix F for summary of results from all models). Hence, suggesting no strong impact of elevation or distance from the forest boundary on red deer densities. Since both variables also were strongly correlated with field distance, I decided to solely look at the results produced by the model using field distance as predictor variable when moving forward with the analysis.

In this model, the field distance, x , had been standardized by subtracting the mean distance to the field from the observed values and dividing by the standard deviation (SD). The mean distance to the field was approximately 162 m, while the SD was about 106 m. The slope per SD units of field distance (Table 3.2) translates to an increase in estimated red deer density of 62 % (95% CRI: 5% to 150%) when field distance increase with 100 m. The posterior detection probability of observer 1 was estimated to have a mean of about 0.728

(Table 3.2), meaning observer 1 was detecting about 72.8 % of the red deer present at the sites. The posterior mean detection probability of observer 2 was slightly higher, with a value of about 0.840 (Table 3.2). However, the posterior 95 % CRI of observer 2's detection probability overlapped with that of observer 1, with the CRI of observer 2 being 0.757-0.906 and the CRI of observer 1 being 0.627-0.817 (Table 3.2). The posterior means of $\mu_{0,1}$ to $\mu_{0,8}$ ($\mu_{0,i}$) ranged from approximately -5.321 ($\mu_{0,7}$) to -1.513 ($\mu_{0,1}$; Table 3.2).

Table 3.2: Summary of the posterior distribution of the top-level parameters from the model using field distance as predictor variable. β is slope of field distance when the distance, x , is standardized. p_1 is the detection probability of observer 1 and p_2 is the detection probability of observer 2. $\mu_{0,1-8}$ are, respectively, the natural logarithm of deer density at a median site at the mean distance from the field in: (1) Haugen in April, (2) Haugen in March, (3) Rå in April, (4) Rå in March, (5) Søre Bjørkum in April, (6) Søre Bjørkum in March, (7) Sprakehaug in April, and (8) Sprakehaug in March. (Correlation between all parameters can be found in Appendix F).

Parameter	Mean	Median	SD	2.5 %	97.5 %
β	0.516	0.517	0.235	0.052	0.977
p_1	0.728	0.730	0.049	0.627	0.817
p_2	0.840	0.843	0.038	0.757	0.906
$\mu_{0,1}$	-1.513	-1.530	0.501	-2.380	-0.499
$\mu_{0,2}$	-2.099	-2.123	0.435	-2.818	-1.205
$\mu_{0,3}$	-4.931	-5.030	1.237	-6.815	-2.567
$\mu_{0,4}$	-5.144	-5.275	1.152	-6.831	-2.768
$\mu_{0,5}$	-3.481	-3.550	0.515	-4.219	-2.339
$\mu_{0,6}$	-2.644	-2.662	0.395	-3.314	-1.838
$\mu_{0,7}$	-5.321	-5.471	1.075	-6.840	-3.002
$\mu_{0,8}$	-3.755	-3.846	0.574	-4.547	-2.458
σ	1.738	1.734	0.225	1.307	2.191

The relative difference in density between a 2.5 percentile site and a 97.5 percentile site could be found by the equation: $exp(2 * 1.96 * \sigma)$. The parameter σ was estimated to have a posterior mean of approximately 1.738 (95 % CRI: 1.307-2.191) at the standardized distance from the field (162 m; Table 3.2). Consequently, when using this posterior mean, the density of deer was expected to be 910 (95 % CRI: 168-5371) times higher at the 97.5 percentile site than in the 2.5 percentile site. The posterior samples of the parameters β , σ and $\mu_{0,i}$ were used to find the posterior mean and median densities of deer per km² at all sampling areas and at different distances from the field during both months (Figure 3.3). Figure 3.3 shows that the 95 % posterior CRI of all sampling areas were quite wide, however, there were clear differences in densities between sampling areas.

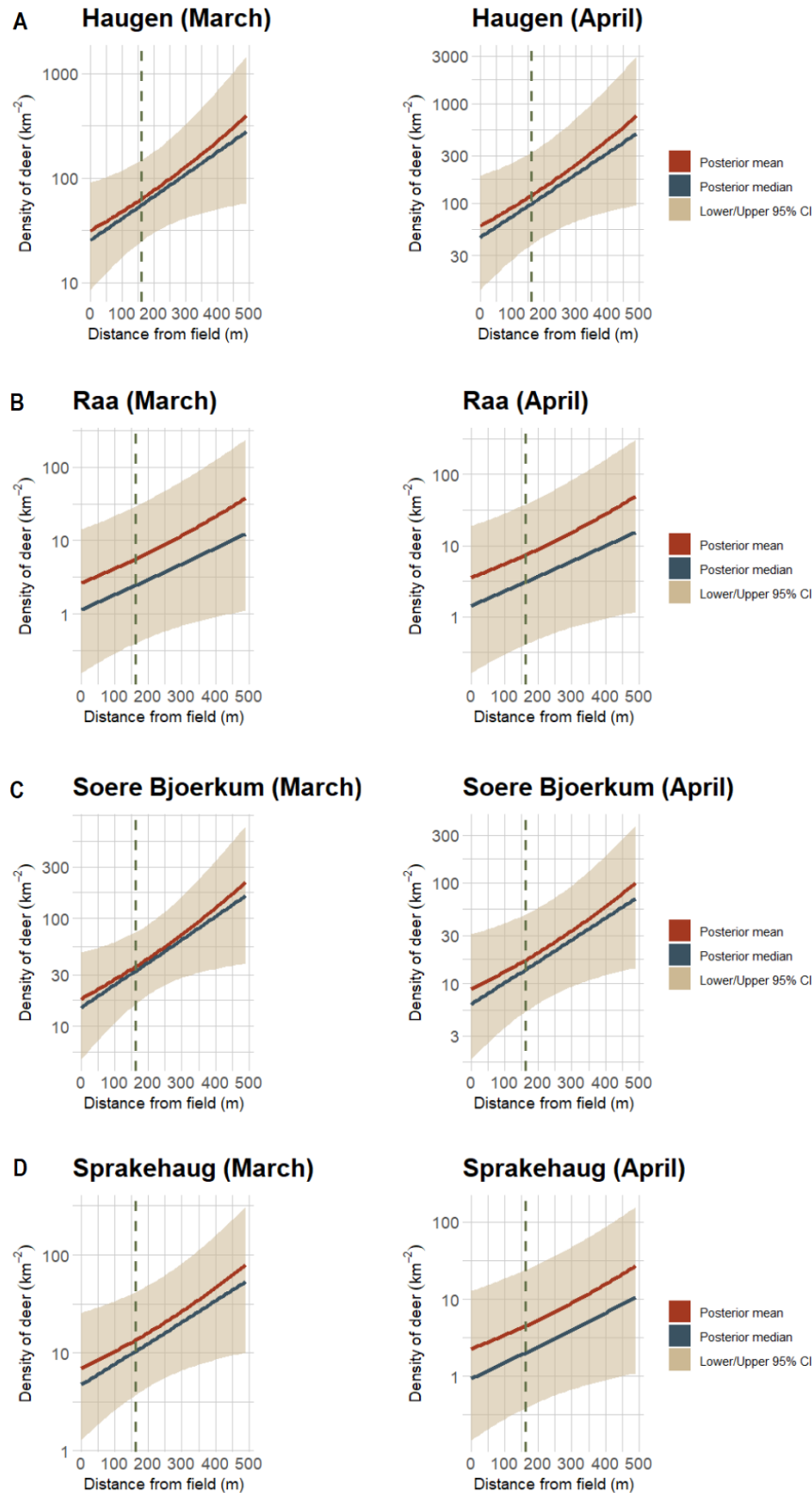


Figure 3.3: Posterior summaries of deer densities per km^2 in the sampling areas in March and April between 0-500 m from the field. Red line represents the posterior mean, blue line represents the posterior median, brown area represents the posterior 95 % CRI, and the stippled line represents the mean of all the sites' combined distances from agricultural fields (approximately 162 m). All sampling areas were located in Lærdal, Norway. Note that the y-axis tick values of the plots are different between the plots.

The posterior values were also used to predict the expected densities at the different sampling areas during March and April at the mean distance from the field (Table 3.3). At this distance, the mean density, density at the median site, density at the 2.5 percentile site and at the 95.5 percentile site, were found using the following equations:

- Mean density: $\exp(\mu_{0,i} + x\beta + 0.5\sigma^2)$
- Density at median site: $\exp(\mu_{0,i} + x\beta)$
- Density at 2.5 percentile site: $\exp(\mu_{0,i} + x\beta - 1.96\sigma)$
- Density at 97.5 percentile site: $\exp(\mu_{0,i} + x\beta + 1.96\sigma)$

Table 3.3: Posterior summaries (2.5 % and 97.5 % quantiles in parentheses) of estimated densities of deer per km² at each of the sampling areas in March and April at a standardized distance from the field (approximately 162 m).

Sampling area	Month	Posterior mean of mean density	Posterior median of mean density	Posterior median of density at median site	Posterior median of density at 2.5 % site	Posterior median of density at 97.5 % site
Rå	March	5.6	2.4 (0.4, 29.2)	0.5 (0.1, 6.3)	$1.7 \cdot 10^{-2}$ ($2.4 \cdot 10^{-3}$, 0.3)	15.9 (2.4, 193.7)
Rå	April	7.4	3.1 (0.4, 38.0)	0.7 (0.1, 7.7)	$2.2 \cdot 10^{-2}$ ($2.6 \cdot 10^{-3}$, 0.3)	20.1 (2.5, 255.0)
Søre Bjørkum	March	35.7	32.5 (16.0, 74.3)	7.0 (3.6, 15.9)	0.2 (0.1, 1.0)	211.9 (98.8, 496.1)
Søre Bjørkum	April	17.1	13.7 (5.2, 48.7)	2.3 (1.5, 9.6)	0.1 ($2.7 \cdot 10^{-2}$, 0.5)	90.1 (31.5, 323.7)
Haugen	March	63.6	55.6 (24.9, 149.5)	12.0 (6.0, 30.0)	0.4 (0.1, 1.8)	362.6 (153.4, 998.3)
Haugen	April	120.0	99.3 (38.5, 324.1)	21.7 (9.3, 60.7)	0.7 (0.2, 3.2)	646.9 (236.5, 217.1)
Sprakehaug	March	13.5	10.3 (3.7, 41.7)	2.1 (1.1, 8.6)	0.1 ($2.0 \cdot 10^{-2}$, 0.4)	67.7 (22.4, 277.1)
Sprakehaug	April	4.5	2.0 (0.4, 24.0)	0.4 (0.1, 5.0)	$1.4 \cdot 10^{-2}$ ($2.4 \cdot 10^{-3}$, 0.2)	13.1 (2.3, 158.9)

The predicted median density of deer at the mean distance from the fields ranged from about 0.4 deer per km² (CRI: $1.4 \cdot 10^{-2}$ to 13.1 deer per km²) in Sprakehaug in April to 21.7 deer per km² (CRI: 0.7 to 646.9 deer per km²) in Haugen in April (Table 3.3). The predicted mean density of deer was much higher due to the high variance (Table 3.3).

Further, these results showed no clear effect of elevation on deer density between sampling areas. Both Rå, the sampling area located at the lowest elevation, and Sprakehaug, the sampling area at the highest elevation, had posterior mean densities in the region of 10.0 deer per km² and overlapping posterior 95 % CRI (Table 3.3; Figure 3.4). Month (March or April) did also appear to have no significant effect on density as mean densities were not

consistently higher for one month (Table 3.3; Figure 3.4). In addition, the 95 % CRI of the posterior mean densities of the sampling areas in March overlapped with the same sampling areas' 95 % CRI in April, e.g., the 95 % CRI of Sprakehaug in March overlapped with the 95 % CRI of Sprakehaug in April (Table 3.3; Figure 3.4).

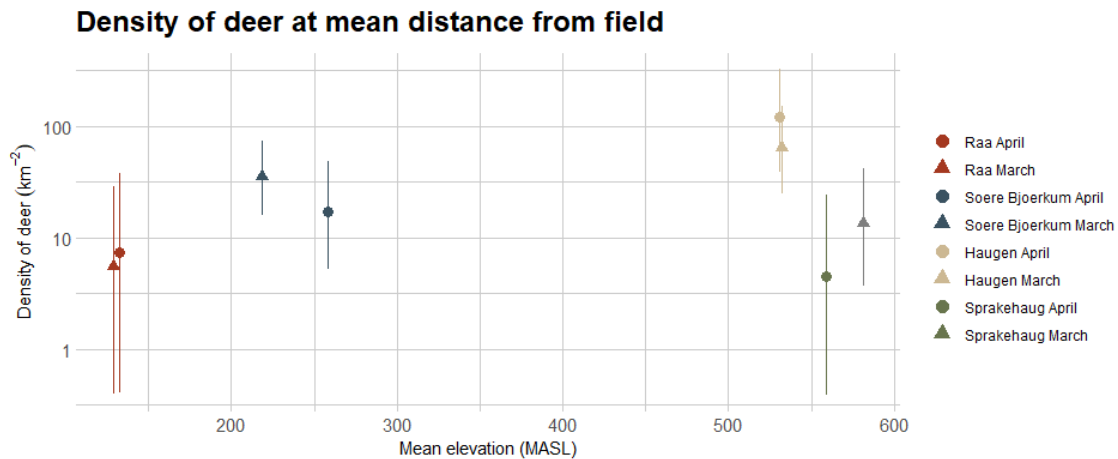


Figure 3.4: The estimated density of deer per km² at each of the sampling areas in March and April at a standardized distance from the field (approximately 162 m). The points represent the posterior mean density of red deer, and the lines represent the posterior lower and upper 95 % CRIs. The figure also shows the mean elevation of the sampling areas in March and April.

3.3 Behavioral response

From the deer's noted behavioral responses as seen in the images and from the observations made before and during flights, it became clear that captive red deer within the enclosure generally showed a lack of response to the unmanned aerial vehicle (UAV). A few animals closest to the stimulus became vigilant when take-off took place within these deer's line of sight, i.e., changed from foraging to alert posture with head and neck upright, ears erect and aimed at the UAV. However, shortly after take-off, most individuals lost interest and resumed back to foraging behavior. At 40 m AGL only a small minority of deer changed to an alert posture with head turned upwards towards the UAV as it overflowed the deer in question. At 60 m AGL no red deer were, seemingly, paying attention to the UAV. Contrariwise, the wild red deer showed much stronger sensitivity to the UAV. When the UAV was detected by wild deer during take-off, these deer immediately ran away from their original position in the opposite direction of the drone (during nighttime survey flights the take-off point was thus set as far away from the routes as possible). If the deer detected the observers before take-off, the deer

became vigilant but did not move as long as the observers kept quiet and calm. In these cases, the deer did not run until take-off was initiated, i.e., when rotor movement and noise began.

During the nighttime survey flights, which were all performed at 40 m AGL, the majority of deer were seen moving on the screen as the UAV overflew the animals. It is difficult to determine whether this movement was triggered by the UAV for several reasons. Firstly, the deer were moving in all directions, including towards the drone. Secondly, deer initially moving in the opposite direction of the drone did not seem to change direction as the drone turned around. Thirdly, most of the moving deer kept a walking pace or slower and may, therefore, have only been foraging. And, finally, the deer's body postures could not be identified (Figure 3.5). However, a small number of individuals could be seen running towards the forest, implying that the UAV was causing at least some disturbance to the animals. No deer were observed during the daytime survey flights performed at 40 m AGL.



Figure 3.5: Thermal image showing five red deer at a field in Haugen, Lærdal, Norway in April 2021. The deer's heat signature is obscured in the motionless image compared to in the live video observed during flight. The image was taken using the drone DJI Mavic 2 Enterprise Dual.

When the UAV was flown at 60 m AGL, during the daytime survey flights, the wild red deer were showing clear signs of a vigilant response to the stimulus. All deer whose head position could be identified in the images were at some point looking directly towards the drone with the ears pointed in the same direction (Figure 3.6). However, the deer's awareness of the UAV did not appear to cause the animals to move or speed up. Deer laying down or standing still remained in their position as the UAV passed above (Figure 3.6), while deer in movement did not seem to increase their pace. On the contrary, some of the deer in the latter category appeared to have a freeze response to the UAV for the brief moment these individuals were aiming their attention towards the stimulus. This response passed quickly,

and the effected individuals seemed to resume movement in the same direction as before the behavior change – regardless of the direction of the UAV.



Figure 3.6: Example images of red deer looking directly towards the direction of the UAV as it passes at 60 m AGL. Image A shows a hind standing still, while image B shows a stag on the move. Both images were captured in Haugen, Lærdal in March 2021. Image C shows a hind laying down in Sprakehaug, Lærdal in March 2021. Image D shows what appears to be a young stag laying down in Søre Bjørkum, Lærdal in April 2021. All images were taken using DJI Mavic 2 Enterprise Dual.

4 Discussion

Information about population estimates, such as density, is key to management and conservation of ecosystems (Collier et al., 2013; Graves et al., 2022; Lisein et al., 2013; Vermeulen et al., 2013; Corcoran et al., 2019; Spaan et al., 2019). The need for adequate population density data is especially crucial in the case of Norwegian red deer, where the Norwegian Environment Agency is aiming to protect the species from a potential chronic wasting disease (CWD) outbreak by reducing the density to less than one deer per km² (Miljødirektoratet, 2020; Solberg and Rolandsen, 2020). Yet, the density data needed to make informed decisions related to this goal is lacking, as the current data collection methods produce density estimates associated with unknown degrees of uncertainties (Solberg et al. 2019, p. 44). Thus, the aim of this thesis was to develop a method for providing more reliable population estimates of wild deer. By means of unmanned aerial vehicle (UAV) technology, the double-observer protocol, and hierarchical state space modeling (SSM) with Bayesian Markov chain Monte Carlo (MCMC) sampling, the study managed to produce red deer density estimates with reliable credible intervals (CRI) in four case studies at different sampling areas in Lærdal, Norway. The uncertainties of the estimates were large (wide CRI) but with more extensive surveys the developed method can be scaled up to produce more precise estimates. The results also suggests that, during the day, distance to the agricultural fields is a significant factor for red deer densities, with increased density further away from fields. Moreover, the UAV did not seem to trigger a flight response in the animals, i.e., the presence of the UAV likely did not influence deer density estimates, when flights took place 60 m above ground level (AGL).

4.1 Absolute red deer density estimates and CWD management

The background for this project was the lack of absolute population density estimates in connection to managing the risk of CWD spillover to red deer and moose. The “seen deer” or harvest statistics commonly used in Scandinavia mainly yield indexes for population development (Hjortevilt, n.d.; Solberg et al., 2019, pp. 10-13), which under normal management have proven sufficient to raise or lower harvest quotas. With the recommended CWD management goal being less than one deer per km², such data on population trends do no longer provide enough information to set adequate harvest quotas in the affected areas. However, the methods used in this study made it possible to obtain estimates of absolute densities at four different sampling areas during two different time periods. When looking at the estimated posterior mean density at a standardized distance from agricultural fields

(approximately 162 m), none of these sampling areas fulfilled the goal of less than one deer per km². The lowest densities were estimated in Sprakehaug in April, with a mean density of about 4.5 deer per km², and in Rå in both March and April, with respective mean densities of about 5.6 and 7.4 deer per km² (Table 3.3; Figure 3.2). The posterior mean density in Sprakehaug in March was slightly higher with about 13.5 deer per km². The estimated densities increased with the distance from agricultural fields, and vice versa. Yet, at 0 m from the fields, the posterior mean densities in Rå and Sprakehaug in April still never reached the goal. Although these were the areas with lowest estimated densities, the posterior mean densities ranged from approximately 3.0 deer per km² at the field boundary to 60.0 deer per km² at 500 m from the fields (Figure 3.2). The mean density of deer in Søre Bjørkum was between approximately 7.0 (0 m distance in April) and 200.0 (500 m distance in March; Figure 3.2). At the other end of the spectrum, and well above the recommended density, was Haugen with an estimated posterior mean of about 63.6 deer per km² in March and 120.0 deer per km² in April at the mean distance from agricultural fields (Table 3.3). Even at the field boundary (0 m), the estimated mean densities of red deer in Haugen never went below 50.0 deer per km² (Figure 3.2). At a 500 m distance from the fields, the estimated mean density of red deer in Haugen in April reached almost 1000.0 deer per km² (Figure 3.2).

A “rule-of-thumb” suggest red deer density generally is around 5 times the harvest (Solberg et al., 2019, p. 16). With a harvest density of 2.5 red deer per km², this would imply overall densities in Lærdal in the range of 10-15 red deer per km² at a broad scale. However, the data was collected on a relatively small scale in late winter and early spring, when red deer tend to have a more aggregated distribution (Bocci et al., 2010; Luccarini et al., 2006; Mysterud et al., 2021). Hence, the extreme estimates of local deer densities may be the result of surveys being conducted above “hot spots”, signifying that UAV surveys preferably should be conducted at broader scales. Such “hotspots” with temporary clustering of red deer may also have led to the vast differences in the deer densities estimated at the four sampling areas. Clearly, covering larger areas is likely to make results more reliable for informing management in this specific situation. That being said, biological factors are not the only possible explanation for the extreme estimates, as these may also be due to (or partially due to) lack of robustness in the statistical model. There was a large variation in the number of red deer counted at each site (Figure 3.2), implying that the data was not independent and, thus, a Poisson distribution perhaps not applicable. Furthermore, the large variance in the density of deer between sites (Figure 3.2) made the mean density estimates sensitive to the choice of

distribution when accounting for the variation in density. Here, I used a lognormal distribution with a heavy tail, which likely led to the large differences between the estimated median and mean densities and potentially the high mean density estimates (Table 3.3). Ideally, other distributions, e.g., different gamma distributions, should be explored. To determine which model best fits the data as well whether the data fits the model in an absolute sense, “goodness of fit” assessments for Bayesian models, that is, posterior predictive checks, should be completed.

The lower 95 % CRIs of Rå and Sprakehaug in April were either close to or below the recommendation (Figure 3.3), with approximately 0.4 deer per km² at the mean field distance (Table 3.3). Thus, there is a possibility that these areas already were within the goal of less than one deer per km². However, the 95 % CRI of the densities were rather wide, which also opens up the possibility that several of the sampling areas had densities close to or far away the Norwegian Environment Agency’s recommendations of less than one deer per km². For example, in Haugen in March, the area with one of the highest density estimates, the lower CRI at 0 m distance from agricultural fields was just a little above 5.0 deer per km² (Figure 3.3). While in Sprakehaug in March, the area with the lowest density estimates, the upper CRI at a 500 m distance from fields was close to 150.0 deer per km² (Figure 3.3). Nevertheless, the uncertainties of the estimates were indeed quantified, whereas a systematic review of deer density estimation documented that only 32% came with a measure of precision (Forsyth et al., 2022). And although this study’s estimated degrees of uncertainties were rather wide, clear differences in densities between sampling areas and months could be detected. E.g., at a standardized distance from the field, the posterior 95 % CRI of the density in Haugen in April did not overlap with that of Sprakehaug the same month (Table 3.3; Figure 3.3). Hence, even though the estimated densities preferably could have been more precise, the method used in this study showed great potential for reliable comparison of density estimates both in space and time.

Thus, if larger areas are covered, data obtained from UAV imagery will be more informative than current methods in determining whether deer densities are being reduced and are approaching the Norwegian Environment Agency’s recommendation of less than one deer per km² or whether they are increasing. The use of UAV data to make estimates about absolute densities with known precision will reduce the likelihood of grossly underestimating the harvest quotas needed to reach the target density, which also means reduced probability of spillover of CWD prions from environmental reservoirs to red deer or moose (Solberg et al.,

2019, p. 44; Ytrehus et al., 2018). Estimates about absolute densities with known precision will also reduce the likelihood of grossly overestimating the needed harvest quotas, effectively reducing the risk of overhunting. Although such a scenario arguably would be positive for the battle against CWD, and granted an unlikely scenario to begin with, overhunting would lead to longer recovery time for the populations and less animals available for hunting in the future (Solberg et al., 2019, p. 45).

4.2 Effect of variables on red deer density estimates

Animal densities and distributions are variable and dynamic from local to landscape scales, and results from processes involving daily foraging decisions to seasonal migrations and over years by population dynamics. Here, I focused on a relatively small, local area during only two successive months in the late winter/early spring of one season. Despite the small scale of the study, estimated densities varied greatly between the sampling sites. As mentioned above, this may have been caused by the increased aggregation of red deer during winter (Bocci et al., 2010; Luccarini et al., 2006; Mysterud et al., 2021). In addition, deer tend to stay on open fields during darkness and move to forest covers at dawn (Armstrong, Euler and Racey, 1983; Beier and McCullough, 1990; Godvik et al., 2009). This distribution of red deer on a daily scale might also help explain some of the great variation in the results. The daytime survey flights of the sampling area with the highest estimated densities, Haugen, were solely performed in the “morning” hours, from 07:53 to 09:45 (see Appendix C for time of all flights). At this time, red deer foraging in the fields might just recently have moved into the forest covers. Hence, these deer would have had relatively little time to move beyond the sampling routes since these were rather close to the fields (see Appendix A for map of route perimeters).

Further, the estimated red deer densities did not significantly differ between different elevations or months. That may be true in the “snapshot” moment represented in the study. In reality, migratory red deer move between low elevations with less snow in the winter and high elevations with less competition during breeding in the summer (Luccarini et al., 2006; Mysterud et al., 2011; 2021). The migration from winter to summer range happens rapidly, in one or a few abrupt moves (Bischof et al., 2012), and so it is likely that no such movements had taken place between the two sampling periods in March and April.

The resulting conclusion that red deer densities at daytime increase with increased distance from agricultural fields, as opposed to with increased distance from the forest

boundaries, is, however, reasonable with respect to prior knowledge. Red deer tend to select home ranges with two main components: refuge or safety for daylight hours, such as forest covers, and quality forage for the night, such as agricultural fields (Coppes et al., 2017; Fattebert et al., 2019; Godvik et al., 2009; Langvatn and Hanley, 1993). In that regard, both the agricultural field boundaries and the forest boundaries are arguably of great importance to local red deer densities. However, within the home range, red deer have repeatedly been found to avoid areas with human recreation/disturbance, in particular during daylight hours (Coppes et al., 2017). This includes roads (Meisingset et al., 2013), hiking trails (Sibbald et al., 2011; Westekemper et al., 2018), and mountain biking trails (Scholten, Moe and Hegland, 2018). Forest boundaries are oftentimes relatively far up the mountain slope (Figure 4.1), i.e., away from human activities, and agricultural fields entail repeated human presence. It is therefore plausible that the density of deer is more affected by the distance to the agricultural fields and not the distance to the end of the forest cover. The optimal distance from the fields, i.e., the distance with maximum estimated density, could potentially have been assessed using a quadratic function to find the vertex. With the small-scale data of this study, such an approach may result in even less precise estimates.



Figure 4.1: Example map showing line strings with the agricultural field and forest boundaries at Sprakehaug, Lærdal, Norway (Google Earth V 7.3.3, 2020e). The red line represents the field boundary, and the white line represents the forest boundary. Top side of map is north.

4.3 Effects of UAV on red deer behavior

Although UAVs are increasingly used as a tool to observe and monitor wildlife (Hodgson et al., 2018; Schroeder et al., 2020), relatively little research has been completed on the impact UAVs have on different species. The presence of a UAV may be disturbing and stress-inducing, in the worst cases harmful, to both target and non-target animals in the area. This is especially a concern for species subjected to avian predation (Christie et al., 2016).

Furthermore, if the target animals take flight, the data obtained via UAV may be difficult to use for other purposes than detection, as the animals may leave the survey area completely or the same individuals may be present in several different frames. Thus, it is preferable to have some knowledge about the species response to UAVs before take-off. In this study, it quickly became clear that wild red deer are quite sensitive to UAVs at ground level, with nearby deer taking flight as soon as the rotor started to move. The lack of such a response before take-off was initiated indicated that the locomotion was triggered by the sound of the UAV, rather than visual stimuli, i.e., the deer were fairly sensitive to the auditory stimuli. This postulation was further supported by the observation of deer running towards the forest during the nighttime survey flights at 40 m AGL. It was quite arduous to keep sight of the UAV in the dark (with the exception of a small green/red light at the topside of the drone, it was essentially invisible), making it unlikely that the deer had made a visual observation.

At 60 m AGL during daytime, the wild red deer were undoubtedly disrupted by the UAV, as evidenced by the deer's head posture and gaze (Figure 3.6), and the momentary "freeze response". This latter response was arguably an advantage for the data collection method since the deer remained in the area and within one frame (i.e., no false positives). The tame deer, that generally were less triggered by the UAV, never showed such an obvious response; however, these animals paid more attention to the UAV when it was 40 m AGL than when it was 60 m AGL. Hence, considering their response to the drone at 60 m AGL during the day and 40 m AGL during the night, the wild deer were probably quite disturbed when the UAV overflew at only 40 m AGL during the day. At this height, the deer could probably both see and hear the UAV very well during the day, which likely triggered a fleeing response in a larger share than observed at night. The lack of detected deer in Rå at 40 m AGL during the daytime may thus be explained by the deer fleeing the area as a response to the UAV.

Witczuk et al. (2018) did not report on the red deer's response to the UAV. All flights were performed at around 150 m AGL in that study, thus the response, if any, was likely to be

significantly weaker than what was observed here. Studies on other species' responses to UAVs are limited and the results are varied. Wild boars (*Sus scrofa*) reportedly showed no marked reaction or distracted movements when an UAV was flown 50 m from the animals (Iwamoto et al., 2022). While guanacos (*Lama guanicoe*), on the contrary, were highly sensitive to UAVs, with almost half of an analyzed group reacting to the drone at 180 m AGL – a distance at which the animals were likely to only hear the UAV (Schroeder et al., 2020). A review of existing literature on animals' responses to UAVs reported that the reactions depend on characteristics of both the UAVs and of the animals themselves (Mulero-Pázmány et al., 2017). However, target-oriented flight patterns, larger UAVs, and noisier engines generally evoked stronger reactions in all investigated species (Mulero-Pázmány et al., 2017). Furthermore, a study quantifying the distances at which different species could make auditory detections of UAVs found that white-tailed deer are able to hear particular drones flying at almost 700 m AGL during certain weather conditions (Scobie and Hugenholtz, 2016). Thus, the increased noise alone, which the red deer probably could pick up with ease, likely made the deer more sensitive to the UAV at 40 m AGL than at 60 m AGL. And although the response at 40 m AGL could not be sufficiently observed, reducing the altitude to less than 60 m AGL has proven pivotal in generating behavioral responses in several other herbivore species, including ungulates such as wildebeests (*Connochaetes taurinus*; Bennitt et al., 2019). Moreover, even if the red deer did not flee, as observed when the UAV was flown 60 m AGL, the animals may still have experienced a strong physiological response. A study on free-roaming American black bears (*Ursus americanus*) found that the bears responded to UAV flights with elevated heart rates despite infrequent behavioral changes (Ditmer et al., 2015). A follow-up study on captive bears showed that the bears were capable of habituating to the UAV after 3-4 weeks of repeated exposure (Ditmer et al., 2019). However, such regular exposure is arguably not realistic in the case of wild deer. With all this in mind, I strongly recommend to not fly the UAV any lower than 60 m AGL when surveying areas with red deer. Most importantly to avoid stressing or causing harm to the animals and to prevent temporal abandonment of the area (which can lead to energetic costs and possibly reduced fitness; Coppes et al., 2017), but also in order to obtain the best data possible.

4.4 Limitations and advantages of UAV for density estimates

A frequently reported challenge when using UAVs for data collection is the restrictions imposed by keeping the drone within visual line of sight (Preston et al., 2021; Spaan et al., 2019), which is now required by law in many countries. Although an initial concern, this soon

turned out to be of little importance in this specific study, as the flights first and foremost were limited by the steep and rugged terrain of the mountain slopes. Here, the main challenge was avoiding trees, cliffs, crevasses, and knolls to prevent the UAV from crashing (Figure 4.2). As reported in another UAV study, high voltage power lines also restricted the flights of the UAV (Iwamoto et al., 2022). Further, Hodgson et al. (2016) have previously mentioned comparison of UAV derived estimates to data from traditional methods as a potential challenge. As no data could be obtained on the length or area covered by the current data collection methods in Lærdal, it was indeed difficult to make sensible comparisons of the estimates from this study to estimates from harvest statistics or spring counts. Thus, no such comparisons were made. That being said, it should be possible to secure approximate lengths of the road-based spring count routes (Lars Nesse, 2022, pers. comm. 8 August) and the potential for comparison should be investigated in the future.



Figure 4.2: The last images taken by the UAV before/during collision with trees. Image A shows a collision in Sprakehaug, Lærdal, in which the UAV had no damages and managed to fly back to take-off point. Image B shows a collision in Søre Bjørkum, Lærdal, in which the UAV was retrieved from the ground the following day. The images were captured in April and March 2021 with the drone DJI Mavic 2 Enterprise Dual.

Another main challenge of the method is the high dependence on weather conditions (Witczuk et al., 2018). This was a significant limitation here as well, and a large number of flights had to be cancelled due to precipitation and/or strong winds. That being said, I recommend that future UAV surveys are completed in the winter as detection will be almost impossible with leaf canopy in summer (Figure 4.3). In addition, in the winter it may be possible to distinguish between a larger number of hinds and stags as all stags are expected to have antlers. Surveying snow covered surfaces will also make detection easier due to higher contrast, visible tracks, and the potential to use thermal camera as support. Without snow, the thermal camera was limited by signals from heated landscape elements – even at night. The

spectral confusion brought on by such objects is a common issue when using UAVs with thermal cameras (Seymour et al., 2017; Kays et al., 2019; Spaan et al., 2019; Takehiko et al., 2022). Another previously reported issue experienced in this study, was the failure to align the images (Preston et al., 2021). As an orthomosaics could not be produced from the images of this study, I recommend setting the sidelap to 0 % so that larger areas can be surveyed in the same amount of flight time, i.e, same amount of battery usage. Forelap, on the other hand, is still needed to detect deer underneath trees, but this does not deduct from the total flight time. Other studies using UAVs as a data collection tool for estimation of animal population parameters, have also mentioned issues such as duplicate detections (Chrétien, Théau and Ménard, 2016; Preston et al., 2021), difficulties in species identification (Witczuk et al., 2018), and flight endurance (Lichante et al., 2015). Of these, only flight endurance was a relevant drawback in this study. However, this, and several of the aforementioned challenges, can be overcome by development of better technology and the use of UAV for data collection of wildlife is still promising.

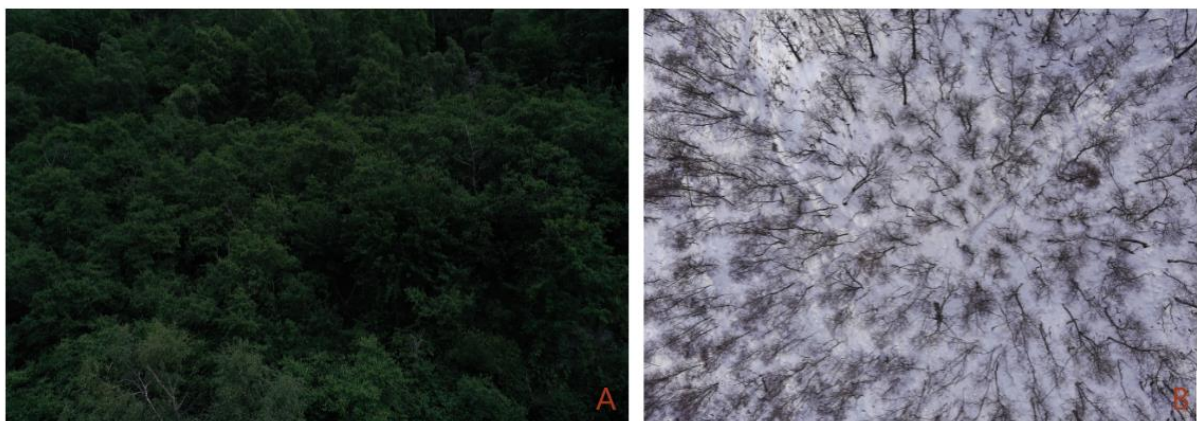


Figure 4.3: Forest canopy in late summer vs. in late winter. Image A was taken with DJI Mavic 2 Pro in Borgund, Lærdal, Norway in September 2020. Image B was taken with DJI Mavic 2 Enterprise Dual in Haugen, Lærdal, Norway in March 2021.

The promising results of UAV within wildlife ecology can be credited to the aircraft's ability to collect quality data from more than one sensor, e.g., from daytime red-green-blue (RGB) and thermal cameras (Hodgson et al., 2018; Lyons et al., 2019; Schroeder et al., 2020). Furthermore, unlike traditional ground-based methods, UAV surveys produce a permanent record that can be analyzed multiple times and by numerous observers, making it possible to complete counts over more than one setting (minimizing observer fatigue), error-check, and recount with different detection methods (Terletzky, Ramsey and Neale, 2012; Christie et al., 2016; Hodgson et al., 2016; 2018; Schroeder et al., 2020; Preston et al., 2021). No reports

could be found on the detection probabilities of the methods currently used to estimate red deer densities in Norway (harvest statistics and on-road spotlight surveys). However, compared to the detection probabilities obtained from spotlight surveys of white-tailed deer, the results from the UAV data were promising: While the mean detection probabilities for spotlight observers ranged from 30-66 % (Collier et al., 2013), the posterior mean detection probabilities for the UAV imagery observers ranged from about 73 % to 84 %, with the lowest CRI being approximately 63 % (Table 3.2). In addition, the permanent record created by UAVs makes it possible to provide optimal information on the survey area's characteristics (Preston et al., 2021).

The use of camera traps is another relatively new method for collecting population data that also can produce a permanent record, and advances in camera trapping technologies and studies are expected to provide new opportunities for wildlife ecology (Delisle et al., 2021; Palencia et al., 2021). However, at present time there are several disadvantages to camera traps. For example, the cameras often require significant amounts of power to continuously operate (Swann, Kawanishi and Palmer, 2011). A potential solution to this problem is the use of triggered cameras, however, such cameras may falsely trigger, or environmental conditions/ operating errors may cause the sensors to fail and not trigger at all (Swann, Kawanishi and Palmer, 2011). Furthermore, triggered traps contain several parts and if one part fails, for instance due to animals chewing or pulling on the cords (Sequin et al., 2003), the whole system may fail (Swann, Kawanishi and Palmer, 2011). Another concern is the animals' reactions to camera traps, not only from an animal welfare perspective but also because reactions may lead to biased results (Henrich et al., 2020; Swann, Kawanishi and Palmer, 2011; Wegge, Pokheral and Jnawali, 2004). Red deer have been found particularly sensitive to camera traps – many taking flight as a response to the camera flash, with some fleeing even without the flash (Henrich et al., 2020). In contrast to camera traps and traditional methods, UAVs can collect data without entering ecologically sensitive areas, significantly reducing disturbance (Lichant et al., 2015; Hodgson et al., 2018). UAV data can also be collected from areas that are inaccessible or hard-to-reach using ground surveys (Christie et al., 2016; Hodgson et al., 2016; 2018; Kellenberger, Marcos and Tuia, 2018) – potentially avoiding the analytical errors associated with road counts (Preston et al., 2021). These advantages can also be found in sampling methods using manned aircrafts. However, compared to such methods, UAV surveys are less costly, significantly safer, less noisy, logistically convenient (e.g., no prepared runway is needed, flying below cloud covers is

possible), and the UAVs' ecological footprint is much smaller (Vermeulen et al., 2013; Lichant et al., 2015; Hodgson et al., 2018; Witzuk et al., 2018; Beaver et al., 2020; Schroeder et al., 2020; Preston et al., 2021).

5 Concluding remarks and future recommendations

On the whole, unmanned aerial vehicles (UAVs) have the potential to become a powerful tool for wildlife ecology, in particular within population estimation. The accuracy and precision of the absolute deer density estimates from the UAV data are likely to be increased if larger areas are covered by the surveys. In addition to flying with no sidelap, this may be possible with better equipment, including UAVs with longer battery life, better obstacle sensors to decrease collision-potential in steep areas, and/or with better cameras that can capture detailed images even further above ground. However, in such a scenario, the legal requirement of maintaining visual line of sight with the UAV may pose a greater challenge. In addition, surveying of larger areas will in effect mean surveying of more images, and manual analysis of images will as a consequence become substantially more time consuming, labor intensive, and possibly costly (Corcoran et al., 2019; Hodgson et al., 2018). An increasingly employed solution to this latter obstacle is the use of machine learning techniques to identify wildlife in UAV imagery (Corcoran et al., 2021, Hodgson et al., 2018; Schroeder et al., 2020). E.g., semi-automated and automated detection systems have successfully been used to count grey seals (*Halichoerus grypus*; Seymore et al., 2017) and fake seabirds (Hodgson et al., 2018), as well as to detect koalas (*Phascolarctus cinereus*; Corcoran et al., 2019) and white-tailed deer (Chrétien, Théau and Ménard, 2016). Results from such studies have found that machine learning techniques can reduce bias and increase precision and accuracy compared to manual analysis (Corcoran et al., 2019). The most prominent automated detection method, the use of convolutional neural networks (CNNs), can detect target animals in complex vegetation despite inconsistencies in the target animals' size, shape, and color (Corcoran et al., 2021; Eikelboom et al., 2019), and is arguably therefore well suited for detection of Norwegian red deer. By replacing manual counts with this technique, as well as increasing the sample size, UAV data might in the near future be used to make precise and accurate estimates of absolute deer densities in Nordafjella Zone 1 and other areas bordering this chronic wasting disease (CWD) contaminated area. Improved estimation of deer densities may also be useful for a number of other management issues in Norway and elsewhere.

References

- AgiSoft Metashape Professional version 1.7.5 (10 October 2021). Available from: <https://www.agisoft.com/downloads/installer/>
- Armstrong, E., D. Euler and G. Racey (1983) White-tailed deer habitat and cottage development in central Ontario. *The Journal of Wildlife Management*, 47 (3), pp. 605-612. Available from: <https://doi-org.ezproxy.uio.no/10.2307/3808598>.
- Beaver, J. T., R. W. Baldwin, M. Messinger, C. H. Newbolt and S. S. Ditchkoff (2020) Evaluating the use of drones equipped with thermal sensors as an effective method for estimating wildlife. *Wildlife Society Bulletin*, 44 (2), pp. 434-443. Available from doi:10.1002/wsb.1090.
- Beier P. and D. R. McCullough (1990) Factors influencing white-tailed deer activity patterns and habitat use. *Wildlife Monographs*, 109, pp. 3-51. Available from: <https://www.jstor.org/stable/3830629>.
- Benestad, S. L., G. Mitchell, M. Simmons, B. Ytrehus and T. Vikøren (2016) First case of chronic wasting disease in Europe in a Norwegian free-ranging reindeer. *Veterinary Research*, 47 (88). Available from doi:10.1186/s13567-016-0375-4.
- Bennitt, E., H. L. A. Bartlam-Brooks, T. Y. Hubel and A. M. Wilson (2019) Terrestrial mammalian wildlife responses to Unmanned Aerial Systems approaches. *Scientific Reports*, 9 (1), 2142. Available from: <https://doi.org/10.1038/s41598-019-38610-x>.
- Bischof, R., L. E. Loe, E. L. Meisingset, B. Zimmermann, B. Van Moorter and A. Mysterud (2012) A migratory northern ungulate in the pursuit of spring: jumping or surfing the green wave?. *The American naturalist*, 180 (4), pp. 407-424. Available from: <https://doi.org/10.1086/667590>.
- Bocci, A., A. Monaco, P. Brambilla, I. Angelini and S. Lovari (2010) Alternative strategies of space use of female red deer in a mountainous habitat. *Annales Zoologici Fennici*, 47 (1), pp. 57-66. Available from: <http://www.jstor.org/stable/23737037>.
- Brack, I.V., A. Kindel and L. F. B. Oliveira (2018) Detection errors in wildlife abundance estimates from Unmanned Aerial Systems (UAS) surveys: Synthesis, solutions, and challenges. *Methods in Ecology and Evolution*, 9 (8), pp. 1864-1873. Available from: <https://doi.org/10.1111/2041-210X.13026>.
- Brooks, M. E., K. Kristensen, K. J. van Benthem, A. Magnusson, C. W. Berg, A. Nielsen, H. J. Skaug, M. Maechler and B. M. Bolker (2017) glmmTMB balances speed and flexibility among packages for zero-inflated generalized linear mixed modeling. *The R Journal*, 9 (2), pp. 378-400. Available from: <https://journal.r-project.org/archive/2017/RJ-2017-066/index.html>.
- Chrétien, L.-P., J. Théau and P. Ménard (2016) Visible and thermal infrared remote sensing for the detection of white-tailed deer using an unmanned aerial system. *Wildlife Society Bulletin*, 40 (1), pp. 181-191. Available from doi:10.1002/wsb.629.

- Christie, K. S., S. L. Gilbert, C. L. Brown, M. Hatfield and L. Hanson (2016) Unmanned aircraft systems in wildlife research: current and future applications of a transformative technology. *Frontiers in Ecology and Environment*, 14 (5), pp. 241-251. Available from doi:10.1002/fee.1281.
- Chronic Wasting Disease Alliance (2020) *Chronic Wasting Disease FAQ*. Available from: [http://cwd-info.org/faq/#:~:text=Chronic%20Wasting%20Disease%20\(CWD\)%20is,of%20bodily%20functions%20and%20death](http://cwd-info.org/faq/#:~:text=Chronic%20Wasting%20Disease%20(CWD)%20is,of%20bodily%20functions%20and%20death). [Accessed 15 August 2020].
- Collier, B. A., S. S. Ditchkoff, C. R. Ruth and J. B. Raglin (2013) Spotlight surveys for white-tailed deer: Monitoring panacea or exercise in futility?. *The Journal of Wildlife Management*, 77 (1), pp. 165-171. Available from doi:10.1002/jwmg.444.
- Coppes, J., F. Burghardt, R. Hagen, R. Suchant and V. Braunisch (2017) Human recreation affects spatio-temporal habitat use patterns in red deer (*Cervus elaphus*). *PLoS ONE*, 12 (5), e0175134. Available from: <https://doi.org/10.1371/journal.pone.0175134>.
- Corcoran, E., M. Winsen, A. Sudholz and G. Hamilton (2021) Automated detection of wildlife using drones: Synthesis, opportunities and constraints. *Methods in Ecology and Evolution*, 12 (6), pp. 1103-1114. Available from doi:10.1111/2041-210X.13581.
- Corcoran, E., S. Denman, J. Hanger, B. Wilson and G. Hamilton (2019) Automated detection of koalas using low-level aerial surveillance and machine learning. *Scientific Reports*, 9 (1), 3208. Available from: <https://doi.org/10.1038/s41598-019-39917-5>.
- Delisle, Z. J., E. A. Flaherty, M. R. Nobbe, C. M. Wzientek and R. K. Swihart (2021) Next-generation camera trapping: Systematic review of historic trends suggests keys to expanded research applications in ecology and conservation. *Frontiers in Ecology and Evolution*, 9. Available from doi:10.3389/fevo.2021.617996.
- de Valpine P., C. Paciorek, D. Turek, N. Michaud, C. Anderson-Bergman, F. Obermeyer, C. Wehrhahn Cortes, A. Rodriguez, D. Temple Lang and S. Paganin (2022). *NIMBLE: MCMC, particle filtering, and programmable hierarchical modeling*. R package version 0.12.2. Available from doi: 10.5281/zenodo.1211190 and <https://cran.r-project.org/package=nimble>.
- de Valpine P., D. Turek, C. Paciorek, C. Anderson-Bergman, D. Temple Lang and R. Bodik (2017) Programming with models: writing statistical algorithms for general model structures with NIMBLE. *Journal of Computational and Graphical Statistics*, 26, pp. 403-413. Available from doi:10.1080/10618600.2016.1172487.
- Ditmer, M. A., J. B. Vincent, L. K. Werden, J. C. Tanner, T. G. Laske, P. A. Iaizzo, D. L. Garshelis and J. R. Fieberg (2015) Bears show a physiological but limited behavioral response to unmanned aerial vehicles. *Current Biology*, 25 (17), pp. 2278-2283. Available from: <https://doi.org/10.1016/j.cub.2015.07.024>.
- Ditmer, M. A., L. K. Werden, J. C. Tanner, J. B. Vincent, P. Callahan, P. A. Iaizzo, T. G. Laske, and D. L. Garshelis (2019) Bears habituate to the repeated exposure of a novel

- stimulus, unmanned aircraft systems. *Conservation Physiology*, 7 (1), coy067. Available from: <https://doi.org/10.1093/conphys/coy067>.
- Drones Made Easy (2022) *Arbitrary DEM preparation for use as a custom terrain source*. Available from: <https://support.dronesmadeeasy.com/hc/en-us/articles/360021867012-Arbitrary-DEM-Preparation-for-use-as-a-Custom-Terrain-Source> [Accessed 5 April 2022].
- Eikelboom, J. A. J., J. Wind, E. van de Ven, L. M. Kenana, B. Schroder, H. J. de Knegt, F. van Langevelde and H. H. T. Prins (2019) Improving the precision and accuracy of animal population estimates with aerial image object detection. *Methods in Ecology and Evolution*, 10 (11), pp. 1875-1887. Available from doi:10.1111/2041-210X.13277.
- EROS (Earth Resources Observation and Science) Center (2018) *USGS EROS Archive - Digital Elevation - Shuttle Radar Topography Mission (SRTM) 1 Arc-Second Global*. Available from: <https://www.usgs.gov/centers/eros/science/usgs-eros-archive-digital-elevation-shuttle-radar-topography-mission-srtm-1> [Accessed 5 April 2022].
- Escobar, L. E., S. Pritzkow, S. N. Winter, D. A. Grear, M. S. Kirchgessner, E. Dominguez-Villegas, G. Machado, A. T. Peterson and C. Soto (2020) The ecology of chronic wasting disease in wildlife. *Biological Reviews*, 95 (2), pp. 393-408. Available from doi:10.1111/brv.12568.
- Fattebert, J., K. Morelle, J. Jurkiewicz, J. Ukalska and J. Borkowski (2019). Safety first: seasonal and diel habitat selection patterns by red deer in a contrasted landscape. *Journal of Zoology*, 308 (2), pp. 111-120. Available from doi: 10.1111/jzo.12657.
- Forsyth, D. M., S. Comte, N. E. Davis, A. J. Bengsen, S. D. Côté, D. G. Hewitt, N. Morellet and A. Mysterud (2022) Methodology matters when estimating deer abundance: a global systematic review and recommendations for improvements. *Journal of Wildlife Management*, 86 (4), e22207. Available from doi:10.1002/jwmg.22207.
- Gelman, A., J. B. Carlin, H. S. Stern and D. B. Rubin (2004) *Bayesian Data Analysis*. 2nd edn., Boca Raton; London; New York; Washington DC, Chapman & Hall/CRC.
- Godvik, I. M. R., L. E. Loe, J. O. Vik, V. Veiberg, R. Langvatn and A. Mysterud (2009) Temporal scales, trade-offs, and functional responses in red deer habitat selection. *Ecology*, 90 (3), pp. 699-710. Available from: <https://doi-org.ezproxy.uio.no/10.1890/08-0576.1>.
- Google Earth V 7.3.3 (20 April 2020a) Haugen, Lærdal, Norway. 61° 04'44"N, 7°53'17"E, Camera 2,508 km. CNS/Airbus 2019. Available from: <http://www.earth.google.com>. [Accessed 20 April 2022].
- Google Earth V 7.3.3 (20 April 2020b) Søre Bjørkum, Lærdal, Norway. 61° 03'11"N, 7°40'23"E, Camera 2,231 km. CNS/Airbus 2019. Available from: <http://www.earth.google.com>. [Accessed 4 April 2022].

- Google Earth V 7.3.3 (20 April 2020c) Rå, Lærdal, Norway. 61° 02'06"N, 7°38'03"E, Camera 2,118 km. CNS/Airbus 2019. Available from: <http://www.earth.google.com>. [Accessed 4 April 2022].
- Google Earth V 7.3.3 (20 April 2020d) Haugen, Lærdal, Norway. 61° 04'46"N, 7°53'15"E, Camera 2,578 km. CNS/Airbus 2019. Available from: <http://www.earth.google.com>. [Accessed 4 April 2022].
- Google Earth V 7.3.3 (20 April 2020e) Sprakehaug, Lærdal, Norway. 61° 05'37"N, 7°52'46"E, Camera 2,616 km. CNS/Airbus 2019. Available from: <http://www.earth.google.com>. [Accessed 4 April 2022].
- Graves, T. A., M. J. Yarnall, A. N. Johnston, T. M. Preston, G. W. Chong, E. K. Cole, W. M. Janousek and P. C. Cross (2022) Eyes on the herd: Quantifying ungulate density from satellite, unmanned aerial systems, and GPS collar data. *Ecological Applications*, (e2600). Available from: <https://doi.org/10.1002/eap.2600>.
- Henrich, M., S. Niederlechner, M. Kröschel, S. Thoma, C. F. Dormann, F. Hartig and M. Heurich (2020) The influence of camera trap flash type on the behavioural reactions and trapping rates of red deer and roe deer. *Remote Sensing in Ecology and Conservation*, 6 (3), pp. 399-410. Available from: <https://doi-org.ezproxy.uio.no/10.1002/rse2.150>.
- Hijmans, R. J. and J. van Etten (2012) *Raster: Geographic analysis and modeling with raster data*. R package version 2.0-12. Available from: <http://CRAN.R-project.org/package=raster>
- Hjortevilt (n.d.) *Fakta om hjort [Facts about red deer]*. [Internet]. Available from: <https://www.hjortevilt.no/fakta-om-artene/hjort/> [Accessed 13 February 2022].
- Hjortevilt (n.d.) *Sett elg og sett hjort [Seen moose and seen red deer]*. [Internet] Available from: <https://www.hjortevilt.no/sett-elg-og-sett-hjort-2/> [Accessed 10 August 2022].
- Hodgson, J. C., R. Mott, S. M. Baylis, T. T. Pham, S. Wotherspoon, A. D. Kilpatrick, R. R. Segaran, I. Reid, A. Terauds and L. P. Koh (2018) Drones count wildlife more accurately and precisely than humans. *Methods in Ecology and Evolution*, 9 (5), pp. 1160-1167. Available from doi:10.1111/2041-210X.12974.
- Hodgson, J. C., S. M. Baylis, R. Mott, A. Herrod and R. H. Clarke (2016) Precision wildlife monitoring using unmanned aerial vehicles. *Scientific Reports*, 6, 22574. Available from doi:10.1038/srep22574.
- Iwamoto, M., S. Nogami, T. Ichinose and K. Takeda (2022) Unmanned aerial vehicles as a useful tool for investigating animal movements. *Methods in Ecology and Evolution*, 13 (5), pp. 969-975. Available from: <https://doi-org.ezproxy.uio.no/10.1111/2041-210X.13829>.
- Kays, R., J. Sheppard, K. Mclean, C. Welch, C. Paunescu, V. Wang, G. Kravit and M. Crofoot (2019) Hot monkey, cold reality: surveying rainforest canopy mammals using

- drone-mounted thermal infrared sensors. *International Journal of Remote Sensing*, 40 (2), pp. 407-419. Available from: <https://doi.org/10.1080/01431161.2018.1523580>.
- Kellenberger, B., D. Marcos and D. Tuia (2018) Detecting mammals in UAV images: Best practices to address a substantially imbalanced dataset with deep learning. *Remote Sensing of Environment*, 216 (October 2018), pp. 139-153. Available from: <https://doi.org/10.1016/j.rse.2018.06.028>.
- Kéry, M. and J. A. Royle (2016) *Applied hierarchical modeling in ecology: Analysis of distribution, abundance and species richness in R and BUGS*. Amsterdam; Boston, Academic Press.
- Kéry, M. and M. Schaub (2011) *Bayesian population analysis using WinBUGS: A hierarchical perspective*. Academic Press.
- Lande, U. S., L. E. Loe, O. J. Skjærli, E. L. Meisingset and A. Mysterud (2014) The effect of agricultural land use practice on habitat selection of red deer. *European Journal of Wildlife Research*, 60, pp. 69-76. Available from doi:10.1007/s10344-013-0751-6.
- Langvatn, R. and T. A. Hanley (1993) Feeding-patch choice by red deer in relation to foraging efficiency: An experiment. *Oecologia*, 95 (2), pp. 164-170. Available from: <https://doi.org/10.1007/BF00323486>
- Linchant, J., J. Lisein, P. Lejeune and C. Vermeulen (2015) Are unmanned aircraft systems (UASs) the future of wildlife monitoring? A review of accomplishments and challenges. *Mammal Review*, 45 (4), pp. 239-252. Available from: <https://doi.org/10.1111/mam.12046>.
- Lisein, J., J. Linchant, P. Lejeune, P. Bouché and C. Vermeulen (2013) Aerial surveys using an Unmanned Aerial System (UAS): comparison of different methods for estimating the surface area of sampling strips. *Tropical Conservation Science*, 6 (4), pp. 506-520. Available from doi:10.1177/194008291300600405.
- Luccarini, S., L. Mauri, S. Ciuti, P. Lamberti and M. Apollonio (2006) Red deer (*Cervus elaphus*) spatial use in the Italian Alps: home range patterns, seasonal migrations, and effects of snow and winter feeding. *Ethology Ecology & Evolution*, 18, pp. 127-145. Available from doi: 10.1080/08927014.2006.9522718.
- Lyons, M. B., K. J. Brandis, N. J. Murray, J. H. Wilshire, J. A. McCann, R. T. Kingsford and C. T. Callaghan (2019) Monitoring large and complex wildlife aggregations with drones. *Methods in Ecology and Evolution*, 10 (7), pp. 1024-1035. Available from: <https://doi.org/10.1111/2041-210X.13194>.
- Meisingset, E. L., L. E. Loe, Ø. Brekkum, B. Van Moorter and A. Mysterud (2013), Red deer habitat selection and movements in relation to roads. *The Journal of Wildlife Management*, 77 (1), pp. 181-191. Available from: <https://doi-org.ezproxy.uio.no/10.1002/jwmg.469>.

- Microsoft (2017) *Paint 3D* (Version 6.2105.4017.0) [Computer Program]. Available from: <https://apps.microsoft.com/store/detail/paint-3d/9NBLGGH5FV99?hl=en-us&gl=US>
- Miljødirektoratet (2020) Bestandsreduksjon av elg og hjort i Nordfjella – videre arbeid i jaktsesongen 2020/2021. [Letter]
- Miller, M. W. and E. S. Williams (2003) Horizontal prion transmission in mule deer. *Nature*, 425 (6953), pp. 35-36. Available from: <http://dx.doi.org/10.1038/425035a>.
- Miller, M. W., E. S. Williams, N. T. Hobbs and L. L. Wolfe (2004) Environmental sources of prion transmission in mule deer. *Emerging Infectious Diseases*, 10 (6), pp. 1003-1006. Available from doi:10.3201/eid1006.040010.
- Mulero-Pázmány, M., S. Jenni-Eiermann, N. Strebel, T. Sattler, J. J. Negro and Z. Tablado (2017) Unmanned aircraft systems as a new source of disturbance for wildlife: A systematic review. *PLoS ONE*, 12 (6), e0178448. Available from: <https://doi.org/10.1371/journal.pone.0178448>.
- Mysterud, A. and C. M. Rolandsen (2018) A reindeer cull to prevent chronic wasting disease in Europe. *Nature Ecology and Evolution*, 2 (9), pp. 1343-1345. Available from doi:10.1038/s41559-018-0616-1.
- Mysterud, A. and D. R. Edmunds (2019) A review of chronic wasting disease in North America with implications for Europe. *European Journal of Wildlife Research*, 65 (26). Available from: <https://doi.org/10.1007/s10344-019-1260-z>. [Accessed 7 May 2022].
- Mysterud, A., E. L. Meisingset, V. Veiberg, R. Langvatn, E. J. Solberg, E.J., L. E. Loe and N. C. Stenseth (2007) Monitoring population size of red deer: an evaluation of two types of census data from Norway. *Wildlife Biology*, 13 (3), pp. 285-298. Available from: [https://doi.org/10.2981/0909-6396\(2007\)13\[285:MPSORD\]2.0.CO;2](https://doi.org/10.2981/0909-6396(2007)13[285:MPSORD]2.0.CO;2).
- Mysterud, A., I. N. Skjelbostad, I. M. Rivrud, Ø. Brekkum and E. L. Meisingset (2021) Spatial clustering by red deer and its relevance for management of chronic wasting disease. *Animals* 2021, 11 (5), p. 1272. Available from: <https://doi.org/10.3390/ani110512>.
- Mysterud, A., L. E. Loe, B. Zimmermann, R. Bischof, V. Veiberg and E. Meisingset (2011) Partial migration in expanding red deer populations at northern latitudes – a role for density dependence?. *Oikos*, 120, pp. 1817-1825. Available from doi: 10.1111/j.1600-0706.2010.19439.x.
- Mysterud, A., O. Strand and C. M. Rolandsen (2019) Efficacy of recreational hunters and marksmen for host culling to combat chronic wasting disease in reindeer. *Wildlife Society Bulletin*, 43 (4), pp. 683-692. Available from doi:10.1002/wsb.1024.
- Nichols, J. D., J. E. Hines, J. R. Sauer, F. W. Fallon, J. E. Fallon and P. J. Heglund (2000) A double observer approach for estimating detection probability and abundance from points counts. *The Auk*, 117 (2), pp. 393-408. Available from: <https://doi.org/10.2307/4089721>.

- Norwegian Mapping Authority (2021) DTM 10 Terrengmodell (UTM33) 2021. [Data set]. Geonorge. Available from: <https://kartkatalog.geonorge.no/metadata/dtm-10-terrengmodell-utm33-2021/774934a0-8f47-4ba1-9201-0ed98776d741>.
- Palencia, P., J. M. Rowcliffe, J. Vicente and P. Acevedo (2021) Assessing the camera trap methodologies used to estimate density of unmarked populations. *Journal of Applied Ecology*, 58 (8), pp. 1583-1592. Available from: <https://doi.org/10.1111/1365-2664.13913>.
- Preston, T. M., M. L. Wildhaber, N. S. Green, J. L. Albers and G. P. Debenedetto (2021) Enumerating white-tailed deer using unmanned aerial vehicles. *Wildlife Society Bulletin* 45 (1), pp. 97-108. Available from doi:10.1002/wsb.1149.
- QGIS Development Team (2020) *QGIS Geographic Information System*. Open Source Geospatial Foundation Project. Available from: <http://qgis.osgeo.org>
- R Core Team (2021) *R: A language and environment for statistical computing*. R Foundation for Statistical Computing, Vienna, Austria. Available from: <https://www.R-project.org/>
- Schneider, C. A., W. S. Rasband and K. W. Eliceiri (2012) NIH Image to ImageJ: 25 years of image analysis. *Nature Methods*, 9 (7), pp. 671-675. Available from doi:10.1038/nmeth.2089.
- Scholten, J., S. R. Moe and S. J. Hegland (2018) Red deer (*Cervus elaphus*) avoid mountain biking trails. *European Journal of Wildlife Research*, 64 (1), pp. 8. Available from: 10.1007/s10344-018-1169-y.
- Schroeder, N. M., A. Panebianco, R. G. Musso and P. Carmanchahi (2020) An experimental approach to evaluate the potential of drones in terrestrial mammal research: a gregarious ungulate as a study model. *Royal Society Open Science*, 7 (1). Available from: <https://doi.org/10.1098/rsos.191482>.
- Scobie, C.A. and C. H. Hugenholtz (2016) Wildlife monitoring with unmanned aerial vehicles: Quantifying distance to auditory detection. *Wildlife Society Bulletin*, 40 (4), pp. 781-785. Available from: <https://doi.org/10.1002/wsb.700>.
- Sequin, E. S., M. M. Jaeger, P. F. Brussard, and R. H. Barrett (2003) Wariness of coyotes to camera traps relative to social status and territory boundaries. *Canadian Journal of Zoology*, 81 (12), pp. 2015-2025. Available from doi:10.1139/z03-204.
- Seymour, A. C., J. Dale, M. Hammill, P. N. Halpin and D.W. Johnston (2017) Automated detection and enumeration of marine wildlife using unmanned aircraft systems (UAS) and thermal imagery. *Scientific Reports*, 7, 45127. Available from doi:10.1038/srep45127.
- Sibbald, A. M., R. J. Hooper, J. E. McLeod and I. J. Gordon (2011) Responses of red deer (*Cervus elaphus*) to regular disturbance by hill walkers. *European Journal of Wildlife Research*, 57 (4), pp. 817-825. Available from: <https://doi-org.ezproxy.uio.no/10.1007/s10344-011-0493-2>.

- Solberg, E. J. and C. M. Rolandsen (2020) *Population reduction of moose and red deer in the Nordfjella region: Experiences from the hunting season 2019/2020*. NINA Report 1813. Norwegian Institute for Nature Research.
- Solberg, E. J., I. M. Rivrud., E. B. Nilsen, V. Veiberg, C. M. Rolandsen, E. L. Meisingset and A. Mysterud (2019) *Population reduction of moose and red deer in the Nordfjella region during the period 2019-2020: Suggested harvesting strategies*. NINA Report 1667. Norwegian Institute for Nature Research.
- Spaan, D., C. Burke, O. McAree, F. Aureli, C. E. Rangel-Rivera, A. Hutschenreiter, S. N. Longmore, P. R. McWhirter and S. A. Wich (2019) Thermal infrared imaging from drones offers a major advance for spider monkey surveys. *Drones*, 3 (2), 34. Available from doi:10.3390/drones3020034.
- Swann, D. E., K. Kawanishi and J. Palmer (2011) Evaluating types and features of camera traps in ecological studies: A guide for researchers, in A. F. O'Connell, J. D. Nichols and K. U. Karanth (eds.) *Camera Traps in Animal Ecology*. Springer, Tokyo, pp. 27-43. Available from: https://doi.org/10.1007/978-4-431-99495-4_3.
- Takehiko, Y. I., A. Miyazaki, L. A. Koyama, K. Kamada and D. Nagamatsu (2022) Antler detection from the sky: deer sex ratio monitoring using. *Wildlife Biology*, e01034. Available from doi:10.1002/wlb3.01034.
- Terletzky, P., R. D. Ramsey and C. M. U. Neale (2012) Spectral characteristics of domestic and wild mammals. *GIScience & Remote Sensing*, 49 (4), pp. 597-608. Available from: <http://dx.doi.org/10.2747/1548-1603.49.4.597>.
- Thorsnæs, G., S. Askheim, E. Helleve and Allkunne (Nynorsk kultursentrum) (2022) Lærdal. *Store Norske Leksikon*. Available from: <https://snl.no/L%C3%A6rdal>. [Accessed 27 April 2022].
- Vermeulen, C., P. Lejeune, J. Lisein, P. Sawadogo and P. Bouché (2013) Unmanned aerial survey of elephants. *PLoS ONE*, 8 (2), e54700. Available from doi:10.1371/journal.pone.0054700.
- Wegge, P., C. P. Pokheral and S. R. Jnawali (2004) Effects of trapping effort and trap shyness on estimates of tiger abundance from camera trap studies. *Animal Conservation*, 7 (3), pp. 251-256. Available from: <https://doi.org/10.1017/S1367943004001441>.
- Williams, P. J., M. B. Hooten, J. N. Womble and M. R. Bower (2017) Estimating occupancy and abundance using aerial images with imperfect detection. *Methods in Ecology and Evolution*, 8 (12), pp. 1679-1689. Available from: <https://doi.org/10.1111/2041-210X.12815>.
- Witczuk, J., S. Pagacz, A. Zmarz and M. Cype (2018) Exploring the feasibility of unmanned aerial vehicles and thermal imaging for ungulate surveys in forests - preliminary results. *International Journal of Remote Sensing*, 39 (15-16), pp. 5504-5521. Available from: <https://doi.org/10.1080/01431161.2017.1390621>.

- Westekemper, K., H. Reinecke, J. Signer, M. Meißner, S. Herzog and N. Balkenhol (2018) Stay on trails – effects of human recreation on the spatiotemporal behavior of red deer *Cervus elaphus* in a German national park. *Wildlife Biology*, 2018 (1), pp. 1-9, wlb.00403. Available from: <https://doi-org.ezproxy.uio.no/10.2981/wlb.00403>.
- Ytrehus, B., D. Grahek-Ogden, O. Strand, M. Tranulis, A. Mysterud, M. Aspholm, S. Jore, G. Kapperud, T. Møretrø, T. Nesbakken, L. Robertson, K. Melby and T. Skjerdal (2018) *Factors that can contribute to spread of CWD - an update on the situation in Nordfjella, Norway*. Opinion of the Panel on biological hazards. Norwegian Scientific Committee for Food and Environment (VKM), Oslo, Norway.
- Årdal municipality, Lærdal municipality and Aurland municipality (2011) *Forvaltningsplan for hjortevilt i Årdal, Lærdal og Aurland [Management plan for deer game in Årdal, Lærdal and Aurland]*. Available from: <https://www.aurland.kommune.no/?id=5913996&cat=410708>.

Appendices

Appendix A: List of survey flights and route perimeters

Table A1: List of survey flights showing name of surveys, date of the flights, at what sampling area the flights were completed, what camera was used for the flights (RGB = daytime, IR = nighttime), meters AGL the UAVs were flown, and the flights' route numbers.

Survey	Date	Sampling area	Camera	AGL (m)	Route
20210307_Fencing_RGB_40m	07.03.2021	Deer Farm	RGB	40	NA
20210307_Fencing_RGB_60m	07.03.2021	Deer Farm	RGB	60	NA
20210307_Fencing_IR_40m	07.03.2021	Deer Farm	IR	40	NA
20210307_Soere_Bjoerkum_RGB_60m_#1	07.03.2021	Søre Bjørkum	RGB	60	1
20210307_Soere_Bjoerkum_RGB_60m_#2	07.03.2021	Søre Bjørkum	RGB	60	2
20210307_Soere_Bjoerkum_RGB_60m_#3	07.03.2021	Søre Bjørkum	RGB	60	3
20210307_Soere_Bjoerkum_RGB_60m_#4	07.03.2021	Søre Bjørkum	RGB	60	4
20210309_Soere_Bjoerkum_IR_40m_#1	09.03.2021	Søre Bjørkum	IR	40	1
20210309_Soere_Bjoerkum_IR_40m_#2	09.03.2021	Søre Bjørkum	IR	40	2
20210309_Soere_Bjoerkum_IR_40m_#3	09.03.2021	Søre Bjørkum	IR	40	3
20210309_Soere_Bjoerkum_IR_40m_#4	09.03.2021	Søre Bjørkum	IR	40	4
20210309_Raa_RGB_40m_#1	09.03.2021	Rå	RGB	40	1
20210309_Raa_RGB_40m_#2	09.03.2021	Rå	RGB	40	2
20210309_Raa_RGB_40m_#3	09.03.2021	Rå	RGB	40	3
20210310_Raa_IR_40m_#1	10.03.2021	Rå	IR	40	1
20210310_Raa_IR_40m_#2	10.03.2021	Rå	IR	40	2
20210310_Raa_IR_40m_#3	10.03.2021	Rå	IR	40	3
20210312_Hauge_IR_40m_#1	12.03.2021	Hauge	IR	40	1
20210312_Hauge_IR_40m_#2	12.03.2021	Hauge	IR	40	2
20210312_Hauge_IR_40m_#3	12.03.2021	Hauge	IR	40	3
20210312_Haugen_RGB_60m_#1	12.03.2021	Haugen	RGB	60	1
20210312_Haugen_RGB_60m_#2	12.03.2021	Haugen	RGB	60	2
20210312_Haugen_RGB_60m_#3	12.03.2021	Haugen	RGB	60	3
20210314_Haugen_IR_40m_#1	14.03.2021	Haugen	IR	40	1
20210314_Haugen_IR_40m_#2	14.03.2021	Haugen	IR	40	2
20210314_Haugen_IR_40m_#3	14.03.2021	Haugen	IR	40	3
20210313_Haugen_RGB_60m_#1	13.03.2021	Haugen	RGB	60	1
20210313_Haugen_RGB_60m_#2	13.03.2021	Haugen	RGB	60	2
20210313_Haugen_RGB_60m_#3	13.03.2021	Haugen	RGB	60	3
20210315_Haugen_IR_40m_#1	15.03.2021	Haugen	IR	40	1
20210315_Haugen_IR_40m_#2	15.03.2021	Haugen	IR	40	2
20210315_Haugen_IR_40m_#3	15.03.2021	Haugen	IR	40	3
20210313_Sprakehaug_RGB_60m_#1	13.03.2021	Sprakehaug	RGB	60	1
20210313_Sprakehaug_RGB_60m_#2_Crash	13.03.2021	Sprakehaug	RGB	60	2
20210315_Sprakehaug_RGB_60m_#3	15.03.2021	Sprakehaug	RGB	60	3
20210315_Sprakehaug_RGB_60m_#4	15.03.2021	Sprakehaug	RGB	60	4
20210315_Sprakehaug_RGB_60m_#5	15.03.2021	Sprakehaug	RGB	60	5
20210408_Soere_Bjoerkum_RGB_60m_#1	08.04.2021	Søre Bjørkum	RGB	40	1

20210408_Soere_Bjoerkum_RGB_60m_#2_Crash	08.04.2021	Søre Bjørkum	RGB	40	2
20210411_Soere_Bjoerkum_IR_40m_#1	11.04.2021	Søre Bjørkum	IR	40	1
20210411_Soere_Bjoerkum_IR_40m_#2	11.04.2021	Søre Bjørkum	IR	40	2
20210411_Soere_Bjoerkum_IR_40m_#3	11.04.2021	Søre Bjørkum	IR	40	3
20210411_Soere_Bjoerkum_IR_40m_#4	11.04.2021	Søre Bjørkum	IR	40	4
20210411_Raa_RGB_40m_#1	11.04.2021	Rå	RGB	40	1
20210411_Raa_RGB_40m_#2	11.04.2021	Rå	RGB	40	2
20210411_Raa_RGB_40m_#3	11.04.2021	Rå	RGB	40	3
20210408_Raa_IR_40m_#1	08.04.2021	Rå	IR	40	1
20210408_Raa_IR_40m_#2	08.04.2021	Rå	IR	40	2
20210408_Raa_IR_40m_#3	08.04.2021	Rå	IR	40	3
20210408_Haugen_RGB_60m_#1	08.04.2021	Haugen	RGB	60	1
20210408_Haugen_RGB_60m_#2	08.04.2021	Haugen	RGB	60	2
20210408_Haugen_RGB_60m_#3	08.04.2021	Haugen	RGB	60	3
20210407_Haugen_IR_40m_#1	07.04.2021	Haugen	IR	40	1
20210407_Haugen_IR_40m_#2	07.04.2021	Haugen	IR	40	2
20210407_Haugen_IR_40m_#3	07.04.2021	Haugen	IR	40	3
20210411_Sprakehaug_RGB_60m_#3	11.04.2021	Sprakehaug	RGB	60	3
20210411_Sprakehaug_RGB_60m_#4	11.04.2021	Sprakehaug	RGB	60	4
20210411_Sprakehaug_RGB_60m_#5	11.04.2021	Sprakehaug	RGB	60	5
20210408_Sprakehaug_IR_40m_#1	08.04.2021	Sprakehaug	IR	40	1
20210408_Sprakehaug_IR_40m_#2	08.04.2021	Sprakehaug	IR	40	2
20210408_Sprakehaug_IR_40m_#3	08.04.2021	Sprakehaug	IR	40	3



Figure A1: Map showing Søre Bjørkum with route perimeters of the sampling area’s survey flights (Google Earth V 7.3.3, 2020b). Perimeters of daytime routes are shown in red with route number and perimeters of nighttime routes are shown in blue. Top side of map is north.



Figure A2: Map showing Rå with route perimeters of the sampling area’s survey flights (Google Earth V 7.3.3, 2020c). Perimeters of daytime routes are shown in red with route number and perimeters of nighttime routes are shown in blue. Top side of map is north.



Figure A3: Map showing Haugen with route perimeters of the sampling area's survey flights (Google Earth V 7.3.3, 2020d). Perimeters of daytime routes are shown in red with route number and perimeters of nighttime routes are shown in blue. Top side of map is north.



Figure A4: Map showing Sprakehaug with route perimeters of the sampling area's survey flights (Google Earth V 7.3.3, 2020e). Perimeters of daytime routes are shown in red with route number and perimeters of nighttime routes are shown in blue. Top side of map is north.

Appendix B: Settings of UAVS and apps

Before take-off, the UAV was calibrated, and set to positioning flight mode (“P-mode”) by means of the custom switch on the side of the remote controller. When using the DJI Mavic 2 Pro-drone, settings of the DJI 4.0-app were kept on default mode except for some options that were changed to the following:

- Focus: infinity
- Shutter priority: S
- ISO: auto ON
- Shutter: 1/1000
- Image size: 3:2
- Image format: JPEG
- White balance: auto ON

When using one of the DJI Mavic 2 Enterprise Dual-drone, the same procedure was completed for the DJI Pilot-app except the options changed were:

- Visible: set between “IR” and “Visible”
- ISO: ON and calibrated for optimal visibility of deer
- Pattern: calibrated for optimal visibility of deer
- Temperature: calibrated for optimal visibility of deer (narrow temperature)
- FFC: auto ON

Identification of red deer from the thermal infrared camera was most successful when the temperature range of the sensors was set to detect heat signatures between 5-14°C both in March and April. The optimal color palette was found to be the pattern ‘hotspot’ where the coldest areas appeared black, hotter areas light grey, and the hottest spots were red and dark orange. This temperature range and color palette created the largest thermal contrast between the target red deer and landscape elements (e.g., rivers, rocks, tree trunks, etc.).

Apart from selection of UAV model, the settings of the Map Pilot-app were identical for the Pro-drone and Enterprise Dual-drones. The changes made to the default settings were:

- Model: DJI Mavic 2 Pro *or* DJI Mavic 2 Zoom/Enterprise
- Image format: RAW image OFF
- Speed class rating: Class 3
- Enable radius guide: OFF

- Camera control: Nadir
- Speed max: 5 m/s
- Overlap: 80% (forelap), 60% (sidelap)

Appendix C: List of GPS-collared red deer and potential survey matches

As common features could not be detected in the dark images from the nighttime survey flights, orthomosaics could not be created. Instead, the less accurate KML-files with route perimeters were uploaded to QGIS, together with the GPS-positions, to determine if GPS-collared deer had been present during sampling.

Table C1: List of GPS-collared red deer/survey matches showing survey names, start and end time of sampling, number associated with deer whose home range overlapped with the flight routes of surveys, and number associated with deer present inside the routes' perimeters during sampling. NA under "GPS-deer number" means no GPS-collared deer were associated with study area *or* that the GPS-coordinates were not recorded during time of sampling due to technical errors. NA under "Match" means no coordinates of any GPS-collared deer were recorded in the corresponding survey's flight route during sampling. "Possibly" means the GPS-collared deer was recorded close to/by the boarder of the survey flight route during sampling but no coordinates were recorded directly inside the route.

Survey	Start time	End time	GPS-deer number	Match
20210307_Soere_Bjoerkum_RGB_60m_#1	14:04	14:31	31, 34	31, 34
20210307_Soere_Bjoerkum_RGB_60m_#2	15:23	15:37	31, 34	31
20210307_Soere_Bjoerkum_RGB_60m_#3	14:45	14:53	31, 34	NA
20210307_Soere_Bjoerkum_RGB_60m_#4	15:03	15:13	31, 34	NA
20210309_Soere_Bjoerkum_IR_40m_#1	02:01	02:08	31, 34	NA
20210309_Soere_Bjoerkum_IR_40m_#2	02:14	02:21	31, 34	Possibly 31, 34
20210309_Soere_Bjoerkum_IR_40m_#3	02:29	02:37	31, 34	NA
20210309_Soere_Bjoerkum_IR_40m_#4	02:43	02:48	31, 34	NA
20210309_Raa_RGB_40m_#1	10:00	10:10	35	NA
20210309_Raa_RGB_40m_#2	10:39	10:45	35	NA
20210309_Raa_RGB_40m_#3	10:57	11:14	35	NA
20210310_Raa_IR_40m_#1	02:02	02:24	35	NA
20210310_Raa_IR_40m_#2	02:32	02:48	35	NA
20210310_Raa_IR_40m_#3	02:58	03:14	35	NA
20210312_Hauge_IR_40m_#1	05:20	05:33	NA	NA
20210312_Hauge_IR_40m_#2	05:38	05:57	NA	NA
20210312_Hauge_IR_40m_#3	06:05	06:13	NA	NA
20210312_Haugen_RGB_60m_#1	08:55	09:00	NA	NA
20210312_Haugen_RGB_60m_#2	09:14	09:22	NA	NA
20210312_Haugen_RGB_60m_#3	09:39	09:45	NA	NA
20210314_Haugen_IR_40m_#1	04:51	05:04	NA	NA
20210314_Haugen_IR_40m_#2	05:09	05:22	NA	NA
20210314_Haugen_IR_40m_#3	05:28	05:39	NA	NA
20210313_Haugen_RGB_60m_#1	08:58	09:06	42	NA
20210313_Haugen_RGB_60m_#2	09:12	09:19	42	NA
20210313_Haugen_RGB_60m_#3	09:26	09:33	42	NA
20210315_Haugen_IR_40m_#1	04:03	04:19	42	NA
20210315_Haugen_IR_40m_#2	04:28	04:41	42	NA

20210315_Haugen_IR_40m_#3	04:48	04:59	42	NA
20210313_Sprakehaug_RGB_60m_#1	14:59	15:06	43	NA
20210313_Sprakehaug_RGB_60m_#2_Crash	15:14	15:20	43	Not enough photos for orthophotography
20210315_Sprakehaug_RGB_60m_#3	10:03	10:09	43	NA
20210315_Sprakehaug_RGB_60m_#4	10:20	10:28	43	NA
20210315_Sprakehaug_RGB_60m_#5	10:44	10:52	43	NA
20210408_Soere_Bjoerkum_RGB_60m_#1	09:58	10:21	31, 34	NA
20210408_Soere_Bjoerkum_RGB_60m_#2_Crash	10:27	10:48	31, 34	NA
20210411_Soere_Bjoerkum_IR_40m_#1	01:08	01:16	31	Possibly 34
20210411_Soere_Bjoerkum_IR_40m_#2	01:24	01:30	31	Possibly 34
20210411_Soere_Bjoerkum_IR_40m_#3	01:39	01:47	31	Possibly 34
20210411_Soere_Bjoerkum_IR_40m_#4	01:57	02:02	31	NA
20210411_Raa_RGB_40m_#1	11:02	11:07	35	NA
20210411_Raa_RGB_40m_#2	11:16	11:26	35	NA
20210411_Raa_RGB_40m_#3	11:32	11:52	35	NA
20210408_Raa_IR_40m_#1	00:59	01:22	35	NA
20210408_Raa_IR_40m_#2	01:28	01:45	35	NA
20210408_Raa_IR_40m_#3	01:50	02:06	35	NA
20210408_Haugen_RGB_60m_#1	07:53	08:02	42	NA
20210408_Haugen_RGB_60m_#2	08:06	08:14	42	NA
20210408_Haugen_RGB_60m_#3	08:20	08:26	42	NA
20210407_Haugen_IR_40m_#1	01:12	01:28	42	NA
20210407_Haugen_IR_40m_#2	01:34	01:47	42	NA
20210407_Haugen_IR_40m_#3	01:50	02:07	42	NA
20210411_Sprakehaug_RGB_60m_#3	08:02	08:10	43	NA
20210411_Sprakehaug_RGB_60m_#4	08:17	08:35	43	NA
20210411_Sprakehaug_RGB_60m_#5	08:40	08:52	43	NA
20210408_Sprakehaug_IR_40m_#1	03:54	04:06	43	NA
20210408_Sprakehaug_IR_40m_#2	04:21	04:42	43	NA
20210408_Sprakehaug_IR_40m_#3	04:52	05:12	43	Possibly 43

Appendix D: R-code

All scripts were created by Torbjørn Håkan Ergon and Julie Bommerlund using R v4.1.1 or R v4.2.0 via RStudio v1.3.1093 for Windows (R Core Team, 2021).

D1. R-code for section 2.5.1 Selecting focal images

For each survey flight, the aerial images were uploaded to a folder. For each folder, the following code was used to align the images:

```
# R-packages used:
library(exifr)
library(tidyverse)
library(leaflet)
library(rgdal)

# Choosing folder
folder = "../Fencing/20210307_Fencing_RGB_40m/RGB/" # Example folder

files = list.files(path = folder, pattern = "*.JPG")
dat = read_exif(paste0(folder, files))

# Plotting all points on a satellite image
leaflet(dat) %>%
  addProviderTiles("Esri.WorldImagery") %>%
  addMarkers(~ GPSLongitude, ~ GPSLatitude)

cord.dec = SpatialPoints(cbind(dat$GPSLongitude, dat$GPSLatitude),
proj4string=CRS("+proj=longlat +init=epsg:4326"))

X = spTransform(cord.dec, CRS("+init=epsg:32633"))
# UTM coordinates, using this gives the distance in meters

im_num = substring(files,5,8)

plot(X, pch=".")
text(X@coords[,1], X@coords[,2], im_num, cex = 0.6)
```

D2. R-code for section 2.5.3 Checking for GPS-collared deer

Every TXT-file with the coordinates of the GPS-collared deer were filtered to only contain the positions during time of sampling using the following code:

```
# R-packages used:
library(rgdal)
library(tidyverse)

# Choosing TXT-file
GPS1_lilla_31 <- read.table
("20210307_Søre_Bjørkum_GPS_Collar23262_lilla_31_dag_edited.txt", header =
TRUE, dec = ",") # Example TXT-file

# Filtering time
GPS1_lilla_31 <- GPS1_lilla_31 %>% filter(UTC_Time > "12.00.38" & UTC_Time
< "15.00.09" ) %>% arrange(UTC_Time)
```

D3. R-code for section 2.5.4 Making count data with site covariates

Count data

For each row and column of the matrix, a function was used to add a threshold distance value to all values but the lowest value. The remaining values below the threshold value then represented deer seen by both observers, i.e., the row name and column name represented the same deer. Rows exclusively containing values above the threshold value, represented deer only seen by observer 1, while the same was true for columns and observer 2. Based on information obtained from ImageJ by marking individual deer with different positions (e.g., above the head, underneath the rump, etc.), this threshold distance value was set to 200 pixels. The following code was used to create this count data:

```
# R-package used:
library(tidyverse)

# Importing files with counts made by observer 1 (A) and 2 (B)
Counts_B = read.csv("../Data/Counts_B.csv")
Counts_A = read.csv("../Data/Counts_A.csv")

# Setting threshold value
threshold = 200

# Creating function used for counting animals seen by both
disc = function(x) {
  xx = x
  xx[x != min(x)] = threshold + 1
  return(xx)
}

# Counting
Counts = NULL
surveys = unique(c(Counts_A$Survey, Counts_B$Survey))
for(survey in surveys) {
  B = Counts_B[Counts_B$Survey == survey & !is.na(Counts_B$Focal_image),]
  A = Counts_A[Counts_A$Survey == survey & !is.na(Counts_A$Focal_image),]
  F_images = unique(c(A$Focal_image, B$Focal_image))
  for(f_im in F_images) {
    images = unique(c(A$Image[A$Focal_image == f_im],
                     B$Image[B$Focal_image == f_im]))
    for(im in images) {
      b = subset(B, subset = Image == im)
      a = subset(A, subset = Image == im)
      n_a = nrow(a)
      n_b = nrow(b)

      # Animals only seen by observer 2 in unique image
      if(n_a == 0) {
        n_both = 0
        n_only_a = 0
        n_only_b = n_b

      # Animals only seen by observer 1 in unique image
      } else if(n_b == 0) {
        n_both = 0
        n_only_a = n_a
      }
    }
  }
}
```

```

        n_only_b = 0
    } else {
# Computing matrix with Euclidean distances between animals
seen in same image
    Dist = matrix(NA, n_a, n_b)
    for(i in 1:n_a){
        for(j in 1:n_b){
            dx = a$X[i] - b$X[j]
            dy = a$Y[i] - b$Y[j]
            Dist[i,j] = sqrt(dx^2 + dy^2)
        }
    }

# Adding threshold value to all but lowest values of rows
and columns of matrices
D = t(apply(Dist, 1, disc))
D = matrix(apply(D, 2, disc), ncol = ncol(D))
n_both = sum(D < threshold)
n_only_a = nrow(D) - n_both
n_only_b = ncol(D) - n_both
}
temp = data.frame(
    Survey = survey,
    Focal_image = f_im,
    Image = im,
    n_both = n_both,
    n_only_a = n_only_a,
    n_only_b = n_only_b
)
Counts = rbind(Counts, temp) # Counts saved as R- and
                             CSV-file
    }
}
}

```

Site covariate data

The site covariates area, position, elevation, proportion of forest, aspect, slope, and distance from field/forest were added to each focal image of the sampling areas (i.e., areas with wild deer) using the following code:

```

# R-packages used:
library(raster)
library(rgdal)

# Importing projected images
folders = list.dirs("../././Projected_Img/All_Focal_Images")
folders = folders[-1]
surveys = dir("../././Projected_Img/All_Focal_Images")

# Loading digital elevation model
DEM = raster("../././QGIS/Laerdal kartdata/Elevation/merge_5m.tif")

# Loading and transforming shape files with field and forest boundaries
field_df = readOGR("Field_Boundary_Shapefile_UTM33N.shp")
field_sp = as(field_df, "SpatialPointsDataFrame")
forest_df = readOGR("Forest_Boundary_Shapefile_UTM33N.shp")
forest_sp = as(forest_df, "SpatialPointsDataFrame")

```

```

# Loading and transforming shape file with forest/no-forest
no_forest = raster("Forest_Polygon_Raster_UTM33N.tif")

# Loading and transforming shape file with field/no-field
field = raster("Field_Polygon_Raster_UTM33N.tif")

# Adding area, positions, elevation, proportion of forest, aspect, slope,
and distance from field/forest to each image
SiteCovs = NULL # Site covariates
cat(length(surveys), "Surveys \n")
for(i in 3:length(folders)){ # Disregard deer farm
  folder = folders[i]
  survey = surveys[i]
  files = dir(folder)
  temp = data.frame(
    Survey = survey,
    File = files)
  cat("\n", i, ": Survey: ", survey, " (", length(files), "images): ",
    sep="")
  for(j in 1:length(files)){
    cat(j, "-", sep="")
    file = files[j]
    footprint = raster(paste(folder, file, sep="/"))
    dem = crop(DEM, extent(footprint))

    # Area
    temp$Area[j] = sum(matrix(footprint)!=0) * 0.1 * 0.1 # Adding area

    # Mean position
    pos = rasterToPoints(footprint)
    pos = pos[pos[,3] != 0, 1:2]
    mean_pos = apply(pos, 2, mean) # Mean position of all the pixels in
    the raster

    temp$mean_x[j] = mean_pos["x"]
    temp$mean_y[j] = mean_pos["y"]

    # Elevation at mean position of footprint
    temp$elevation_at_mean_pos[j] = extract(dem, cbind(mean_pos["x"],
    mean_pos["y"]))

    # Mean, min and max of elevation
    elev = extract(dem, pos)
    temp$mean_elevation[j] = mean(elev, na.rm = TRUE)
    temp$min_elevation[j] = min(elev, na.rm = TRUE)
    temp$max_elevation[j] = max(elev, na.rm = TRUE)

    # Proportion forest
    no_forest_pos = extract(no_forest, pos)
    temp$proportion_forest[j] = mean(is.na(no_forest_pos))

    # Proportion no field
    field_pos = extract(field, pos)
    temp$proportion_no_field[j] = mean(is.na(field_pos))

    # Aspect
    aspect_layer = terrain(dem, opt="aspect", unit = "degrees")
    aspects = extract(aspect_layer, pos)
    temp$aspect_deg[j] = mean(aspects, na.rm = TRUE)

    # Slope
    slope_layer = terrain(dem, opt="slope", unit = "degrees")
    slopes = extract(slope_layer, pos)
    temp$slope_deg[j] = mean(slopes, na.rm = TRUE)

```

```

# Distance from field
field_dist_layer = distanceFromPoints(dem, field_sp)
field_dist_raw = extract(field_dist_layer, pos)
field_dist = field_dist_raw * is.na(no_field_pos) # Area covered by
                                                  polygon = distance
                                                  of 0 m

temp$field_dist_at_mean_pos[j] = extract(field_dist_layer,
cbind(mean_pos["x"], mean_pos["y"]))
temp$mean_field_dist[j] = mean(field_dist, na.rm = TRUE)
temp$min_field_dist[j] = min(field_dist, na.rm = TRUE)
temp$max_field_dist[j] = max(field_dist, na.rm = TRUE)

# Distance from forest
forest_dist_layer = distanceFromPoints(dem, forest_sp)
forest_dist_raw = extract(forest_dist_layer, pos)
forest_dist = forest_dist_raw * is.na(no_forest_pos)
temp$forest_dist_at_mean_pos[j] = extract(forest_dist_layer,
cbind(mean_pos["x"], mean_pos["y"]))
temp$mean_forest_dist[j] = mean(forest_dist, na.rm = TRUE)
temp$min_forest_dist[j] = min(forest_dist, na.rm = TRUE)
temp$max_forest_dist[j] = max(forest_dist, na.rm = TRUE)
}
SiteCovs = rbind(SiteCovs, temp) # SiteCovs saved as R- and CSV-file
}

```

Combining count data and site covariate data

For the wild deer, the data containing the counts was combined with the site covariates data and other site covariate data obtained during flights, using the following code:

```

# R-packages used:
library(tidyverse)

# Loading and aggregating data on counts
load("Counts.Rdata")
CountsAggr = aggregate(Counts[,4:6], by = list(Counts$Focal_image,
Counts$Survey), FUN = sum)
names(CountsAggr)[1:2] = c("Focal_image", "Survey")

# Loading site covariate data
load("../Area/SiteCovs.Rdata")
CountData = SiteCovs

# Extracting only image number and adding 0s to image number
CountData$Focal_image = substring(CountData$File, 14, 17)
CountsAggr$Focal_image = paste0(lapply(4-nchar(CountsAggr$Focal_image),
function(i) paste(rep(0,i), collapse = "")), CountsAggr$Focal_image)

# Adding count data to site covariate data (all focal images, including no
deer)
row.names(CountsAggr) = paste(CountsAggr$Survey, CountsAggr$Focal_image,
sep="_")

CountData$n_both = CountsAggr[paste(CountData$Survey,
CountData$Focal_image, sep="_"), "n_both"]
CountData$n_only_ab = CountsAggr[paste(CountData$Survey,
CountData$Focal_image, sep="_"), "n_only_a"]
CountData$n_only_jb = CountsAggr[paste(CountData$Survey,
CountData$Focal_image, sep="_"), "n_only_b"]

```



```

CountData$n_both[is.na(CountData$n_both)] = 0
CountData$n_only_ab[is.na(CountData$n_only_ab)] = 0
CountData$n_only_jb[is.na(CountData$n_only_jb)] = 0

# Loading data from flights
FlightData = read.csv("../Data/Flight_Data.csv")
names(FlightData)[names(FlightData) == 'i..Survey'] <- 'Survey'

# Removing empty lines
FlightData = FlightData[FlightData$Survey != "",]

# Transforming dates to date objects and adding month
FlightData$Date_str = FlightData$Date
FlightData$Date = as.Date(FlightData$Date_str, format = "%d.%m.%Y")
FlightData$Month = months(FlightData$Date)

# Making unique route IDs
FlightData$Route_within_survey = FlightData$Route
FlightData$Route = substring(FlightData$Survey, 10)
table(FlightData$Route, FlightData$Month)

# Keeping more variables from flight data
sub_FlightData <- FlightData[, c("Survey", "Study_area", "Route", "Month",
"Date", "Weather", "Temperature_C", "Snow")]

# Joining count data and flight data
CountData_original = CountData
CountData <- left_join(sub_FlightData, CountData, by = "Survey") # Joining
                                                                    data
                                                                    sets by
                                                                    "Survey"

CountData = CountData[!grepl("_IR_", CountData$Survey),] # Removing IR
                                                                    surveys

# CountData saved as R- and CSV-file

```

A similar but simpler (i.e., with less site covariates) data set was created for the data obtained from the enclosure.

D4. R-code for section 2.5.5 Statistical modeling

Predictor variables

The code below gives an example of how the different Poisson GLMMs were created to evaluate potential predictor variables. The model in this example includes the variable ‘field distance’:

```

# R-package used:
library(glmTMB)

# Loading count data
load("../Analysis/Make_CountData/CountData.RData")

# Sorting/dividing dataset:
CountData$n_all = CountData$n_both + CountData$n_only_jb +
CountData$n_only_ab

CountData$Site = paste("site", 1:nrow(CountData), sep="_")
CountData$Route_Month = paste(CountData$Route, CountData$Month)
CountData$StudyArea_Month = paste(CountData$Study_area, CountData$Month)

```

```
# Excluding data from enclosure
glmm_Data = CountData[CountData$Survey != "20210307_Fencing_RGB_40m" &
CountData$Survey != "20210307_Fencing_RGB_60m",]

# Fitting GLMM model
fit1 = glmmTMB(n_all ~ 1 + mean_field_dist, offset = log(Area/10000), data =
glmm_Data, family=poisson)

summary(fit1)
```

The results from this example model were as follows:

```
## Family: poisson ( log )
## Formula:          n_all ~ 1 + mean_field_dist
## Data: glmm_Data
## Offset: log(Area/10000)
##
##      AIC      BIC   logLik deviance df.resid
##   330.2    337.6  -163.1   326.2     299
##
##
## Conditional model:
##              Estimate Std. Error z value Pr(>|z|)
## (Intercept)  -1.774530   0.292011  -6.077 1.23e-09 ***
## mean_field_dist  0.002983   0.001190   2.507  0.0122 *
## ---
## Signif. codes:  0 '***' 0.001 '**' 0.01 '*' 0.05 '.' 0.1 ' ' 1
```

Prior

The detection probabilities of observer 1 and 2, i.e., p_1 and p_2 , derived from the data of the deer farm enclosure (where the density was known) were used to create priors for p_1 and p_2 of the wild deer data. The following model was created to find these posterior values (p_1 and p_2) of the data from the enclosure:

```
# R-packages used:
library(nimble)
library(coda)

# Defining the model
DoubleObsMultisiteCode_fence <- nimbleCode({

# Model
for(s in 1:N_surv){
  Psum[s] <- 1-(1-p[s])*(1-p[s])
  pi[1,s] <- p[s]*(1-p[s])/Psum[s]
  pi[2,s] <- (1-p[s])*p[s]/Psum[s]
  pi[3,s] <- p[s]*p[s]/Psum[s]
  mu[s] <- log(mean_lambda) - 0.5*sigma[s]*sigma[s]
  for(i in 1:N_sites[s]){
    # Process model:
    N[s,i] ~ dpois(lambda[s,i]*area[s,i])
    lambda[s,i] <- exp(mu[s] + epsilon[s,i])
    epsilon[s,i] ~ dnorm(0, sd = sigma[s])
    # Observation model:
    Y[s,i] ~ dbin(Psum[s], N[s,i])
    y[s, i, 1:3] ~ dmulti(pi[1:3,s], Y[s,i])
  }
}
```

```

}
}

# Priors
for(s in 1:N_surv){
  sigma[s] ~ dunif(0, 5) # Low to avoid convergence to one side/value
  p[s] ~ dunif(0, 1) # 0 = no animals detected, 1 = all animals detected
} # Prior knowledge kept vague by giving priors a uniform distribution

mean_lambda <- 117/5 # Deterministic! No. deer /
                    Size of enclosure in hectare

# Derived parameters
for(s in 1:N_surv){
  median_lambda[s] <- exp(mu[s])
}
})

# Loading the data
load("../..//Analysis/Make_CountData/CountData_Fence.RData")

# Sorting the data
UseData_fence = CountData_Fence[!is.na(CountData_Fence$Area),]
UseData_fence$Survey = factor(UseData_fence$Survey,
levels = unique(UseData_fence$Survey)) # Sorted as in data
N_sites = table(UseData_fence$Survey)
UseData_fence$Site = unlist(lapply(N_sites, function(i) 1:i))

Counts_fence = rbind(
  cbind(UseData_fence[,1:4], Site = UseData_fence$Site, Cat = "only_ab",
  Count = UseData_fence$n_only_ab),
  cbind(UseData_fence[,1:4], Site = UseData_fence$Site, Cat = "only_jb",
  Count = UseData_fence$n_only_jb),
  cbind(UseData_fence[,1:4], Site = UseData_fence$Site, Cat = "both",
  Count = UseData_fence$n_both)
)

Counts_fence$Cat = factor(Counts_fence$Cat, levels = c("only_ab",
"only_jb", "both"))
y = tapply(Counts_fence$Count, list(Counts_fence$Survey, Counts_fence$Site,
Counts_fence$Cat), sum)
Y = apply(y, c(1,2), sum)
area = tapply(UseData_fence$Area, list(UseData_fence$Survey, UseData_fence$
Site), sum)/10000 # Area in hectare

# Function for initial values
colsumy = apply(y, 3, sum, na.rm=TRUE)
p1hat = colsumy[3]/(colsumy[2]+colsumy[3])
p2hat = colsumy[3]/(colsumy[1]+colsumy[3])
phat = (p1hat+p2hat)/2
Nhat = apply(Y, 1, sum, na.rm=TRUE)/(1-(1-p1hat)*(1-p2hat)) # For all sites
                                                                combined

lambdahat = (Nhat/N_sites)/apply(area, 1, mean, na.rm=TRUE) + 0.01
# Adding a small value since we get -Inf from log(lambdahat=0)

Inits = function(){
  N = round(Y/(1-(1-p1hat)*(1-p2hat)), 0)
  N[is.na(N)] = 0
  sigma = runif(2, 0, 0.1)
  list(
    epsilon = matrix(rnorm(nrow(Y)*ncol(Y), 0, sigma) , nrow = nrow(Y),
    ncol = ncol(Y)),
    p = exp(log(phat)*runif(2, 0.9, 1.1)),
    N = N,

```

```

    sigma = sigma
  )
}

# Setting up the MCMC
DoubleObsMultisiteModel <- nimbleModel(
  DoubleObsMultisiteCode_fence,
  constants = list(lamblow = 0.1*mean(lambdahat),
    lambupp = 10*mean(lambdahat), # 0.1 to 10 times point estimate
    N_surv = length(N_sites),
    N_sites = N_sites),
  data = list(y=y, Y=Y, area = area),
  inits = Inits()
)

CDoubleObsMultisiteModel <- compileNimble(DoubleObsMultisiteModel)
DoubleObsMultisiteConf <- configureMCMC(DoubleObsMultisiteModel, monitors =
c("median_lambda", "p", "mu", "sigma"))
DoubleObsMultisiteMCMC <- buildMCMC(DoubleObsMultisiteConf)
CDoubleObsMultisiteMCMC <- compileNimble(DoubleObsMultisiteMCMC)

posterior_samples_fence_p <- runMCMC(
  CDoubleObsMultisiteMCMC,
  niter=500000,
  nburnin=100000,
  nchain=3,
  thin=2,
  inits = Inits,
  samplesAsCodaMCMC = TRUE)

# Posterior_samples_fence_p saved as R- and CSV-file

```

The code below was used to create priors of μ and σ based on p_1 and p_2 derived from data of fenced deer:

```

# Loading the data
load(file = "posterior_samples_fence_p.RData")

# Creating a vector with p's from all 3 chains
posterior_samples_p_fence = c(posterior_samples_fence_p$chain1[, "p[2]"],
posterior_samples_fence_p$chain2[, "p[2]"], posterior_samples_fence_p$chain3[, "
p[2]"])

# Taking logit of p's
logit = function(p) log(p/(1-p))
logit_posterior_samples_p_fence = logit(posterior_samples_p_fence)

# Finding logit means and SDs
mean_logit_posterior_samples_p_fence = mean(logit_posterior_samples_p_fence
)
sd_logit_posterior_samples_p_fence = sd(logit_posterior_samples_p_fence)

# Making prior mu and sigma from logit means and SDs
mu_logit_p = mean_logit_posterior_samples_p_fence
sigma_logit_p = 1.2*sd_logit_posterior_samples_p_fence

```

Model

The model was created using the following code:

```
# R-packages used:
library(nimble)
library(coda)

# Defining the model
DoubleObsMultisiteCode <- nimbleCode({
  # Model
  Psum <- 1-(1-p1)*(1-p2)
  pi[1] <- p1*(1-p2)/Psum
  pi[2] <- (1-p1)*p2/Psum
  pi[3] <- p1*p2/Psum

  for(s in 1:N_surv){
    for(i in 1:N_sites[s]){
      # Process model:
      N[s,i] ~ dpois(lambda[s,i]*area[s,i])
      lambda[s,i] <- exp(mu[s,i] + epsilon[s,i])
      mu[s,i] <- mu0[sam[s]] + x[s,i]*beta
      epsilon[s,i] ~ dnorm(0, sd = sigma)
      # Observation model:
      Y[s,i] ~ dbin(Psum, N[s,i])
      y[s, i, 1:3] ~ dmulti(pi[1:3], Y[s,i])
    }
  }

  # Priors
  for(k in 1:N_sam){
    mu0[k] ~ dunif(log(lamblow[k]), log(lambupp[k]))
  }

  beta ~ dnorm(0, sd=2) # Assume that x is standardized
                        (x_standard = (x-mean(x))/sd(x))

  logit_p1 ~ dnorm(mu_logit_p, sd = sigma_logit_p) # Values from enclosure
  logit_p2 ~ dnorm(mu_logit_p, sd = sigma_logit_p) data
  p1 <- exp(logit_p1)/(1+exp(logit_p1))
  p2 <- exp(logit_p2)/(1+exp(logit_p2))

  sigma ~ dgamma(0.1, 0.1)

  # Derived parameters: Mean and median densities at mean x
  for(k in 1:N_sam){
    median_lambda[k] <- exp(mu0[k])
    mean_lambda[k] <- exp(mu0[k] + 0.5*sigma^2)
  }
})

# Loading the data
load("../..//Analysis/Make_CountData/CountData.RData")

# Removing NAs and surveys from enclosure
UseData = CountData[!is.na(CountData$Area) & CountData$Survey != "20210307_
Fencing_RGB_40m",]
UseData$Survey = factor(UseData$Survey, levels = unique(UseData$Survey))
# Sorted as in data

# Adding column "Site"
N_sites = table(UseData$Survey)
UseData$Site = unlist(lapply(N_sites, function(i) 1:i))
```

```

# Making "Counts"
Counts = rbind(
  cbind(UseData[,1:4], Site = UseData$Site, Cat = "only_ab",
Count = UseData$n_only_ab),
  cbind(UseData[,1:4], Site = UseData$Site, Cat = "only_jb",
Count = UseData$n_only_jb),
  cbind(UseData[,1:4], Site = UseData$Site, Cat = "both",
Count = UseData$n_both)
)

Counts$Cat = factor(Counts$Cat, levels = c("only_ab", "only_jb", "both"))

y = tapply(Counts$Count, list(Counts$Survey, Counts$Site, Counts$Cat), sum)
# 3D array: row = survey, column = site (focal image), layer = Cat

Y = apply(y, c(1,2), sum) # Matrix with survey x no. deer

area = tapply(UseData$Area, list(UseData$Survey, UseData$Site), sum)/10000
# Area in hectare

mean_field_dist = tapply(UseData$mean_field_dist, list(UseData$Survey,
UseData$Site), sum) # Changed for mean forest distance and mean elevation

# Making standardize function
standardize = function(x) (x-mean(x, na.rm=TRUE))/sd(x, na.rm=TRUE)

# Making index for study area and month
Counts$StudyArea_Month = paste(Counts$Study_area, Counts$Month, sep="_")
tab = table(Counts$Survey, Counts$StudyArea_Month)
sam = apply(tab, 1, function(i) which(i != 0))

# Creating function for initial values
colsumy = apply(y, 3, sum, na.rm=TRUE)
p1hat = colsumy[3]/(colsumy[2]+colsumy[3])
p2hat = colsumy[3]/(colsumy[1]+colsumy[3])
Nhat = apply(Y, 1, sum, na.rm=TRUE)/(1-(1-p1hat)*(1-p2hat)) # For all sites
                                                                combined

lambdahat_surv = (Nhat/N_sites)/apply(area, 1, mean, na.rm=TRUE) + 0.01
lambdahat = tapply(lambdahat_surv, list(sam), mean)

Inits = function(){
  N = round(Y/(1-(1-p1hat)*(1-p2hat)), 0)
  N[is.na(N)] = 0
  sigma = runif(1, 0, 0.1)
  p1 = exp(log(p1hat)*runif(1, 0.9, 1.1))
  p2 = exp(log(p2hat)*runif(1, 0.9, 1.1))
  list(
    mu0 = log(lambdahat*runif(length(lambdahat), 0.9, 1.1)),
    epsilon = matrix(rnorm(nrow(Y)*ncol(Y), 0, sigma),
                      nrow = nrow(Y), ncol = ncol(Y)),
    logit_p = rnorm(mean_logit_posterior_samples_p_fence,
                    sd_logit_posterior_samples_p_fence/5),
    N = N,
    sigma = sigma,
    beta = runif(1, -0.5, 0.5)
  )
}

# Setting up the MCMC
DoubleObsMultisiteModel <- nimbleModel(
  DoubleObsMultisiteCode,
  constants = list(lambblow = 0.1*lambdahat, # 0.1 to 10 times point
                                                           estimate
                  lambupp = 10*lambdahat,
                  N_surv = length(N_sites),

```



```

        N_sites = N_sites,
        mu_logit_p = mu_logit_p,
        sigma_logit_p = sigma_logit_p,
        sam = sam,
        N_sam = length(unique(sam)),
        area = area,
        x = standardize(mean_field_dist) # Changed for mean
                                         forest distance and
                                         mean elevation
    ),
    data = list(y=y, Y=Y),
    inits = Inits()
)

CDoubleObsMultisiteModel <- compileNimble(DoubleObsMultisiteModel)
DoubleObsMultisiteConf <- configureMCMC(DoubleObsMultisiteModel, monitors =
c("median_lambda", "mean_lambda", "p1", "p2", "mu0", "sigma", "beta"))
DoubleObsMultisiteMCMC <- buildMCMC(DoubleObsMultisiteConf)
CDoubleObsMultisiteMCMC <- compileNimble(DoubleObsMultisiteMCMC)

posterior_samples <- runMCMC(
  CDoubleObsMultisiteMCMC,
  niter=500000,
  nburnin=100000,
  nchain=3,
  thin=2,
  inits = Inits,
  samplesAsCodaMCMC = TRUE)

plot(posterior_samples)
summary(posterior_samples)

# Posterior_samples saved as R- and CSV-file

```

Appendix E: Model definition

Torbjørn Ergon & Julie Bommerlund

Deer densities were estimated using a hierarchical state space model fitted by the use of Bayesian MCMC sampling in NIMBLE (v0.12.1; de Valpine et al., 2017; 2022). Specifically, we combined a double-observer observation model with an overdispersed Poisson process model describing the variation in true deer densities among sampling sites (focal images). We will here first derive the observation model and the process model, using a hierarchical formulation, and then explain how we made use of known density at the deer farm to inform priors for detection probabilities. The NIMBLE model code is given in Appendix D4.

To estimate abundance and population density, one must account for the fact that not all individuals that are present will be observed (i.e., imperfect detection). We used a double observer protocol to estimate detection probabilities (section 2.5.2 in the main text). By estimating the detection probabilities of two independent observers, it is also possible to estimate the number of individuals that are not observed, and hence population density (Nichols et al., 2000).

At each site (focal image) we have records of how many individuals that were seen by only observer 1 (y_{10}), how many individuals were seen by only observer 2 (y_{01}), and how many individuals were seen by both observers (y_{11}). For a given site i , we denote the observed data by a vector $\mathbf{y}_i = [y_{01}, y_{10}, y_{11}]_i$, and the number of individuals seen by at least one observer is the sum of the elements in this vector, $Y_i = y_{01,i} + y_{10,i} + y_{11,i}$. The observation model defined in the first section below describes the probability (likelihood) of getting these observed data conditional on the number of individuals (N_i) present at each site; i.e. $L(\mathbf{y}_i|N_i)$. The number of individuals at each site, N_i , is unknown, and the stochastic model for this is described in the next section.

Observation model

Given that the two observers detect individuals independently with probabilities p_1 and p_2 respectively, the probability that an individual is detected by only observer 1 is $P_{10} = p_1(1 - p_2)$, the probability of only being detected by observer 2 is $P_{01} = (1 - p_1)p_2$, and the probability of being detected by both observers is $P_{11} = p_1p_2$. The probability of being detected by at least one observer is the same as one minus the probability of not being detected by any of the observers, $p^* = 1 - (1 - p_1)(1 - p_2)$. Note that this is equivalent to $p^* = P_{10} + P_{01} + P_{11}$.

The key to derive a model for the observed data ($L(\mathbf{y}_s|N_s)$), is to first write the probability of getting the observed data as the probability of the observed data *conditional* on the number of individuals seen by at least one observer (Y_i), and then multiply this with the probability of observing Y_i . I.e., $L(\mathbf{y}_i|N_i) = L(\mathbf{y}_i|Y_i)L(Y_i|N_i)$. The first of these components is a multinomial likelihood, and the second component is a binomial likelihood. Hierarchically, we write this as

$$\mathbf{y}_i \sim \text{Multinomial}(\boldsymbol{\pi}, Y_i)$$

$$Y_i \sim \text{Binomial}(p^*, N_i)$$

where $\boldsymbol{\pi} = [P_{10}, P_{01}, P_{11}]/p^*$ (i.e., the multinomial probability vector $\boldsymbol{\pi}$ contains the probabilities of the three detection categories conditional on detection). Note that all observed individuals must belong to one, and only one, of the three detection categories, and hence the elements of $\boldsymbol{\pi}$ sum to one.

The observation model formulated here has only two top level parameters: the detection probabilities of the two observers, p_1 and p_2 . These could have been made site specific, and then been modelled as a function of covariates on e.g. a logit scale.

Process model

The number of individuals present at a site was modelled as an overdispersed Poisson process with a log-normal expectation. Denoting the expected number of individuals at site i as $\lambda_i a_i$ where λ_i is the expectation per unit area (we used hectares) and a_i is the area of the site, we can write the model hierarchically as,

$$N_i \sim \text{Poisson}(\lambda_i a_i)$$

$$\log(\lambda_i) = \mu_i + \varepsilon_i$$

$$\mu_i = \mathbf{x}_i \boldsymbol{\beta}$$

$$\varepsilon_i \sim N(0, \sigma_\varepsilon)$$

where μ_i is the expectation of $\log(\lambda_i)$ and ε_i represents the random variation in density among sites; ε_i is drawn from a normal distribution with zero mean and standard deviation σ_ε . $\mathbf{x}_i \boldsymbol{\beta}$ is the linear model for μ_i (without the constraint $\mu_i = \mathbf{x}_i \boldsymbol{\beta}$, the model would be unidentifiable as μ_i and ε_i would be fully confounded).

Sampling area specific predictions can be obtained by including a set of binary indicator variables in \mathbf{x}_i . However, it is important to realize that if \mathbf{x}_i includes sampling area covariates that only vary among sampling areas, and not just site covariates that vary within sampling areas, a random effect of sampling area would need to be included in order to avoid pseudoreplication (sites within sampling areas is not a random sample of sites with the same sampling area covariate value). Failure to do this would lead to overconfident estimates of the effects of the sampling area covariates (i.e., too narrow posterior distributions). Hence, to accommodate modelling of sampling area covariates, one would have to expand the model to

$$N_i \sim \text{Poisson}(\lambda_i a_i)$$

$$\log(\lambda_i) = \mu_i + \delta_{s(i)} + \varepsilon_i$$

$$\mu_i = \mathbf{x}_i \boldsymbol{\beta}$$

$$\delta_{s(i)} \sim N(0, \sigma_\delta)$$

$$\varepsilon_i \sim N(0, \sigma_\varepsilon)$$

where $\delta_{s(i)}$ is the random effect of the sampling area that site i belongs to, and σ_δ is the standard deviation of this effect. Note that the former model is a special case of the latter with σ_δ fixed to zero.

With this model, the predicted median density among sites with the same characteristics, defined by the predictor variables \mathbf{x}_i , becomes e^{μ_i} , and the predicted mean becomes $e^{\mu_i + \sigma^2/2}$ (the mean is higher than the median because the log-normal distribution is right-skewed). Here, $\sigma = \sigma_\delta^2 + \sigma_\varepsilon^2$ unless one is conditioning the predictions on a specific sampling area, in which case the predicted mean becomes $e^{\mu_i + \delta_{s(i)} + \sigma_\varepsilon^2/2}$. To predict the total number of individuals in a larger area, it is the predicted mean density (not median density) among sites that should be multiplied by the size of the larger area, and with the model formulation used here, this is a derived parameter.

Top level parameters in the complete model are thus p_1 , p_2 , σ_δ , σ_ε , and $\boldsymbol{\beta}$.

Making use of known density in deer enclosure to inform priors on detectability

The deer density in the enclosure at the deer farm was known, and this may be used to inform the priors for detection probability (Kéry and Schaub, 2011, p. 31). The enclosure surrounded a natural habitat with a similar forest type as at the sampling areas. It is therefore reasonable

to assume that detection probabilities inside and outside of the enclosures are similar. It is, however, not reasonable to assume that the variation in deer densities among sites (focal images) are similar because the enclosure had much higher density, much more females than males, many young individuals, and there were feeding stations where the deer tended to aggregate. Hence, to estimate posterior distributions for detection probabilities, we kept the same model structure as above but made μ a function of known mean density (d) and the unknown variance in density (σ^2). As density is modelled as a log-normal distribution, mean density is $d = e^{\mu + \sigma_\varepsilon^2/2}$, and hence we get $\mu = \log(d) - \sigma_\varepsilon^2/2$ (we did not model μ as a function of covariates since the habitat within the enclosure is very homogenous [similar slope and aspect throughout the enclosure, and distance from field is meaningless]). Hence, we used the following hierarchical model:

$$\mathbf{y}_i \sim \text{Multinomial}(\boldsymbol{\pi}, Y_i)$$

$$Y_i \sim \text{Binomial}(p^*, N_i)$$

$$N_i \sim \text{Poisson}(\lambda_i a_i)$$

$$\log(\lambda_i) = \mu + \varepsilon_i$$

$$\mu = \log(d) - \sigma_\varepsilon^2/2$$

$$\varepsilon_i \sim N(0, \sigma_\varepsilon)$$

As initial analysis showed that there was no significant difference in detection probability for the two observers, we simplified the observation model to have the same detection probability for the two observers, $p_1 = p_2 = p$. The model was then fitted with the following uninformative priors:

$$p \sim \text{Uniform}(0,1)$$

$$\sigma_\varepsilon \sim \text{Uniform}(0,5)$$

To inform priors when fitting the full model to the data from the sampling areas, we first logit-transformed the posterior samples of p (here denoting the vector of posterior samples as \mathbf{p}),

$$\boldsymbol{\eta} = \log\left(\frac{\mathbf{p}}{1 - \mathbf{p}}\right).$$

For the full model applied to data from the sampling areas, we then specified the priors for detection probability as

$$\eta_1 \sim N(\text{mean}(\boldsymbol{\eta}), 1.2 \cdot \text{sd}(\boldsymbol{\eta}))$$

$$\eta_2 \sim N(\text{mean}(\boldsymbol{\eta}), 1.2 \cdot \text{sd}(\boldsymbol{\eta}))$$

$$p_1 = \frac{e^{\eta_1}}{1 + e^{\eta_1}}$$

$$p_2 = \frac{e^{\eta_2}}{1 + e^{\eta_2}}$$

Here, the standard deviations were conservatory increased by 20% to account for the fact that detection probabilities inside and outside of the enclosure could be different.

Appendix F: Model results

Prior

The summary of the results from the model used to inform priors for detection probability was as follows:

```
Thinning interval = 1
Number of chains = 3
Sample size per chain = 2e+05

1. Empirical mean and standard deviation for each variable,
   plus standard error of the mean:
```

	Mean	SD	Naive SE	Time-series SE
median_lambda[1]	2.4129	1.70701	2.204e-03	0.0268997
median_lambda[2]	14.2046	4.08846	5.278e-03	0.0318845
mu[1]	0.5980	0.82879	1.070e-03	0.0163035
mu[2]	2.5983	0.36640	4.730e-04	0.0032839
p[1]	0.7795	0.04189	5.407e-05	0.0001102
p[2]	0.7843	0.05334	6.886e-05	0.0001404
sigma[1]	2.2316	0.35979	4.645e-04	0.0066836
sigma[2]	1.0039	0.31815	4.107e-04	0.0025879

2. Quantiles for each variable:

	2.5%	25%	50%	75%	97.5%
median_lambda[1]	0.2755	1.1242	2.0202	3.3062	6.6753
median_lambda[2]	5.1605	11.5348	14.7348	17.3409	20.6154
mu[1]	-1.2892	0.1171	0.7032	1.1958	1.8984
mu[2]	1.6410	2.4454	2.6902	2.8531	3.0260
p[1]	0.6911	0.7526	0.7820	0.8090	0.8544
p[2]	0.6696	0.7504	0.7881	0.8222	0.8775
sigma[1]	1.5839	1.9784	2.2134	2.4640	2.9806
sigma[2]	0.5034	0.7742	0.9618	1.1894	1.7388

Model 1: Predictor variable 'field distance'

The summary of the results from the model using field distance as a predictor variable was as follows:

```
Iterations = 1:2e+05
Thinning interval = 1
Number of chains = 3
Sample size per chain = 2e+05

1. Empirical mean and standard deviation for each variable,
   plus standard error of the mean:
```

	Mean	SD	Naive SE	Time-series SE
beta	0.51591	0.23498	3.034e-04	1.028e-03
mean_lambda[1]	1.20022	0.80528	1.040e-03	3.925e-03
mean_lambda[2]	0.63578	0.33739	4.356e-04	1.582e-03
mean_lambda[3]	0.07392	0.10702	1.382e-04	2.947e-04
mean_lambda[4]	0.05566	0.08144	1.051e-04	2.099e-04
mean_lambda[5]	0.17105	0.12337	1.593e-04	5.326e-04
mean_lambda[6]	0.35731	0.15476	1.998e-04	7.062e-04

mean_lambda[7]	0.04481	0.06901	8.910e-05	1.909e-04
mean_lambda[8]	0.13478	0.10872	1.404e-04	4.150e-04
median_lambda[1]	0.25068	0.13895	1.794e-04	6.897e-04
median_lambda[2]	0.13525	0.06473	8.357e-05	3.613e-04
median_lambda[3]	0.01517	0.01977	2.553e-05	4.081e-05
median_lambda[4]	0.01165	0.01598	2.062e-05	3.499e-05
median_lambda[5]	0.03563	0.02263	2.922e-05	7.682e-05
median_lambda[6]	0.07699	0.03274	4.227e-05	2.229e-04
median_lambda[7]	0.00923	0.01302	1.680e-05	2.894e-05
median_lambda[8]	0.02822	0.02110	2.723e-05	6.806e-05
mu0[1]	-1.51340	0.50093	6.467e-04	2.559e-03
mu0[2]	-2.09909	0.43484	5.614e-04	2.481e-03
mu0[3]	-4.93149	1.23724	1.597e-03	2.618e-03
mu0[4]	-5.14367	1.15183	1.487e-03	2.562e-03
mu0[5]	-3.48109	0.51488	6.647e-04	1.796e-03
mu0[6]	-2.64432	0.39455	5.094e-04	2.709e-03
mu0[7]	-5.32102	1.07525	1.388e-03	2.492e-03
mu0[8]	-3.75460	0.57398	7.410e-04	1.908e-03
p1	0.72797	0.04860	6.275e-05	1.031e-04
p2	0.84024	0.03811	4.920e-05	8.505e-05
sigma	1.73807	0.22526	2.908e-04	2.106e-03

2. Quantiles for each variable:

	2.5%	25%	50%	75%	97.5%
beta	0.052355	0.358755	0.516591	0.67401	0.97684
mean_lambda[1]	0.384683	0.694571	0.992916	1.45396	3.24082
mean_lambda[2]	0.249454	0.413316	0.556257	0.76327	1.49512
mean_lambda[3]	0.004103	0.011850	0.030869	0.08965	0.37956
mean_lambda[4]	0.003968	0.010537	0.024412	0.06448	0.29175
mean_lambda[5]	0.052341	0.094201	0.137443	0.20775	0.48664
mean_lambda[6]	0.160275	0.251935	0.324955	0.42495	0.74300
mean_lambda[7]	0.003846	0.009382	0.020074	0.04960	0.24025
mean_lambda[8]	0.037260	0.068861	0.103292	0.16296	0.41738
median_lambda[1]	0.092550	0.150533	0.216498	0.31198	0.60685
median_lambda[2]	0.059720	0.087435	0.119661	0.16598	0.29976
median_lambda[3]	0.001097	0.002498	0.006536	0.01905	0.07681
median_lambda[4]	0.001080	0.002204	0.005118	0.01366	0.06276
median_lambda[5]	0.014713	0.020310	0.028710	0.04312	0.09639
median_lambda[6]	0.036358	0.052486	0.069804	0.09361	0.15908
median_lambda[7]	0.001070	0.001982	0.004207	0.01042	0.04969
median_lambda[8]	0.010604	0.014703	0.021368	0.03394	0.08562
mu0[1]	-2.380011	-1.893573	-1.530174	-1.16481	-0.49947
mu0[2]	-2.818081	-2.436865	-2.123090	-1.79587	-1.20479
mu0[3]	-6.815310	-5.992163	-5.030442	-3.96068	-2.56642
mu0[4]	-6.830654	-6.117424	-5.274969	-4.29310	-2.76849
mu0[5]	-4.219019	-3.896642	-3.550499	-3.14385	-2.33934
mu0[6]	-3.314333	-2.947218	-2.662058	-2.36862	-1.83836
mu0[7]	-6.839692	-6.223746	-5.470924	-4.56410	-3.00202
mu0[8]	-4.546552	-4.219672	-3.845842	-3.38329	-2.45789
p1	0.626717	0.696368	0.730105	0.76203	0.81686
p2	0.756873	0.816468	0.843403	0.86740	0.90571
sigma	1.307153	1.585008	1.733830	1.88752	2.19059

Table F1: Matrix showing the correlation between the posterior distribution of the top-level parameters from the model using field distance as a predictor variable.

	β	$\mu_{0,1}$	$\mu_{0,2}$	$\mu_{0,3}$	$\mu_{0,4}$	$\mu_{0,5}$	$\mu_{0,6}$	$\mu_{0,7}$	$\mu_{0,8}$	p_1	p_2	σ
β	1.000	-0.059	-0.068	0.038	0.052	-0.204	-0.178	-0.05	-0.165	-0.008	-0.009	-0.029
$\mu_{0,1}$	-0.059	1.000	0.120	0.015	0.025	0.081	0.163	0.022	0.072	-0.007	-0.009	-0.278
$\mu_{0,2}$	-0.068	0.120	1.000	0.021	0.029	0.107	0.237	0.034	0.100	-0.010	-0.013	-0.405
$\mu_{0,3}$	0.038	0.015	0.021	1.000	0.008	0.009	0.025	0.003	0.006	-0.002	0.002	-0.061
$\mu_{0,4}$	0.052	0.025	0.029	0.008	1.000	0.011	0.037	0.003	0.013	-0.001	0.001	-0.09
$\mu_{0,5}$	-0.204	0.081	0.107	0.009	0.011	1.000	0.160	0.026	0.086	-0.005	-0.006	-0.223
$\mu_{0,6}$	-0.178	0.163	0.237	0.025	0.037	0.160	1.000	0.048	0.148	-0.013	-0.015	-0.520
$\mu_{0,7}$	-0.050	0.022	0.034	0.003	0.003	0.026	0.048	1.000	0.025	-0.001	-0.001	-0.070
$\mu_{0,8}$	-0.165	0.072	0.100	0.006	0.013	0.086	0.148	0.025	1.000	-0.005	-0.006	-0.209
p_1	-0.008	-0.007	-0.010	-0.002	-0.001	-0.005	-0.013	-0.001	-0.005	1.000	0.115	-0.012
p_2	-0.009	-0.009	-0.013	0.002	0.001	-0.006	-0.015	-0.001	-0.006	0.115	1.000	-0.015
σ	-0.029	-0.278	-0.405	-0.061	-0.090	-0.223	-0.520	-0.070	-0.209	-0.012	-0.015	1.000

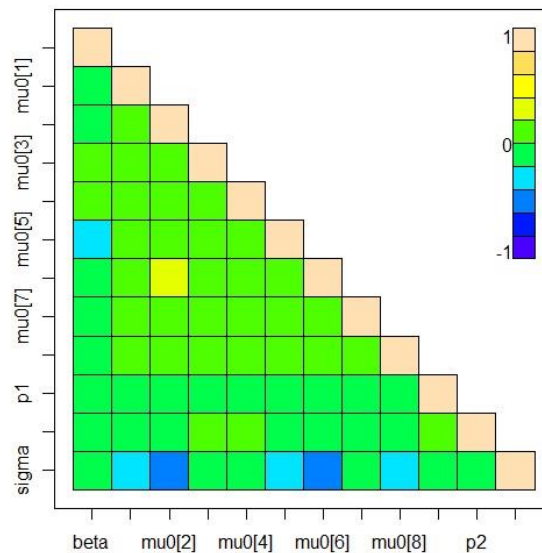


Figure F1: Correlation between the posterior distribution of the top-level parameters from the model using field distance as a predictor variable.

Model 2: Predictor variable 'forest distance'

The summary of the results from the model using forest (i.e., end of forest) distance as a predictor variable was as follows:

```
Iterations = 1:2e+05
Thinning interval = 1
Number of chains = 3
Sample size per chain = 2e+05
```

1. Empirical mean and standard deviation for each variable, plus standard error of the mean:

	Mean	SD	Naive SE	Time-series SE
beta	0.373564	0.21051	2.718e-04	9.078e-04
mean_lambda[1]	1.300777	0.88498	1.142e-03	4.442e-03

mean_lambda[2]	0.692142	0.37280	4.813e-04	1.782e-03
mean_lambda[3]	0.072416	0.10673	1.378e-04	2.929e-04
mean_lambda[4]	0.052913	0.07850	1.013e-04	2.040e-04
mean_lambda[5]	0.210495	0.15304	1.976e-04	6.058e-04
mean_lambda[6]	0.390491	0.17173	2.217e-04	7.679e-04
mean_lambda[7]	0.049305	0.07660	9.889e-05	2.042e-04
mean_lambda[8]	0.149094	0.12280	1.585e-04	4.736e-04
median_lambda[1]	0.251419	0.14148	1.826e-04	7.026e-04
median_lambda[2]	0.136321	0.06589	8.506e-05	3.654e-04
median_lambda[3]	0.013807	0.01845	2.381e-05	3.951e-05
median_lambda[4]	0.010244	0.01423	1.837e-05	3.205e-05
median_lambda[5]	0.040974	0.02720	3.511e-05	9.406e-05
median_lambda[6]	0.078039	0.03342	4.315e-05	2.323e-04
median_lambda[7]	0.009413	0.01337	1.726e-05	2.988e-05
median_lambda[8]	0.028904	0.02194	2.833e-05	7.077e-05
mu0[1]	-1.513154	0.50526	6.523e-04	2.603e-03
mu0[2]	-2.093074	0.43899	5.667e-04	2.489e-03
mu0[3]	-5.011570	1.20806	1.560e-03	2.634e-03
mu0[4]	-5.239928	1.10888	1.432e-03	2.506e-03
mu0[5]	-3.361427	0.55485	7.163e-04	1.987e-03
mu0[6]	-2.632311	0.39862	5.146e-04	2.761e-03
mu0[7]	-5.310457	1.08185	1.397e-03	2.494e-03
mu0[8]	-3.736339	0.58328	7.530e-04	1.957e-03
p1	0.727942	0.04868	6.284e-05	1.032e-04
p2	0.840351	0.03803	4.910e-05	8.437e-05
sigma	1.780772	0.22670	2.927e-04	2.124e-03

2. Quantiles for each variable:

	2.5%	25%	50%	75%	97.5%
beta	-0.042900	0.233038	0.375109	0.51534	0.78342
mean_lambda[1]	0.408227	0.745229	1.070563	1.57415	3.57155
mean_lambda[2]	0.267076	0.445977	0.603065	0.83323	1.64114
mean_lambda[3]	0.004285	0.012144	0.030361	0.08562	0.38046
mean_lambda[4]	0.004191	0.010671	0.023762	0.06046	0.27716
mean_lambda[5]	0.059186	0.112778	0.168329	0.25878	0.60590
mean_lambda[6]	0.174587	0.274423	0.354541	0.46425	0.81691
mean_lambda[7]	0.004117	0.010203	0.021852	0.05424	0.26638
mean_lambda[8]	0.039976	0.075082	0.113432	0.18038	0.46891
median_lambda[1]	0.092550	0.149994	0.215743	0.31323	0.61480
median_lambda[2]	0.059730	0.087614	0.120363	0.16733	0.30492
median_lambda[3]	0.001089	0.002381	0.005926	0.01676	0.07259
median_lambda[4]	0.001075	0.002082	0.004600	0.01181	0.05496
median_lambda[5]	0.014922	0.022251	0.032754	0.05064	0.11403
median_lambda[6]	0.036465	0.052936	0.070845	0.09514	0.16121
median_lambda[7]	0.001072	0.001998	0.004228	0.01056	0.05132
median_lambda[8]	0.010624	0.014848	0.021784	0.03481	0.08862
mu0[1]	-2.380006	-1.897161	-1.533667	-1.16083	-0.48647
mu0[2]	-2.817920	-2.434813	-2.117245	-1.78780	-1.18772
mu0[3]	-6.822788	-6.040208	-5.128349	-4.08848	-2.62288
mu0[4]	-6.835003	-6.174631	-5.381617	-4.43876	-2.90107
mu0[5]	-4.204902	-3.805347	-3.418744	-2.98293	-2.17131
mu0[6]	-3.311393	-2.938667	-2.647268	-2.35236	-1.82503
mu0[7]	-6.838350	-6.215664	-5.466087	-4.55090	-2.96963
mu0[8]	-4.544643	-4.209864	-3.826591	-3.35796	-2.42337
p1	0.626507	0.696097	0.730260	0.76214	0.81661
p2	0.757399	0.816527	0.843434	0.86752	0.90559
sigma	1.346578	1.626547	1.776614	1.93100	2.23727

Model 3: Predictor variable 'mean elevation'

The summary of the results from the model using mean elevation as a predictor variable was as follows:

```

Iterations = 1:2e+05
Thinning interval = 1
Number of chains = 3
Sample size per chain = 2e+05

```

1. Empirical mean and standard deviation for each variable, plus standard error of the mean:

	Mean	SD	Naive SE	Time-series SE
beta	0.344784	0.37198	4.802e-04	2.724e-03
mean_lambda[1]	1.059795	0.91842	1.186e-03	6.196e-03
mean_lambda[2]	0.565437	0.40832	5.271e-04	2.926e-03
mean_lambda[3]	0.070114	0.10174	1.313e-04	2.841e-04
mean_lambda[4]	0.053278	0.07800	1.007e-04	2.032e-04
mean_lambda[5]	0.244872	0.18125	2.340e-04	6.329e-04
mean_lambda[6]	0.480696	0.20710	2.674e-04	8.939e-04
mean_lambda[7]	0.042742	0.07170	9.257e-05	2.491e-04
mean_lambda[8]	0.139655	0.14438	1.864e-04	7.559e-04
median_lambda[1]	0.213022	0.13363	1.725e-04	6.927e-04
median_lambda[2]	0.115923	0.06347	8.194e-05	3.414e-04
median_lambda[3]	0.014815	0.01950	2.518e-05	4.410e-05
median_lambda[4]	0.011536	0.01606	2.074e-05	4.246e-05
median_lambda[5]	0.053794	0.03940	5.086e-05	1.751e-04
median_lambda[6]	0.110024	0.05739	7.410e-05	5.077e-04
median_lambda[7]	0.008628	0.01244	1.606e-05	2.895e-05
median_lambda[8]	0.028455	0.02446	3.158e-05	8.827e-05
mu0[1]	-1.686888	0.50318	6.496e-04	2.579e-03
mu0[2]	-2.261176	0.43462	5.611e-04	2.298e-03
mu0[3]	-4.955491	1.23167	1.590e-03	2.808e-03
mu0[4]	-5.161163	1.15254	1.488e-03	3.086e-03
mu0[5]	-3.131510	0.63067	8.142e-04	2.928e-03
mu0[6]	-2.330514	0.49585	6.401e-04	4.543e-03
mu0[7]	-5.379099	1.05452	1.361e-03	2.513e-03
mu0[8]	-3.769964	0.59516	7.683e-04	2.158e-03
p1	0.727800	0.04876	6.295e-05	1.038e-04
p2	0.840230	0.03818	4.928e-05	8.512e-05
sigma	1.725192	0.24182	3.122e-04	2.545e-03

2. Quantiles for each variable:

	2.5%	25%	50%	75%	97.5%
beta	-0.425973	0.101896	0.360533	0.60369	1.02758
mean_lambda[1]	0.286356	0.530387	0.798919	1.26515	3.38897
mean_lambda[2]	0.182598	0.317133	0.453064	0.67642	1.61762
mean_lambda[3]	0.003930	0.011519	0.029641	0.08466	0.35769
mean_lambda[4]	0.003836	0.010257	0.023601	0.06173	0.27846
mean_lambda[5]	0.061917	0.126872	0.195667	0.30555	0.71357
mean_lambda[6]	0.206951	0.338861	0.441101	0.57498	0.98897
mean_lambda[7]	0.003595	0.008724	0.018376	0.04493	0.23900
mean_lambda[8]	0.033117	0.062928	0.097510	0.16273	0.50178
median_lambda[1]	0.088675	0.124262	0.173448	0.25595	0.56870
median_lambda[2]	0.057795	0.073671	0.096793	0.13649	0.28529
median_lambda[3]	0.001093	0.002451	0.006314	0.01845	0.07604
median_lambda[4]	0.001079	0.002170	0.004973	0.01335	0.06337
median_lambda[5]	0.015393	0.026688	0.042202	0.06796	0.15877
median_lambda[6]	0.038698	0.067652	0.097312	0.13847	0.25378

median_lambda[7]	0.001066	0.001912	0.003926	0.00952	0.04728
median_lambda[8]	0.010572	0.014300	0.020629	0.03311	0.09325
mu0[1]	-2.422774	-2.085367	-1.751879	-1.36276	-0.56440
mu0[2]	-2.850861	-2.608152	-2.335178	-1.99148	-1.25427
mu0[3]	-6.818968	-6.011149	-5.065009	-3.99291	-2.57653
mu0[4]	-6.831521	-6.133209	-5.303662	-4.31645	-2.75880
mu0[5]	-4.173830	-3.623539	-3.165277	-2.68877	-1.84031
mu0[6]	-3.251964	-2.693378	-2.329834	-1.97708	-1.37127
mu0[7]	-6.844185	-6.259580	-5.540183	-4.65437	-3.05164
mu0[8]	-4.549536	-4.247481	-3.881034	-3.40795	-2.37250
p1	0.626271	0.695894	0.730041	0.76197	0.81675
p2	0.757159	0.816281	0.843333	0.86757	0.90567
sigma	1.271954	1.557863	1.718694	1.88500	2.21643